Master's thesis

NTNU
Norwegian University of Science and Technology
Faculty of Engineering
Department of Marine Technology

Martinus Kristiansen Aarmo

A station-keeping analysis of a damaged floating offshore wind turbine

Master's thesis in Marine Technology
Supervisor: Marilena Greco
Co-supervisor: Mohd Atif Siddiqui
June 2023

NTNU
Norwegian University of
Science and Technology

Martinus Kristiansen Aarmo

A station-keeping analysis of a damaged floating offshore wind turbine

Master's thesis in Marine Technology
Supervisor: Marilena Greco
Co-supervisor: Mohd Atif Siddiqui
June 2023

Norwegian University of Science and Technology
Faculty of Engineering
Department of Marine Technology

NTNU
Norwegian University of
Science and Technology

Preface

This master's thesis presents the research and analysis conducted at the Norwegian University of Science and Technology (NTNU) under the Department of Marine Technology. The thesis was conducted during the Spring of 2023, and is the final milestone of the specialization within the field of Hydrodynamics.

The primary objective of this thesis is to present a comprehensive numerical study focusing on the analysis of damaged floating offshore wind turbines (FOWTs). The significance of this research lies in the potential to advance our understanding of the behavior and performance of these critical scenarios, ultimately contributing to the development of more sturdy and efficient offshore wind energy systems.

The groundwork for this master's thesis was laid during the preceding fall of 2022 when a project thesis was conducted. The project thesis served as a preliminary investigation, providing a foundation upon which this master's thesis was built. The selection of the thesis topic was driven by a genuine interest in the domains of renewable energy, dynamics, and hydrodynamics. Some parts of the master project were re-used in the master thesis due to relevance to the tasks completed.

During the project thesis, extensive literature reviews were undertaken, exploring the causes and occurrences of damage on FOWTs. Furthermore, attention was given to the study of modeling and simulation techniques, numerical tools, and the identification of relevant offshore wind turbine sites. Notably, certain sections of the project thesis have been incorporated into this master's thesis as supplementary material, ensuring their seamless integration and emphasizing their relevance within the overall research framework. Throughout this report, specific sections will explicitly highlight the inclusion of material from the project thesis, thereby underscoring their contribution to the broader scope of this research.

Trondheim, May 31st, 2022

Martinus K. Aarmo

Acknowledgments

First and foremost, I would like to express my gratitude to my supervisor, Professor Marilena Greco, whose guidance and expertise have been necessary in shaping the path of this research over the past year. Her invaluable support has extended far beyond academic matters, as she has also been a source of emotional encouragement during challenging periods involving intense workload. I am truly grateful for her interest in my work, which has motivated me to push the boundaries of my capabilities and achieve greater outcomes.

I extend my heartfelt appreciation to Mohd Atif Siddiqui from Kongsberg Maritime for his exceptional guidance and support throughout the course of this past year. Mr. Siddiqui's keen interest in my studies has been very helpful in propelling this thesis forward. His extensive relevant knowledge during critical junctures has been invaluable. I am very grateful for his commitment to this thesis and his ongoing motivation to ensure its success.

Furthermore, I would like to extend my gratitude to all the professors at the institute who have demonstrated a genuine interest in my work. Their valuable insights, advice, and guidance have significantly contributed to the outcome of this thesis. I deeply appreciate their willingness to share their expertise and provide me with the necessary guidance to navigate this research.

Lastly, I wish to express my deepest appreciation to my friends and family for their unwavering support throughout my academic journey. Their constant encouragement, understanding, and belief in my abilities have been a source of strength and inspiration. Without their unwavering support, I would not have reached this pivotal point in my academic pursuit. I will forever cherish their contributions and the profound impact they have had on my personal and academic growth.

Nomenclature

Abbreviations

BEM	Blade element momentum
COB	Center of buoyancy
COG	Center of gravity
DLF	Dynamic load factor
DOF	Degree of freedom
FEM	Finite element method
FOWT	Floating offshore wind turbine
FWT	Floating wind turbine
JONSWAP	Joint North Sea Wave Project
NORA10	Norwegian Reanalysis 10km
NORA3	Norwegian Reanalysis 3km
PDF	Probability density function
PM	Pierson-Moskowitz
QTF	Quadratic transfer function
RAO	Response amplitude operator
SIMO	Simulation of marine operations
TDP	Touch down point
TLP	Tension legged platform
WADAM	Wave analysis by diffraction and Morison theory

Symbols

ω_p	Peak frequency
ρ	Density
σ	Spectral width
α	Angle of Attack
α	Phase angle
α	Scaling factor
$\bar{F}$	Mean drift force

β	Frequency ratio
β	Wave propagation angle
$\dot{m}$	Mass flow rate
ϵ	Phase angle
$\eta, \dot{\eta}, \ddot{\eta}$	Body motion, velocity, acceleration
γ	Peak enhancement factor
λ	Tip speed ratio
λ	Wave length
λ_r	Local speed ratio
Ω	Angular velocity of rotor
Ω	Fluid domain
ω	Frequency
ω_0	Undamped natural frequency
ϕ	Velocity potential
ϕ_0	Incident wave potential
ϕ_D	Diffraction potential
ϕ_R	Radiation potential
ρ	Fluid density
$_P$	Spectral peak period
τ	Time lag integration factor
$\tilde{x}$	Particular solution
ζ	Damping ratio
ζ_{An}	Wave amplitude
a'	Angular induction factor
A	Added mass matrix
a	Acceleration
a	Axial induction factor
a	Fluid particle acceleration
A_0, A_1	Inlet-, outlet area

B	Damping matrix
C	Restoring matrix
C_D	Drag coefficient
C_G	Center of gravity
C_l	Lift coefficient
C_M	Mass coefficient
C_P	Turbine power coefficient
D	Diameter
d	Water depth
E	Energy
F	Force
F	Wave force transfer function
F^{ext}	Wave excitation load
F^{RAD}	Radiation load
F^{SV}	Slow-drift excitation
F_d	Damping force
F_i	Inertia force
F_i^{SV}	Slow drift excitation loads
F_S	Restoring force
g	Gravitational constant
h	Verticle span
h	Water depth
H_S	Significant wave height
K	Stiffness
k	Wave number
L	Lift force
l_s	Length of suspended line
m	Mass
m_n	Spectral moment

N	Number of wave components
P	Load
P	Power
p	Pressure
P_0	Maximum load
p_a	Atmospheric pressure
p_d	Dynamic pressure
Q	Torque
R	Radius of gyration
r	Specific radius of blades
T	Period
T	Thrust
T_H	Horizontal tension
T_{jk}	Second-order quadratic transfer function
T_{jk}^{ic}, T_{is}^{jk}	Second order quadratic transfer functions
$u, \dot{u}, \ddot{u}$	Displacement, velocity, acceleration
u	Fluid particle velocity
u	Response
U_C	Current velocity
u_p	Particular solution
U_w	Wind velocity
u_{st}	Static displacement
V	Fluid velocity
v_0	Inlet velocity
V_B	Body velocity
V_n	Normal component of fluid velocity
X	Response transfer function
z	Distance to water surface

NTNU Trondheim
Norwegian University of Science and Technology
Faculty of Engineering Science and Technology
Department of MarineTechnology

MASTER THESIS IN MARINE TECHNOLOGY

Spring 2023

FOR

Martinus Kristiansen Aarmo

A station-keeping analysis of a damaged floating offshore wind turbine

(En stasjonsholdingsanalyse av en skadet flytende vindturbin til havs)

Floating Offshore Wind Turbines (FOWTs) represent a young, growing industry with majority of the work focused on development, installation, and improving efficiency. Innovation in floating structures, turbine sizes and mooring designs has also been a major area of interest. As the number of floating units and size increase, chances of accidental events and safety become an important issue.

The present study aims to investigate the station-keeping of a FOWT with a semisubmersible floater, assuming operational and extreme sea conditions and considering both intact and damaged conditions. In the project thesis, the candidate examined the state-of-the art, including classification rules; he selected the simulation tool (SIMA), the FOWT (INO-WINDMOOR 12MW) and identified the field site (Hywind Tampen) for the studies. The intact model was available, and a preliminary frequency-domain analysis was performed using HydroD, checking numerical convergence and assessing the results against reference data. Then two compartment models were included to examine the effects of damage on the floater, and the effects of free-surface and sloshing were investigated using HydroD.

Objective
The master thesis has the overall target to provide insights on the influence of damage presence, location, and features, on station-keeping of a FOWT with semi-submersible floater.

The work should be carried out in steps as follows; some include part of the work done in the project thesis so to make the MSc thesis a stand-alone document:

1. Provide the background motivation and state-of-the-art relevant for this topic in terms of available studies, existing rules/guidelines for damage scenarios, available prediction tools for studying the behaviour at sea of FOWTs with emphasis on the tool chosen for this analysis. Provide the information on the selected site and on the available metocean data. Base this on the material collected in the project work and complement it when needed.
2. Based on step 1, select the damage scenarios to be investigated, for which the FOWT can achieve a stable condition in calm water, and select the environmental conditions for the statistical analysis to assess behaviour at sea with respect to intact conditions.
3. Perform the frequency-domain analysis of the floater in intact and damaged conditions. Check numerical convergence and accuracy through comparison against available intact-floater results. Discuss comparatively the results (e.g., RAOs) for the floater in intact and damaged conditions.
4. Check the natural periods and other relevant parameters for the intact and damaged FOWT models and perform the time-domain analysis of the FOWT in intact and damaged conditions, neglecting the effects of transient mechanisms at the damage

opening. Examine selected operational and extreme wave conditions and assess effects of second-order wave loads and of wind loads (e.g., on floater motions, mooring-line tensions, etc.). For operational environmental conditions and damaged FOWT, assume both a parked turbine and an operating turbine.

5. If time allows, for a selected environmental scenario and one damaged scenario case, compare the instantaneous damage-opening position with the local incident-wave elevation to detect possible water transient phenomena, as error sources in the analysis in step 4.
6. Draw the conclusions from the studies and discuss possible further research steps.

The work may show to be more extensive than anticipated. Some topics may therefore be left out after discussion with the supervisor without any negative influence on the grading.
The candidate should in their report give a personal contribution to the solution of the problem formulated in this text. All assumptions and conclusions must be supported by mathematical models and/or references to physical effects in a logical manner.
The candidate should apply all available sources to find relevant literature and information on the actual problem.
The thesis should be organised in a rational manner to give a clear presentation of the work in terms of exposition of results, assessments, and conclusions. It is important that the text is well written, and that tables and figures are used to support the verbal presentation. The thesis should be complete, but still as short as possible. In particular, the text should be brief and to the point, with a clear language. Telegraphic language should be avoided.
The thesis must contain the following elements: the text defining the scope (i.e. this text), preface (outlining project-work steps and acknowledgements), abstract (providing the summary), table of contents, main body of thesis, conclusions with recommendations for further work, list of symbols and acronyms, references and (optional) appendices. All figures, tables and equations shall be numerated.
The supervisor may require that the candidates, in an early stage of the work, present a written plan for the completion of the work. The plan should include budget for the use of computer and laboratory resources that will be charged to the department. Overruns shall be reported to the supervisor.
From the thesis it should be possible to identify the work carried out by the candidate and what has been found in the available literature. It is important to give references to the original source for theories and experimental results.

Supervisor : Marilena Greco
Co-supervisor : Mohd Atif Siddiqui

Submitted : January 15th 2023
Deadline : June 11th 2023

Marilena Greco
Supervisor

Abstract

The increasing demand for renewable energy has placed wind energy at the forefront of sustainable power generation. In recent years, the wind energy industry has expanded beyond land-based installations to offshore locations, particularly in deep waters exceeding 150 meters. Offshore wind farms offer vast open areas at more affordable prices. However, this industry faces several challenges, particularly regarding the unpredictable environmental conditions, which pose difficulties for the operation and maintenance of large offshore structures.

The objective of this thesis is to investigate the performance of the INO-WINDMOOR 12MW semi-submersible FWT at a water depth of 280 meters. This study focuses on analyzing the chosen semi-submersible floater design and evaluating its behavior under both operational and extreme conditions using state-of-the-art prediction tools.

Numerical models of the semi-submersible were developed using finite element panel and compartment models. The finite element panel model, created in GeniE software, accurately represented the structural components, while the compartment model represents the internal volumes filled with seawater for damage cases. These models, along with a finite element surface model, were utilized in the software HydroD to perform first- and second-order frequency-domain analyses and calculate the hydrodynamic properties of the floater. To account for second-order effects, a free-surface model was incorporated. The hydrodynamic properties obtained from these analyses were then integrated into the SIMA software to create a coupled time-domain model.

Given the complexity and computational cost of the analyses, symmetric models of the floater were employed. Additionally, investigations were conducted to assess the applicability of symmetric models for non-symmetric load cases, aiming to simplify computational requirements while maintaining acceptable results. All hydrodynamic properties were rigorously examined to ensure the accuracy and validity of the obtained results.

The Hywind Tampen area, known for its deep waters, was selected as the appropriate site for the study due to its suitability for offshore wind projects. Environmental conditions from a nearby location were utilized to generate environmental load cases for the coupled time-domain simulations. Three harsh environmental load cases were established to capture more extreme conditions, which were of particular interest.

The numerical models employed in this study underwent rigorous validation procedures, including convergence studies, verification against official analyses, decay tests, and regular wave tests. Furthermore, a dedicated constant wind test was conducted in order to verify the performance of the wind turbine. Subsequently, time-domain simulations were performed using the SIMA software to evaluate the response of the numerical models under various loading configurations and damage cases. These simulations were utilized to perform statistical analysis of the turbine's response, environmental loads, mooring line tensions, and axial accelerations experienced at the turbine nacelle. The obtained results were comprehensively compared and discussed to derive valuable insights into the behavior of damaged FOWTs.

The results indicated a satisfactory agreement between Newman's approximation and analyses utilizing full quadratic transfer functions (QTFs) in the surge direction. However, analyses and simulations conducted without considering static inclinations yielded unsatisfactory results, with significant uncertainties. Notably, the behavior of the damaged configurations proved critical, particularly during emergency shutdown simulations, where the nacelle's axial acceleration exhibited a substantial increase compared to intact configurations.

Sammendrag

En økende etterspørsel etter fornybar energi har plassert vindenergi i frontlinjen for bærekraftig kraftproduksjon. I nyere tider har vindindustrien utvidet seg fra landbaserte installasjoner til offshore-lokasjoner, spesielt i dype farvann som overstiger 150 meter. Offshore vindparker tilbyr store åpne områder til mer overkommelige priser. Imidlertid står denne industrien overfor flere utfordringer, spesielt når det gjelder de uforutsigbare miljøforholdene, som skaper vanskeligheter for driften og vedlikeholdet av store offshore-strukturer.

Målet med denne avhandlingen er å undersøke ytelsen til INO-WINDMOOR 12MW halvt nedsenkbar flytende vindturbin opererende i områder med vanndybde på 280 meter. Studiene fokuserer på å analysere det valgte designet for den halvt nedsenkbare flotøren og evaluering av atferden under både operative og ekstreme forhold ved hjelp av moderne prediksjonsverktøy.

Numeriske modeller av den halvt nedsenkbare enheten ble utviklet ved hjelp av panel modeller og rom modeller. Den endelige panel modellen, opprettet i GeniE-programvaren, representerte nøyaktig de strukturelle komponentene, mens rom modellen representerte de interne volumene fylt med sjøvann for skadesituasjoner. Disse modellene, sammen med en overflate modell, ble benyttet i HydroD-programvaren for å utføre første- og andreordens frekvensdomeneanalyser og å beregne de hydrodynamiske egenskapene til flotøren. For å ta hensyn til andreordenseffekter, ble en fri overflate-modell inkludert. De hydrodynamiske egenskapene som ble utrettet fra disse analysene ble deretter integrert i SIMA-programvaren for å opprette en koplet tidsdomenmodell.

På grunn av kompleksiteten og beregningskostnaden for analysene, ble symmetriske modeller av flotøren benyttet. I tillegg ble det utført undersøkelser for å vurdere anvendeligheten av symmetriske modeller for ikke-symmetriske lasttilfeller, med ett mål om å forenkle beregningskravene samtidig som akseptable resultater opprettholdes. Alle hydrodynamiske resultatene ble nøye undersøkt for å sikre nøyaktighet og gyldighet.

Området Hywind Tampen, kjent for sine dype farvann, ble valgt som ett egnet sted for studiene på grunn av sine passende egenskaper for offshore-vindprosjekter. Miljøforhold fra en nærliggende lokasjon ble brukt til å generere miljøbelastningstilfeller for tidsdomensimuleringene. Tre krevende miljøbelastningstilfeller ble etablert for å fange opp mer ekstreme forhold, som var av spesiell interesse.

De numeriske modellenene benyttet i disse studiene gjennomgikk strenge valideringsprosedyrer, inkludert konvergensstudier, verifikasjon mot offisielle analyser, forfallstester og tester med regulære bølger. Videre ble det gjennomført en konstant vindtest for å verifisere ytelsen til vindturbinen. Deretter ble tidsdomensimuleringer utført ved hjelp av SIMA-programvaren for å evaluere responsen til de numeriske modellene under ulike lastekonfigurasjoner og skadesituasjoner. Disse simuleringene ble brukt til å utføre statistisk analyse av turbinens respons, miljøbelastninger, spenningsnivåer i fortøyningssystemet og akselerasjoner langs aksen som blir opplevd av turbinens komponenter. De oppnådde resultatene ble grundig sammenlignet og

diskutert for å trekke verdifulle innsikter om atferden til skadde flytende offshore-vindturbiner (FOWTs).

Resultatene viste tilfredsstillende samsvar mellom Newman's tilnærming og analyser som brukte QTFs i surge-retningen. Imidlertid ga ikke analysene og simulasjonene gjennomført uten å ta hensyn til statiske helninger tilfredsstillende resultater. Bemerkelsesverdig viste atferden til de skadede konfigurasjonene seg å være kritisk, spesielt under nødstanssimuleringer der akselerasjonen langs aksen til nacellen økte betydelig sammenlignet med intakte konfigurasjoner.

Table of Contents

List of Figures

List of Tables

1 Introduction

1.1 Background

In recent years, the world has been grappling with a series of complex and interconnected global crises, highlighting the interdependencies and challenges of our modern society. From the ongoing COVID-19 pandemic that has reshaped the way we live, work, and interact, to the escalating climate crisis threatening our planet's ecosystems and livelihoods, these crises have had profound impacts on individuals, communities, and nations worldwide. Additionally, economic disparities, political instability, and social unrest have further exacerbated tensions and tested our collective resilience. Addressing these crises requires international cooperation, innovative solutions, and a commitment to sustainable development to navigate the uncertain path ahead and build a more resilient and equitable future for all.

Diverse interpretations of the multitude of crises plaguing our society have fragmented our collective focus, diverting attention away from crucial environmental preservation efforts. An illustrative example of this phenomenon emerged in 2020 when decommissioned coal mines were repurposed for cryptocurrency mining, as documented by Place (2021). However, despite varying opinions, a significant international treaty, known as the Paris Agreement, was adopted during the 2015 United Nations Framework Convention on Climate Change (UNFCCC). This agreement was implemented in response to the urgent need to address the escalating threat of climate change caused by global warming (UNFCCC, 2015). While there has been a decline in the growth of annual CO2 emissions in recent years following the Paris Agreement, actual emissions have not reduced accordingly (IPCC, 2022). Given the gravity of this crisis and its potential far-reaching consequences, decisive action is imperative. With a rapidly growing global population, the demand for increased energy and resources is pressing. However, solving this issue is challenging due to limited space and resources. According to 2022 statistics, coal and natural gas remained the dominant sources of global electricity generation, accounting for approximately 58% of the total annual generation (Statista, 2023). To preserve the climate, a transition to green and sustainable energy sources is paramount for the future. Wind energy has emerged as a promising contender in electricity generation. Despite challenges such as noise, visual impact, transportation, and installation complexities, it has proven capable of producing clean energy. Consequently, the International Energy Agency predicts that wind energy production will become Europe's primary power source by the end of 2027 (WindEurope, 2022). In recent years, offshore wind energy installations have gained traction, mitigating some of the challenges associated with onshore operations. The shift to offshore environments has led to nearly a 20% increase in capacity compared to onshore locations, attributed to higher wind velocities and reduced turbulence (WindEurope, 2022). However, it is important to acknowledge the negative aspects of offshore installations, including harsh and unpredictable environmental conditions, wet and corrosive environments, difficult site access, and higher installation and operational costs (Bachynski-Polic, 2022a).

1.2 The Current Perspective of Offshore Wind Energy

This section presents the current perspective of offshore wind energy. The origins of offshore wind energy can be traced back to Denmark, where two pioneering offshore wind farms, Vindeby and Middelgrunden, were established in 1991 and 2000, respectively. The Vindeby wind farm consisted of 11 turbines, while Middelgrunden featured 20 turbines. Notably, during the nine-year period between the two projects, the individual turbine capacity at Middelgrunden experienced a significant increase of over 4000%, surpassing that of Vindeby (Vikkelsø et al., 2003, Ørsted, 2018). Presently, there is a noticeable global interest in the potential of the wind energy industry. Through a combination of offshore and onshore production, wind energy has the capacity to contribute approximately 15% of Europe's electricity. Several countries have embraced this shift towards sustainable energy and have established goals and targets for the development of new offshore wind farms (GWECS, 2022).

In terms of larger wind farms, Equinor is a leading company in the field. They are credited with one of the first large-scale floating wind farms, known as Hywind Scotland, which has been in operation since 2017 (Equinor, 2022). Since then, many have recognized the potential of renewable energy and have joined this endeavor. Despite this, Equinor is advancing with their latest project, Hywind Tampen, which is projected to have a system capacity of 88MW. Once completed, it will become the largest wind farm in the world (Equinor, 2022). Apart from its size, the shared anchor system in this project is noteworthy due to its complex nature and its alignment with the future goals and plans of offshore wind energy. Considering factors such as deeper waters, harsher environments, and the scale of multiple projects, the requirement for mooring significantly increases. Equinor, for instance, indicates that a 1GW park with 66 floaters would necessitate approximately 200km of mooring lines (H. Haslum, 2018). Given the anticipated expectations of 264GW by 2050 (DNV, 2022a), this would result in over 52000km of mooring lines. To put it into perspective, this amount of mooring would be sufficient to encircle the Earth's circumference. Hence, the concept of shared anchors and mooring represents an exceptional asset in terms of cost-effectiveness for future offshore wind endeavors. Shared mooring lines are not yet applied, this might be due to the potential consequences behind the concept. For now, the rules and standards for offshore wind are less restrictive, as these are new concepts in the development phase. Examples of this are shown in the standard DNV-ST-0119 (DNV, 2021), in which two consequence classes are defined as:

- *Consequence class 1, where failure is unlikely to lead to unacceptable consequences such as loss of life, collision with an adjacent structure, and environmental impacts.*
- *Consequence class 2, where failure may well lead to unacceptable consequences of these types.*

The classification of offshore wind turbines based on consequence classes has a significant impact on the restrictions imposed on these structures. Currently, due to the industry's developmental phase and efforts to expand its reach, most offshore

wind turbines have not yet been classified as consequence class 1. As a result, the stability requirements are relatively lenient, considering the minimal consequences associated with these turbines. However, as the focus shifts towards sustainability and long-term maintenance of offshore wind farms, optimizing damaged conditions and the ability to retrieve impaired turbines will become crucial. Maintaining large-scale offshore wind farms will entail thorough investigation and preparedness for potential damage scenarios. The ability to repair or retrieve damaged FOWTs within a shared mooring configuration may have significant implications for the construction requirements. By employing shared mooring systems, these constructions may be classified as consequence class 1, thereby necessitating heightened safety measures. This underscores the criticality of maintenance for the ongoing success of these large-scale projects. Furthermore, the increased safety and stability requirements are likely to foster research and exploration of new concepts and ideas. Promising advancements can already be observed in the development of new semi-submersible floaters (SENER, 2022, EDP, n.d., Robertson et al., 2014). Semi-submersible designs offer enhanced flexibility in terms of water depth and location compared to traditional offshore wind farms (Bachynski-Polic, 2022a). Consequently, the development of semi-submersible wind-turbine support structures has gained momentum, with approximately 50 designs currently in progress worldwide, as reported by WindEurope (WindEurope, 2020). Among these designs, approximately 60% are semi-submersibles. The mass production of semi-submersibles holds promise for the continued growth of the offshore wind industry, offering a viable option for expansion.

1.3 Preliminary studies

The foundation of this master's thesis was established during the preceding fall semester of 2022. The primary objectives of the project focused on conducting a literature review and familiarizing with the relevant software tools to be employed. The literature review investigated the causes and occurrences of damage to FOWTs, with a specific emphasis on damage resulting from nearby service vessels operating at lower speeds. Considering the increasing significance of semi-submersible floaters in offshore wind applications, the INO-WINDMOOR concept was chosen as the design for this study, along with a suitable offshore site. Furthermore, an extensive review of the state-of-the-art modeling and simulation prediction tools, second-order forces, and sloshing in internal tanks was conducted. This led to the selection of the SESAM software, which includes GeniE, HydroD, and SIMA, for the subsequent simulations and analyses carried out in the thesis.

The chosen semi-submersible concept for this project is the INO-WINDMOOR FOWT, which is a research initiative funded by the Research Council of Norway, Equinor, Inocean, and other industry partners. Detailed documentation and description of the project can be found in the work by Souza et al.(2021). This article provides valuable information regarding the floater model and its associated wind turbine, and it was utilized during the thesis to validate the numerical models created.

Throughout the project thesis, numerical finite element panel models were developed using the GeniE module of the SESAM software to represent the floater's geometry, internal compartments, and free-surface. The properties presented in the reference article were used as a basis for modeling the floater. Additionally, frequency-domain analyses were conducted using the HydroD module. To ensure the desired accuracy, mesh convergence studies were performed on the models, and an appropriate mesh size was selected for the subsequent analyses. Due to simplifications in the HydroD studies, such as the absence of the mooring line system, turbine tower, and components, compensatory measures were implemented by incorporating additional horizontal external stiffness and mass properties. Similar to Souza et al. (2021), a 5% critical damping was included in the heave, roll, and pitch directions to account for viscous damping in the model. In addition to examining the intact floater, the project thesis also investigated the inclusion of ballast water by generating various loading conditions corresponding to different ballast mass distributions. The dynamic effects of the internal ballast water were also explored.

The frequency-domain analyses conducted during the project exhibited favorable agreement with the reference values provided by SINTEF. To validate the model, the hydrodynamic added mass and damping results were compared to the reference values. Table 1.1 presents a comparison of the natural periods of the model with the reference values from the SINTEF article.

DOF	**Period SINTEF [s]**	**Period panel model [s]**
Heave	17	17
Roll	31	31
Pitch	31	31

Table 1.1: Natural periods comparison with SINTEF (Souza et al., 2021)

Following the satisfactory outcomes of the frequency-domain analysis, additional emphasis was placed on exploring the influence of ballast water and its associated effects. Through this exploration, it was observed that when utilizing partially filled compartments without internal sloshing resistance, resonant effects would arise, leading to distorted results. Consequently, a decision was made to narrow the focus solely to the damaged compartments, rather than all internal compartments. This deliberate choice allowed for a specific examination of the damage scenarios and a comprehensive assessment of the overall impact of such damage.

1.4 Objectives

The overall target of this master thesis is the investigation of the effect of damaged compartments for a chosen semi-submersible FOWT design during critical environmental conditions. This will be done by the use of the chosen state-of-the-art numerical prediction tools chosen during the course of the project thesis. The more interesting aspects to look into for this thesis are the dynamic behavior and motion of the FOWT, the natural periods, resonance and instabilities, the environmental

force contributions and mooring line tensions. These parameters are to be investigated by the means of frequency-domain analyses as well as time-domain simulations by the inclusion of all the FOWT components.

1.5 Thesis Structure

The structure of the master thesis is presented below:

- **Chapter 2** Summarizes a literature study performed on the causes and occurrences of damage on FOWTs, modeling and simulation tools, second-order wave forces on FOWTs and sloshing in tanks.
- **Chapter 3** Presents the theoretical information applied in numerical analyses and simulations in the project.
- **Chapter 4** Provides an overview of offshore substructure concepts, and introduces the FOWT design used in this thesis.
- **Chapter 5** Presents information on the choice of site, and the environmental data used to generate the environmental load cases that were applied in the time-domain simulations.
- **Chapter 6** Describes the software and methodology applied in the thesis.
- **Chapter 7** Presents the model assessment by the means of frequency-domain analyses, convergence studies, decay-, regular wave- and performance tests.
- **Chapter 8** Displays the results from the analyses, and provides analyses in the assessment of the dynamic behavior of the damage cases
- **Chapter 9** Documents a discussion of the findings from the thesis
- **Chapter 10** Provides a conclusion and suggestions for further work

2 Literature Review

A comprehensive literature review was undertaken to establish a foundation of preliminary knowledge and motivation for the master project and thesis. The review encompassed a thorough examination of significant works and studies conducted in fields directly relevant to the subject matter of the master thesis.

2.1 Causes and Occurrences of Damage on FOWTs

This section provides a comprehensive literature review focusing on the causes and incidences of damage to FOWTs. As the transition from the demonstration phase to the commercial phase of FOWTs is currently in progress, a primary objective of this stage is to minimize construction costs (Chujo et al., 2020). Numerous commercial projects are currently underway, accompanied by ongoing research aimed at addressing challenges and identifying effective solutions.

Concurrently, extensive research is underway to assess the likelihood of accidental occurrences involving FOWTs (Chujo et al., 2020). Given the scarcity of documented data on such incidents, these studies play a vital role in determining the significance of various hazards. Probabilities in these studies are often calculated using automatic identification system (AIS) data, followed by finite element method (FEM) analysis to evaluate the likelihood of structural failure. This provides an effective overview of the events that can cause damage to FOWTs. According to Chujo et al. (2020), the main causes of damage to FOWTs are environmental forces, mooring ability, and collisions with ships. These hazards can be further categorized into different accident scenarios, providing a useful framework for understanding the potential causes of damage. One area of increasing focus in FOWT research is the potential for collisions with ships. Given the proximity of FOWT farms near the coastal regions and main shipping routes, there are risks of such collisions (Chujo et al., 2020). As offshore farms continue to expand, examining the consequences of such accidental events is crucial.

Rypestøl (2020) conducted a comprehensive analysis of the OO-Star Wind floater, a post-tensioned concrete structure (Rypestøl, 2020). The study specifically investigated the impact scenarios involving broadside collisions and collisions with a bulbous bow, employing global response analysis in USFOS to simulate these events. The findings of the study revealed the possibility of punching shear effects and compartment flooding as significant outcomes. Consequently, these investigations underscore the substantial risks associated with accidental collisions involving service vessels.

Work by Wang et al. (2021) presents modeling and local analyses of the LIFES50+ and OO-Star wind floaters in LS-DYNA. The study considered several scenarios, including variable wall thicknesses and vessel speeds. The results showed structure accelerations, stresses, mooring forces, and force-displacement relationships. The study also highlighted several significant effects for different scenarios and the potential for flooding.

Zheng et al. (2018) conducted a study on the dynamic response of a semi-submersible

platform supporting a 5 MW wind turbine, known as the OC4 DeepCwind semi-submersible. In this study, ANSYS-AQWA was used to simulate the coupled system subjected to wind and waves. The study simulated three types of damage to the base column, and the results showed the significant impact on the platform stability, particularly in roll and yaw motions.

In 2023, on the 23rd of April, a collision event occurred between a cargo ship and a turbine at the Gode Wind 1 offshore wind farm. After this event, the turbine was taken out of service and extracted for inspection ((an$_l ee$), 2023). Luckily, there were no injuries, but despite this, the event signifies the importance of planning emergency solutions in the case of such emergencies.

This literature review aimed to identify existing research concerning the dynamic response of damaged FOWTs. The lack of extensive literature on this topic underscores the potential advantages of conducting further investigations in the expanding FOWT industry. Specifically, there is a need for in-depth exploration of the damage stability of these structures and the implications of coupled mooring-system configurations. Undertaking such research could greatly contribute to the continued growth and development of the FOWT industry.

2.2 Modeling and Simulation

This section provides a comprehensive examination of the numerical modeling and simulation tools frequently employed in the domain of FWTs. The primary focus of the study is to explore the practical applications of these tools in analyzing the behavior of FWTs under diverse conditions. The findings of this study are highly pertinent for gaining insights into the present status of the field and identifying the available resources for conducting research on FWTs.

FOWTs are structures that are affected by a variety of forces, including hydrodynamics, aerodynamics, structural dynamics, mooring line dynamics, and control dynamics. These forces can be modeled using either a rigid body or a flexible body approach. Because of the coupling between environmental and structural forces, the simulation tool must be able to handle these couplings in an effective manner (Bachynski-Polic, 2022b). One efficient way to analyze the substructure of a FOWT is through frequency domain analysis. This type of analysis may be performed in Wadam, which is integrated into HydroD and the SESAM package. The output of this analysis is the hydrodynamic coefficients at a given set of frequencies and wave headings. The hydrodynamic coefficients can also be obtained using time-domain analysis in Wasim, which uses the Rankine panel method (DNV, 2022b). However, these tools do not consider coupled effects.

To perform coupled analyses, several options are available. Two examples are OrcaFlex and the SIMA workbench. The SIMA workbench has the advantage of being integrated into the SESAM package, making it easier to move system properties in-between different analyses. The SIMA workbench is a complete tool for simulating marine operations, from modeling to results presentation. It is a platform for various calculation programs, including SIMO and RIFLEX (DNV, 2022b). By

combining Wadam and HydroD, it is possible to perform first- and second-order hydrodynamic analysis and transfer the results to SIMA for further use. One benefit of using SIMA compared to other solvers is the ability to script the solution procedures using JavaScript (DNV, 2022b). This allows the user to model, define parameters, and perform the simulations using code. In today's computational environment, the ability to combine multiple solver programs into a single code can save time and effort.

SIMA consists of several components, including RIFLEX, which is a finite element code that provides nonlinear static and dynamic analysis of slender systems such as mooring lines, wind turbine blades, and risers (DNV, 2022b). SIMO is a time-domain solver that simulates the motions and station-keeping of complex floating systems, taking into account environmental forces such as waves, wind, and currents. SIMO also includes the integration of Morison's equation for slender elements. This tool is also available through the integration of HydroD, and in both programs, the user can define slender elements, and the loads resulting from these elements are calculated.

This thesis employs HydroD with Wadam for conducting frequency-domain analyses due to its seamless integration and compatibility for ongoing analyses. Additionally, SIMA will be utilized for performing the coupled analysis. A comprehensive description of the tool will be provided within the thesis, offering detailed insights into its functionalities and capabilities.

2.3 Second-order Forces

Frequency domain analyses are commonly used in the FOWT industry to determine hydrodynamic coefficients, natural periods, wave excitation forces, and motions (DNV, 2022b). Second-order effects, which describes the effects that arise due to the nonlinear nature of fluid flow, require more computational effort and hence, time to analyze. This literature study examines the importance of these forces for semi-submersible FOWTs to determine the significance of these hydrodynamic effects and potential simplifications.

Bayaty et al. (2014) studied the second-order hydrodynamic effects on the OC4-DeepCwind semi-submersible supporting a 5 MW reference wind turbine. The structure was simulated under induced loads and motions for various wave conditions. The goal of this research was to assess the effects of second-order hydrodynamic loads and motions at the sum and difference frequencies of the incoming waves. The second-order hydrodynamic forces were computed using WAMIT for all degrees of freedom. The paper also discusses the possibility of approximating the difference-frequency quadratic transfer functions (QTFs) by manipulating the diagonal values within the framework of Newman's approximation. This approximation is valid when the natural frequencies of slowly varying motions are small, as in the case of the paper. However, the paper also notes some drawbacks of this approximation for shallow water, broad-banded sea states, or sea states with wave direction spreading. FAST is an offshore simulation tool. At the time of the study, FAST was not configured to use second-order QTFs produced by WAMIT, so the assessment was

conducted using WAMIT only.

The model of the turbine was included using global mass and stiffness parameters as external matrices derived from a FAST linearization procedure. The results showed the presence of difference-frequency hydrodynamic effects at the natural frequencies of the semi-submersible, which was designed for the lower end of the wave spectrum. When comparing the results to experimental data from the Maritime Research Institute Netherlands for the same concept, the response estimated by WAMIT was found to be an over-prediction due to the lack of viscous drag.

Zhang et al. (2020) studied the second-order effects on three semi-submersibles supporting 5 MW reference turbines. The objective of the research was to compare the hydrodynamic response of the semi-submersibles in different water depths and loading conditions. The effects of second-order forces were estimated using both Newman's approximation and the full QTFs. For the environmental load cases, three scenarios were selected. For the first-order frequency domain analysis, AQWA-NAUT was used. The mean-drift forces were calculated using the far-field and near-field approach in the AQWA-DRIF module.

In terms of the dynamic motion response, the results provide insight into the excitation of responses at the natural frequencies of all the motions occur due to difference-frequency wave forces. This is shown for all of the semi-submersible designs assessed, and is shown to be significant for the pitch motion. The results also highlight the benefits of using Morison drag for a more accurate representation of the motion responses. In terms of the second-order forces, the results highlight an increasing effect for shallower conditions. Comparing Newman's and the full QTFs, Newman's approximation proves suitable in terms of determining the resonant surge motions, but in the case of the other degrees of freedom proves less accurate. Hence, the full QTF approach is recommended in terms of modeling the difference-frequency effects.

2.4 Sloshing in Tanks

Sloshing is a phenomenon that occurs when liquid with a free surface is contained in a structure that is free to move (Faltinsen et al., 2009). The movement of the liquid within the container is caused by the movement of the structure containing the liquid due to the fact that the free-surface remains horizontal (Faltinsen et al., 2009). The fluid motion in the tank can be critical for the structure if the natural period of the fluid motion is in the vicinity of a period corresponding to significant motion of the structure. Additionally, the lack of damping associated with fluid motion can also cause problems for the structure (Faltinsen et al., 2009). This literature study aims to provide a better understanding of the importance of fluid motion in damaged compartments and tanks.

Shen et al. (2020) looked into closed fish-farm concepts and the effects of sloshing. The main objective was to develop a numerical tool for the response of the structure. For the internal motion, to estimate the forces due to sloshing, internal potential flow was solved by the means of harmonic polynomial cell method. Two

cases were examined in these studies. For the first case, sloshing inside a forced oscillatory rectangular 2D tank was investigated while undergoing forced oscillations. The investigations highlight a close correlation between the wave elevation and sloshing force through the simulations. The second case performs investigations on a rectangular-shaped closed cage freely floating while exposed to waves. For this case, studies from experimental tanks have also been included. For this case, three conditions were studied which differed by the means of filling fraction. Overall this case provides good insight into the sloshing effect on the overall motions of the structure. The investigations also show that linear modal numerical solutions can provide reasonable predictions of the motion of the cage for the two tanks.

Mohd Atif Siddiqui's Philosophiae Doctor thesis investigated the experimental and numerical hydrodynamic analysis of a damaged ship section in waves (Siddiqui, 2020). The thesis included experiments, decay tests, flooding tests, and numerical work. One important finding from the thesis is that in general, for a closed partially-filled tank/compartment, the lateral motions (sway or roll) can excite sloshing resonance, while according to linear theory (Faltinsen and Timokha, 2009), the vertical motions (heave) cannot excite resonant sloshing. It should be mentioned that for this, it is assumed that the linear effects dominates the heave motion features. The study also demonstrates the lost buoyancy method, for the calculation of equilibrium conditions after flooding. This could be useful for damage stability calculations of offshore structures. The numerical work performed in the thesis included calculations with WAMIT, which showed that the software is capable of accurately describing the effects and resonance frequencies of sloshing.

2.5 Applied Static Inclinations in Potential Flow Methods

Potential flow methods are a set of mathematical techniques employed to analyze the behavior of fluid flow. These methods rely on the assumption that the fluid being studied is incompressible, inviscid, and irrotational, meaning it lacks internal friction and cannot be compressed or expanded. In potential flow, the fluid's velocity can be determined through a scalar function known as the velocity potential, which adheres to Laplace's equation. Potential flow methods offer the advantage of being relatively straightforward to apply and can yield valuable insights into fluid behavior without the need for complex numerical simulations. However, it is important to note that these methods have certain limitations as they do not consider the nonlinear effects of flow, which can be significant in specific applications.

When studying the impact of damage on offshore structures, the application of static inclinations becomes crucial in understanding subsequent behavior. Two primary methods are commonly used to investigate hydrodynamic loads: potential flow methods and computational fluid dynamics (CFD). CFD, a branch of fluid mechanics, employs numerical methods and algorithms to analyze and solve complex fluid flow problems. Although CFD is computationally more demanding, it is worthwhile to examine the potential flow methods' ability to assess the resulting effects of applied static inclinations.

In a study conducted by Siddiqui et al. (2022), a comparison was made between

CFD and potential flow methods concerning hydrodynamic loads on fixed offshore wind turbines (FOWTs). The researchers performed potential flow and CFD simulations on the UMaine Volturn US-S fixed floater under regular wave conditions. The study primarily focused on mean wave-drift forces in the surge direction, considering different wave headings, wave heights, and mean pitch angles. The results indicated significant disparities between the two calculation methods, particularly when accounting for mean pitch angles. The findings suggest that CFD may better capture the effects of static pitch angles, but further investigation is necessary to comprehend the underlying physical phenomena.

For potential flow methods, it is also recommended to calculate mean-drift forces using full Quasi-Steady Transfer Functions (QTFs) to enhance accuracy in capturing the associated effects.

3 Theory

The subsequent Section provides an overview of the theoretical information applied in the software later in this thesis. The theory consists of hydrodynamic theory which is applied in both HydroD and SIMA. This theory is based primarily based on Sea loads on ships and offshore structures (Faltinsen, 1999), and the compendium for the subject Marine Dynamics (Bachynski et al., 2021). Secondly, some rules and regulations from DNV are included as an indication of relevant requirements for floating offshore structures. Third, some additional theory on aerodynamics is included. This theory is mainly based on lectures and lecture material from the course Integrated dynamic analysis of wind turbines (Bachynski-Polic, (2022)).

3.1 Description of Waves

This subsection is based on Bachynski et al. (2021). Regular waves are a basic way of describing periodic wave conditions, and are seen as a simplification of the real system of a realistic sea state. For the simulation of a floating semi-submersible, the realistic irregular wave theory is preferred. Irregular wave theory treats the representation of the sea in a statistical manner by combination of regular waves. The surface elevation is described by combination and superposition of a number of long-crested waves described as

$$\zeta(x,t) = \sum_{n=1}^{N} \zeta_{An} cos(\omega_n t - k_n x + \epsilon_n) \tag{1}$$

where ζ_{An} is the wave amplitude of the linear wave component with frequency ω_n, t is the time, k_n is the wave number, x is the particular horizontal location and η_n is the phase angle.

In this manner of representing irregular sea states, there are three common assumptions stated as follows

- The wave process is stationary, i.e, within a short time interval (20min-3h) the mean value and variance of the process is constant
- The wave elevation is normally distributed with variance and zero mean
- The wave process is ergodic, i.e., a simple time series could be representative of the wave process. The variance and expected value will then be calculated by time-averaging one time-series

The common way to represent this further is by the generation of a wave-spectrum $S(\omega)$. This spectrum describes the energy content of the waves with respect to the corresponding frequency-domain. The relation between the frequency-domain spectra and the physical waves may be stated as follows

$$\frac{\zeta_{An}^2}{2} = S(\omega_n)\Delta\omega \tag{2}$$

This is defined as the area within a frequency interval of size $\Delta\omega$ representing the energy content of all the wave components within the interval. From this, the total energy density in a sea state may be described as:

$$\frac{E}{\rho g} = \sum_{n=1}^{N} \frac{\zeta_{An}^2(\omega_n)}{2} = \sum_{n=1}^{N} S(\omega_n)\Delta\omega \tag{3}$$

where ρ is the density of sea water and g is the gravitational constant.

The wave spectrum contains all the statistical properties of the wave elevation of the sea state described. These are normally defined by the use of spectral moments which are calculated as follows

$$m_n = \int_0^\infty \omega^n S(\omega) d\omega \tag{4}$$

where n is the moment order. From these, one may extract other properties that are significant in representing the sea state in a more understandable manner. This is done by the introduction of parameters significant wave height, and peak period.

The significant wave height, H_S is the average height of the highest one-third of waves in a given sea state. By the means of spectral moments, one way of calculating it is by:

$$H_S = 4\sqrt{m_0} \tag{5}$$

The spectral peak period, T_P, is defined as the period at which the wave spectrum exhibits its maximum value.

3.1.1 Wave Spectrum

The principle behind the correlation between wave spectra and real sea state was introduced in the past section. Sea states are random processes. In regards to the visual representation, different standardized wave spectra have been developed corresponding to several conditions and locations. In hindsight, these are specific models based on observations and recordings of sea states in several locations. In most cases, these are expressed by the means of H_S and T_P.

The JONSWAP Spectrum

The JONSWAP("Joint North Sea Wave Project")-spectrum is a representation of wave conditions in the North Sea and is commonly used to describe sea states in ocean engineering. It is based on the standardized Pierson-Moskowitz (PM) spectrum, but includes a sharper peak to account for the higher wave energy observed in the North Sea during the Joint North Sea Wave Project (1968-1969) (Bachynski et al., 2021). The spectrum is typically described by the following equation

$$S(\omega) = \alpha \frac{g^2}{\omega^5} exp\left[-\frac{5}{4}\left(\frac{\omega_p}{\omega}\right)^4 \right] \gamma^{exp\left[-\frac{1}{2}\left(\frac{\omega-\omega_p}{\sigma\omega_p}\right)^2 \right]} \tag{6}$$

Here, α is a scaling factor, γ is the peak enhancement factor, σ is the spectral width represented in Equation 7 and ω_p is the peak frequency.

$$\sigma = \begin{cases} 0.07 & for \qquad \omega \leq \omega_p \\ 0.09 & for \qquad \omega > \omega_p \end{cases} \tag{7}$$

Another important aspect of the JONSWAP spectrum is its use of the gamma parameter, γ, which is used to describe the steepness of the wave spectrum. The gamma parameter is defined as the ratio of the wave height to the wave length. By adjusting the gamma parameter, one can model different sea states, from relatively calm to very steep and rough seas. This makes the JONSWAP spectrum a versatile tool for modeling wave conditions in a variety of environments.

3.2 Hydrodynamic Theory

For the master thesis, the objective is focused on a floating semi-submersible platform in deep waters. This is why the focus of the theoretical notations will be directed towards deep-water theory, and hence, h/λ(water depth/wave length) $\geq$ 0.5 is required. For performing a mesh convergence study, but also validating the model, first order analyses in Wadam will be performed. The analyses are based on performing first-order frequency domain analyses by the calculation of radiation and diffraction effects on the modeled structure. The hydrodynamic theory presented is mainly based on Faltinsen (1999).

3.2.1 Linear Wave Theory

The velocity potential is a significant part of all hydrodynamic modeling. It's a mathematical term used to describe the fluid flow field. For an incident free-surface regular wave in finite water depth, the velocity potential is defined as

$$\phi(x, y, z, t) = \frac{g\zeta_a}{\omega} \frac{coshk(z+h)}{cosh(kh)} cos(\omega t - kx) \tag{8}$$

where ζ_a is the wave amplitude, $\omega = 2\pi/T = \sqrt{gk}$ is the wave frequency expressed in the form of the deep water relation, z is the distance to the surface, in which z = 0 defines the free surface, h is the average water depth, k = $2\pi/\lambda$ is the wave number. Considering the application of deep-water theory, the formulation of the velocity potential may be simplified to

$$\phi(x, y, z, t) = \frac{g\zeta_a}{\omega} e^{kz} cos(\omega t - kx) \tag{9}$$

The relation between pressure, velocity, and elevation in a fluid may be expressed by a fundamental principle in fluid dynamics. This principle is based on the conserva-

tion of energy within fluid flow, and is called the Bernoulli equation. This equation is expressed as:

$$p - p_a = -\rho g z - \rho \frac{\partial \phi}{\partial t} - \frac{1}{2}\rho |\nabla \phi|^2 \tag{10}$$

Here, p is the pressure at the specific point in the fluid, p_a is the atmospheric pressure and ρ is the density of seawater. The Bernoulli equation assumes that the fluid flow is steady, incompressible, inviscid, negligible external forces and that the flow is along a streamline. These assumptions simplify the equation, but they also limit its applicability to certain situations. Another governing principle is the Laplace equation stating that the flow is irrotational as

$$\nabla^2 \phi = 0 \tag{11}$$

Which is valid within the fluid domain Ω analyzed. In addition to the governing equations, there are several boundary conditions to take into account. The first one being the impermeability condition, stating that surfaces such as the sea-bottom and body are impermeable as

$$\frac{\partial \phi}{\partial n} = 0 \tag{12}$$

on the surface of the sea-bottom, and

$$\frac{\partial \phi}{\partial n} = V_B \cdot n \tag{13}$$

On the body surface. Here, V_B is the body velocity, and n is a normal vector pointing outwards from the body. In addition to the impermeability condition, one also has the free-surface kinematic condition. This states that fluid particles on the free surface remain there as

$$\frac{D(z - \zeta)}{Dt} = 0 \tag{14}$$

on z = ζ(x,y,t). The last boundary condition also refers to the free surface, and it states that the pressure at the free surface is equivalent to the ambient pressure p_a. This refers to the velocity potential of the fluid as

$$g\zeta + \frac{\partial \phi}{\partial t} + \frac{1}{2}\left[\left(\frac{\partial \phi}{\partial x}\right)^2 + \left(\frac{\partial \phi}{\partial y}\right)^2 + \left(\frac{\partial \phi}{\partial z}\right)^2\right] = 0 \tag{15}$$

On z = ζ(x,y,t). The reasoning behind the two boundary conditions for the free surface comes from there being two unknowns in regards to it. One has both an unknown velocity potential, but also the unknown wave amplitude ζ. The velocity potential may be further developed in the radiation and diffraction problem.

3.3 Linear Potential Wave Loads

In hydrodynamics, linear theory refers to the approach of linearizing the equations governing the fluid motions in order to simplify the analysis of small disturbances

in fluid flow. For this, one assumes that the disturbances in the fluid flow are small, and that they don't affect the overall flow field in a significant manner. Due to the linearity of the sea-keeping problem, one may apply superposition and hence, decompose the potential into two sub-problems. The diffraction problem assumes the body is fixed and interacting with the incident waves. The flow due to the incident waves penetrates the body with a normal velocity as if it wasn't there. The loads caused by this effect are called Froude-Kriloff loads. To recover the state of the body, it diffracts waves outwards, causing a flow in the opposite direction with respects to the incident waves. The velocity potential is then defined as

$$\phi(x, y, z, t) = \phi_0(x, y, z, t) + \phi_D(x, y, z, t) \tag{16}$$

Where ϕ_D is the diffraction potential with Laplace equation as its governing equation, and ϕ_0 is the incident wave potential. The sum of the Froude-Kriloff- and the diffraction loads results in the wave excitation loads.

The radiation problem on the other hand assumes the body being forced to oscillate in all its degrees of freedom with frequency ω. The result of this event are radiated waves as a result of the body motion. In this problem, the waves and their contributions are neglected. The velocity potential resulting from this problem is specified as

$$\phi(x, y, z, t) = \phi_R(x, y, z, t) \tag{17}$$

and it may be split into six sub-problems for each DOF. The governing equation for this problem is also the Laplace equation. The hydrodynamic loads resulting from this problem are defined added mass, damping and restoring. Here, the added mass and damping terms are in connection with the dynamic pressure due to the motions, while the restoring terms are due to the varying buoyancy due motions. In linear wave theory, the body-motion amplitude is calculated assuming that the response amplitude is proportional to the excitation loads. In hindsight, this means the body oscillates with the same frequency as the frequency of the disturbance. Considering this, one may solve a problem only dependent on the frequency ω, a frequency domain analysis. This is a consequence of the linearization of the problem, and hence, assuming that the non-linearities are negligible.

The wave excitation forces in each DOF are obtained from the previously described diffraction problem. When the velocity potentials are solved for, one may apply Bernoulli to obtain the dynamic pressure as

$$p_d = -\rho \frac{\partial \phi_0 + \phi_D}{\partial t} = -\rho \frac{\partial \phi_0}{\partial t} - -\rho \frac{\partial \phi_D}{\partial t} \tag{18}$$

Then, the wave excitation loads are obtained by multiplying the dynamic pressure by the body normal vector n_j in each DOF, and then integrating over the body mean wetted surface S_0 as

$$F_j^{ext} = \int_{S_0} p_d n_j dS \tag{19}$$

where j specifies the degree of freedom. The radiation problem on the other hand, is associated with the velocity potential radiated when the body generates waves and disturbs the surface. The loads resulting from this problem are formulated by the

means of added mass, damping and restoring coefficients.

$$-A_{ij}\ddot{\eta}_i - B_{ij}\dot{\eta}_i - C_{ij}\eta_i = F_{ij}^{RAD} \tag{20}$$

Here, A_{ij} is the frequency-dependent added mass, B_{ij} is the frequency-dependent damping, C_{ij} is the hydrostatic restoring, and F_{ij}^{RAD} is the radiation load in direction i due a change in buoyancy as a consequence of body motions.

3.3.1 Solving the Radiation Diffraction Problem

Wadam is an analysis program for calculation of wave-structure interaction. The solution is calculated in the frequency domain. In this approach, one solves the steady-state response as one calculation per wave frequency, producing response amplitude operators. If one were to use linear (time-domain) for the approach, one would have to wait for transients to die out before continuing on the next condition (Bachynski et al., 2021). Considering the interest of the solution often being the steady state response, in many cases, it would be faster to proceed with the frequency domain solution.

This means that by defining the frequency range to solve the problem in, one solves the equation to find the amplitude and phase of the problem. The output results from the analysis will be presented in a file containing a description of the velocity potentials, added mass, damping for each frequency, force- and motion transfer functions listed by frequency and wave heading.

3.3.2 Non-Linear Wave Theory

In the context of second-order wave theory, the problem of wave-body interaction considers a perturbation approach in which retains both the linear and second-order effects in the model. This theory provides a more accurate representation of the fluid pressure on the instantaneous free-surface, the non-linearities in the velocities of fluid particles at the free-surface, and the zero-normal flow condition through the body (Faltinsen, 1999). Second-order loads are particularly important in the design of mooring systems, the capsizing of semi-submersibles, and the added resistance due to the waves.

When examining a moored floating structure, the dependence on the difference-frequency effect is significant. This is because the natural periods of the floating body in horizontal degrees of freedom may be excited, leading to resonant motions. Understanding these second-order effects is crucial for the design and operation of offshore structures.

Mean Drift Forces

Looking at the mean wave-loads, they may be especially important for the design of mooring systems, added resistance in waves, and analysis of oscillations in waves

(Faltinsen, 1999). For potential flow modeling of a floating body, the wave drift forces are a result of the body's ability in causing waves. For semi-submersibles the mass forces are likely to dominate, and in this case, the drift forces are in general small. Despite this, viscous effects may contribute, and the significance may vary (Faltinsen, 1999). When performing calculations of the mean drift forces, its not required to solve the second order problem. This occurs due to the pressure resulting from the second order velocity potential having zero mean, and hence, not contributing to the mean drift forces. There are several applicable ways of solving for the mean drift forces. The least demanding one being the use of equations for conservation of momentum in the fluid in the vicinity of the body surface as

$$M(t) = \int \int_{\Omega} \int \rho V d\tau \tag{21}$$

where V is the fluid velocity and Ω is the fluid domain. By integrating, applying Gauss theorem, and rewriting the equation for an incompressible fluid, one ends up with

$$\frac{dM}{dt} = -\rho \int_S \int \left[\left(\frac{p}{\rho} + gz \right) n + V \left(V_n - U_n \right) \right] ds \tag{22}$$

where $V_n = \partial\phi/\partial n$ is the normal component of the fluid velocity at the surface S, p is the pressure, g is the gravitational constant, z is the height following rewriting using Euler's equation, and V_n is the fluid velocity component normal to the body surface. By time averaging the equation, neglecting the components that don't affect the horizontal degree of freedom, over one period of oscillation, one finds that the resulting mean horizontal force may be calculated as

$$\bar{F}_i = -\overline{\int_{S_\infty} \int [p n_i + \rho V_i V_n] ds} \qquad i = 1, 2 \tag{23}$$

where S_∞ is the time-dependent control surface within the water domain, and V_i is a component of the fluid velocity.

For the direct pressure integration, one calculates the pressure over the wetted surface, in which the computed pressures are integrated over the whole wetted control surface. This allows one to calculate the net force exerted by the fluids on the body. The direct pressure integration method is generally considered to be more computationally expensive compared to the conservation of momentum approach.

Slow-Drift Motions

Slow-drift motions are resonant oscillations that are excited by the non-linear interaction between waves and the motion of a body. These types of motions are commonly observed in moored systems, such as a floating semi-sub. The slow-drift motions typically occur in the surge, sway, and yaw directions (Faltinsen, 1999). For moored systems, the control forces due to the mooring will counteract the mean environmental forces. These control forces are small compared to the first order forces, and cannot withstand these. The second-order difference frequency effects may excite resonance of the slow-drift motions of the mooring system. This is due

to the periods of the second-order forces and the mooring system being large compared to the ones of the first-order forces. The slow drift motions can't be excited by the interaction with a single regular wave, but is connected with the difference-frequency effect. Hence, for the occurrence of these effects, waves with different frequencies have to be present. The formal equation for the slow-drift excitation load is expressed by Faltinsen (1999) as

$$F_i^{SV} = \sum_{j=1}^{N}\sum_{k=1}^{N} A_j A_k [T_{jk}^{ic} cos((\omega_k - \omega_j)t + (\epsilon_k - \epsilon_j)) + T_{jk}^{is} sin((\omega_k - \omega_j)t + (\epsilon_k - \epsilon_j))] \quad (24)$$

Where A_i are the wave amplitudes, ω_i are the wave frequencies, ϵ_i are the random phase angles and N is the number of wave components. T_{jk}^{ic} and T_{jk}^{is} are the second-order quadratic transfer functions of the difference frequency loads. The quadratic transfer functions may be calculated by the use of software such as HydroD and Wadam. In order to do this, one's required to generate a panel model of the free surface as well. Then the second-order analysis is performed utilizing direct pressure integration, which is known to be a computationally heavy process.

3.4 Morison's Equation

Morison's equation was introduced as a way of estimating wave loads on circular cylindrical structures (Bachynski et al., 2021). The equation is a semi-empirical and assumes the structure to be an upright cylindrical body shape that has a small cross-sectional size relative to the waves, meaning that the equation is a long-wave approximation. This induces important viscous effects which are quantified in the form of the two terms in the Morison equation. These are defined the drag- and inertia-term. The equation applies to 2-D sections as

$$F_m(t) = \rho \frac{\pi D^2}{4} C_M a(t) + \frac{1}{2} \rho D C_D u(t)|u(t)| \quad (25)$$

Here, C_M and C_D are the mass and drag coefficients which are commonly determined empirically, a is the acceleration of the fluid particles of the waves, D is the diameter of the cross-section and u is the velocity of the fluid particles. To obtain the total loads acting on the structure, one would integrate this equation over the wetted surface in the vertical direction. Morison's equation may be modified to account for body motions as

$$F_m(t) = \rho \frac{\pi D^2}{4} C_M a(t) - \rho \frac{\pi D^2}{4} (C_M - 1)\ddot{\eta}_1(t) + \frac{1}{2} \rho D C_D (u(t) - \dot{\eta}_1)|u(t) - \dot{\eta}_1| \quad (26)$$

in which $\ddot{\eta}$ is the body acceleration, and $\dot{\eta}$ is the body velocity. The equation is also possible to modify for inclined structures by the use of trigonometric identities. In this case, the force applied to the structure would be normal to the cylinder axis. In the case of current acting, one may also combine the wave particle velocity with the current velocity to estimate the effects resulting. As mentioned in section 2.2, the slender elements will be directly defined in SIMA, in which these calculations are implemented.

3.5 Linear Dynamic Response

This section is provided to describe the basics behind the response of a dynamic system. This is to be used further in the thesis for interpretation of the response and behavior of a 6DOF semi-submersible. The theoretical content is based on Bachynski et al. (2021).

The dynamics of a moving system is based on the equilibrium condition developed from Newton's second law, stating that a force acting on a body is equal to the body mass times its acceleration as:

$$\sum F(t) = m\ddot{u} \tag{27}$$

The sum of forces on the left side considers all force contributions to the system of the body. This includes both internal and external excitation loads. In most cases, it's useful to describe the components of the system as:

$$F_i + F_d + F_S + P(t) = 0 \tag{28}$$

Where $F_i = -m\ddot{u}$ is the inertia force, $F_d = -c\dot{u}$ is the damping force, $F_S = -ku$ is the restoring force, $u(t)$ is the response of the system and P(t) are the sum of external excitation loads of the system. This is known as the equilibrium equation. To find the solution to such an equilibrium equation, if one assumes steady-state conditions and that the excitation load is harmonic, one may form a reltation between the load and the response as:

$$P(t) = P_0 cos(\omega t + \alpha) = (-\omega^2 m + i\omega c + k)\tilde{x}e^{i\omega t} = m\ddot{u} + c\dot{u} + ku \tag{29}$$

where the complex part of the solution is neglected, and only the real part is included. Where ω is the frequency of the load and response, α is the phase angle included to allow the load to be truly harmonic, i is an imaginary unit, $\tilde{x}$ is the unknown response and P_0 is the real maximum load. By re-writing, and separating the unknown complex $\tilde{x}$, one arrives at the solution:

$$\tilde{x} = \frac{\tilde{P}}{(-\omega^2 m + i\omega c + k)} \tag{30}$$

From this, the particular solution is expressed as:

$$u_p(t) = \frac{P_0}{k} \frac{1}{\sqrt{(1-\beta^2)^2 + (2\zeta\beta)^2}} cos(\omega t + \alpha + \phi) \tag{31}$$

Where

$$\phi = tan^{-1}\Big(\frac{-2\zeta\beta}{1-\beta^2}\Big) \tag{32}$$

Here, $\beta = \omega/\omega_0$ is the frequency ratio defining the ratio between the load frequency and the undamped natural frequency of the system, $\zeta = c/c_{cr}$ is the damping ratio describing the damping relative to the critical damping of the system. By establishing a relation between the particular solution $u_p(t)$ and the static displacement

u_{st}, one may define the dynamic load factor DLF which describes the ratio between dynamic and static response for a given load:

$$DLF = \left| \frac{u_{p,max}}{u_{st}} \right| = \frac{1}{\sqrt{(1-\beta^2)^2 + (2\zeta\beta)^2}} \tag{33}$$

which as displayed, depending on the damping, the frequency, and the phase angle of the system. The DLF may be used in determining the increase in response as the load frequency approaches the natural frequency of the system which is expressed as resonance.

3.6 Stability

This section will provide an overview of the DNV-ST-0119 standard for FOWT structures produced by DNV. The standard consists of requirements, principles and acceptance criteria for objects, personnel, organizations and/or operations. The section also compares the standard for FOWTs up against DNV-OS-C301 which is an offshore standard for stability and watertight integrity of offshore units. In the hindsight of investigation of damaged FOWTs, the focus will be damage stability.

Compared to the increased development within the field of offshore wind, the DNV-ST-0119 standard is not updated at the same speed. In the coming years, one should expect an updated version containing more specific requirements. The standard ensures safety by using consequence class methodology. This means that the design is classified based on the consequences of failure. Two classes of consequence are specified as:

1. Consequence class 1, where failure is unlikely to lead to unacceptable consequence such as loss of life, collision with an adjacent structure, and environmental impacts.
2. Consequence class 2, where failure may well lead to unacceptable consequences of these types.

It also states specifically that "For FWT structures, which are unmanned during severe environmental loading conditions, the consequences of failure are mainly of an economic nature" and that "Unless otherwise specified, the floating structure and its station keeping system shall be designed to consequence class 1" (DNV, 2021). Considering the current development within the field, in which shared anchor mooring configurations have been investigated for use (Gao et al., 2009), and shared mooring which is considered for use in the long-term (H. Haslum, 2018), the consequences of failure may very well change to those expressed in consequence class 2. This may very well lead to damage on the overall mooring configuration, and hence, risk of collision with other structures. Considering Equinor's success using shared anchors, and their current development within shared mooring, it's likely that others within the industry adapt to similar methods.

For the floating stability requirements of the structures, the standard explains the minimum requirements. For the damage stability section of the standard, it specifically states that "For unmanned units, damaged stability is not a mandatory requirement". For units not complying with consequence class 1, the following requirements are stated:

10.3.1.6

Stability and buoyancy in damaged condition shall also be demonstrated in temporary conditions during transport, installation, maintenance and repair.

10.3.2.2

The unit should have sufficient reserve stability in damaged condition to withstand the wind heeling moment superimposed from any direction. In this condition the final waterline, after flooding, should be below the lower edge of any down-flooding opening

10.3.4.1

- Collision with ship with the following extent of damage to be applied in exposed areas as illustrated as an example for a column stabilized unit in Figure 3.1
- Vertical extent of 3 m occurring 3 m below to 5 m above the waterline under consideration, as shown to the right in Figure 3.1.
- Penetration of 1.5 m in normal direction to the outer hull, as shown to the right in Figure 3.1.
- Horizontal extent in tangential direction to the outer hull, dL, shall be taken as either 3 m or 1/8 of perimeter in case of a column (measured at the periphery). This implies that if watertight bulkheads are spaced at a shorter distance (dL), two or more compartments shall be assumed flooded, see Figure 3.2. For distance (dL) larger than 3 m, only one compartment needs to be flooded. Wherever damage of a smaller extent than the one specified above results in a more severe condition, such smaller extent shall be assumed.

10.3.4.2

For all damage scenarios set out in [10.3.4.1] the following survival criteria shall be met when applying the overturning moment according to [10.3.4.1]:

- The unit should reach a stable equilibrium condition without any down-flooding to occur

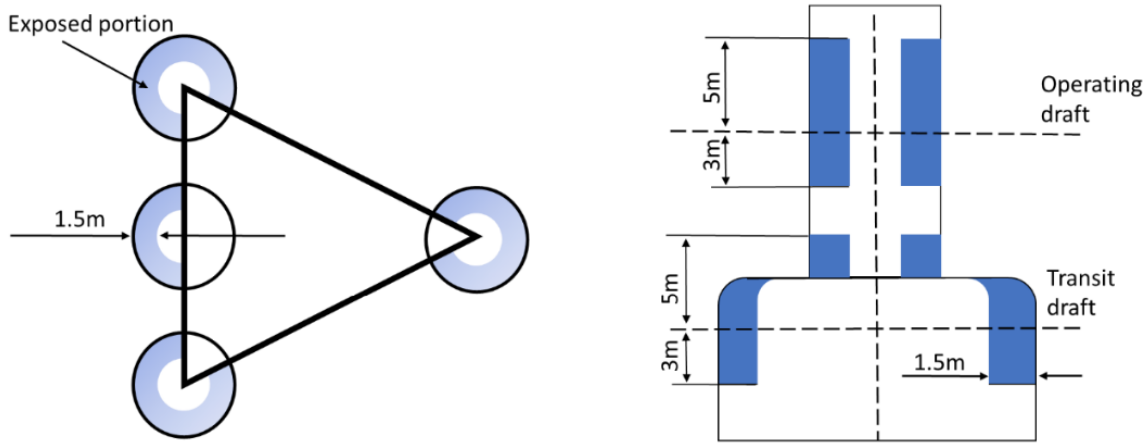

Figure 3.1: Exposed areas of a column stabilized unit (left) and vertical extent of damage (right) (DNV, 2021)

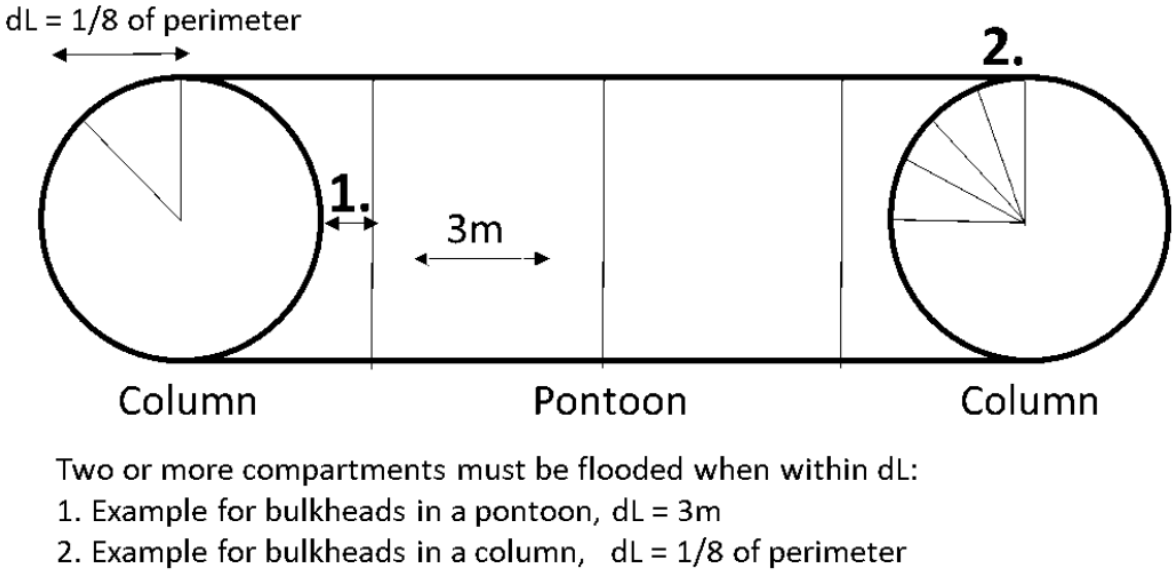

Figure 3.2: Horizontal extent of damage in tangential direction to the outer hull (DNV, 2021)

- For a TLP additional assessments shall be done in relation to the minimum and maximum tension criteria.

In conclusion, considering the consequence-class definitions, the damage stability criteria is close to non-existent, and not required. Looking at qualifications within DNV-OS-C301, the requirements stated are more direct. In general, for column stabilized units, the following is required:

5.4.1

The unit shall have sufficient free-board and be subdivided by means of watertight decks and bulkheads to provide sufficient buoyancy and stability to withstand a wind heeling moment induced by a wind velocity of 25.8 m/s (50 knots) superimposed from any direction in any operating or transit condition, taking the following considerations into account:

1. The angle of inclination after the damage set out in [5.9] shall not be greater than 17°
2. Any opening (through which progressive flooding may occur) below the final waterline shall be made watertight, and openings within 4 m above the final waterline shall be made watertight.
3. The righting moment curve, after the damage set out above, shall have, from the first intercept to the lesser of the extent of watertight integrity required by 2) and the second intercept, a range of at least 7°. Within this range, the righting moment curve shall reach a value of at least twice the wind heeling moment curve, both being measured at the same angle.

This means that being able to reduce angles of inclination by the use of actively ballasting compartments following damage, may not be seen as a justification of the requirements. DNV-ST-0119 doesn't mention this limitation, but assuming a similar development of the standard, it is to be expected in a coming edition.

5.9 - Extent of damage – column stabilized units, deep draught floating and tension leg units

In assessing the damage stability of such units, the following extent of damage shall be assumed:

1. Only those columns, underwater hulls and braces on the periphery of the unit shall be assumed to be damaged, and the damage shall be assumed in the exposed portions of the columns, underwater hulls and braces.
2. Columns and braces shall be assumed flooded by damage having a vertical extent of 3.0 m occurring at any level between 5.0 m above and 3.0 m below the draughts specified in the stability manual. Where a watertight flat is located within this region, the damage shall be assumed to have occurred in both compartments above and below the watertight flat in question. Lesser distances above or below the draughts may be applied upon consideration, taking into account the actual operating conditions. However, the required damage region shall extend at least 1.5 m above and below the draught specified in the operating manual.
3. No vertical bulkhead shall be assumed damaged, except where bulkheads are spaced closer than a distance of one eighth of the column perimeter at the

draught under consideration, measured at the periphery, in which case one or more of the bulkheads shall be disregarded.

4. Horizontal penetration of damage shall be assumed to be 1.5 m.

5. Underwater hull or footings shall be assumed damaged when operating in a transit condition in the same manner as indicated in 1), 2), 4) and either 3) or [5.6], having regard to their shape.

6. All piping, ventilation systems, trunks, etc., within the extent of damage shall be assumed damaged. Positive means of closure shall be provided at watertight boundaries to preclude the progressive flooding of other spaces that are intended to be intact.

7. All deep draught units shall comply with the damage stability survival requirements in [5.5] assuming flooding of any single watertight compartment located at or below the waterline corresponding to the maximum draught.

3.7 Mooring Line Theory

The control of both position and motion of a floating offshore structure is important. To keep the FOWT in its location, the semi-sub floater is connected to the seabed by the use of a mooring system. A catenary mooring system consists of cables in which the lower ends are anchored to the seabed. The anchoring lines provide restrictions to the offsets of the structure by the means of their own weight. This weight is applied in such a manner that the mooring lines induce stiffness upon the structure. The magnitude of this stiffness is decided upon during the design procedure. A typical catenary mooring system is displayed in Figure 3.3. In this figure, one may notice that the anchor is located a distance x_B away from the touch down point (TDP). This is due to the fact that the anchors are not capable of taking up the vertical excitation forces, and hence, the anchors are to lie on the seabed.

The mooring system applied to the INO-WINDMOOR 12MW FOWT for this thesis is described in Section 6.6. In order to establish this system, one has to perform inelastic static analysis of the system to estimate the required position of the anchors. For this thesis, this will be performed by the use of MATLAB with the catenary equations which are described in detail in Faltinsen (1999). The theory and equations applied for the static analysis assumes a horizontal seabed, assumes constant cable weight per meter, neglects the bending stiffness, neglects the dynamic effects in the line, neglects the current forces, and neglects the effects of elasticity. In order to find the minimum length of the suspended line l_s, the following equation may be applied as:

$$l_s = asinh(\frac{x}{a}) \tag{34}$$

Where x is the horizontal length of the suspended line defined in meters, and a is defined as:

$$a = \frac{T_H}{w} \tag{35}$$

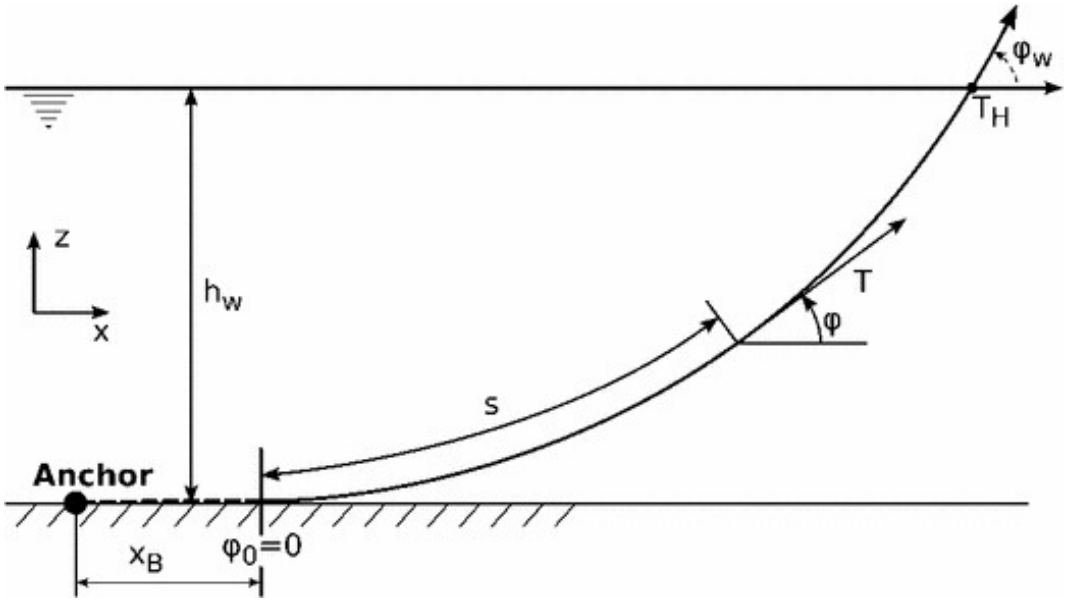

Figure 3.3: Mooring line system (Faltinsen, 1999)

Where T_H is the horizontal component of the tension specified at the water plane and w is the weight in N/m. The vertical span of the mooring line h is defined in the following manner:

$$h = a(cosh(\frac{x}{a} - 1)) \tag{36}$$

By combination and manipulation, one may end up with the following equation for the length of the suspended line:

$$l_s^2 = h^2 + 2h\frac{T_H}{w} \tag{37}$$

3.8 Aerodynamic Theory

This subsection will present the aerodynamic theory to be use for the coupled time-domain simulations in SIMA. The theory is mainly based on lecture notes from the modular subject integrated analysis of offshore wind turbines (Bachynski-Polic, (2022)).

Wind turbines are devices that convert the kinetic energy of wind into electrical energy. They consist of a rotor with blades, a nacelle containing the generator, a gearbox, and a tower. The rotor is spun by the wind, which turns the generator to produce electricity. Aerodynamics is the study of forces and the resulting motion of objects interacting with the wind. The blades of a wind turbine are designed to capture as much of the wind energy as possible. This requires careful consideration of the aerodynamic principles, and hence, it plays a crucial role in both the design- and operational processes of wind turbines.

3.8.1 1-D Momentum Theory

The initial method for calculating the power and thrust of an ideal rotor turbine involves examining a one-dimensional actuator disk model which is shown in Figure 3.4.

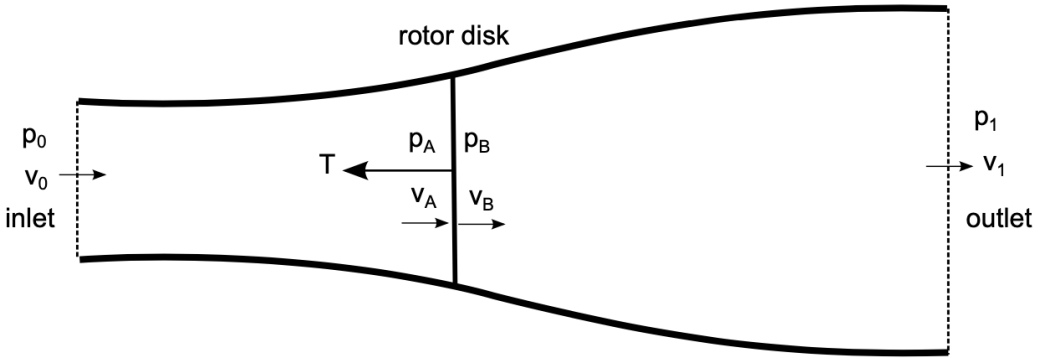

Figure 3.4: 1-D actuator disk rotor model Bachynski-Polic, (2022)

Here, the boundaries represent the boundaries of the stream tube, p and v are pressures and velocities at different locations of the control volume, and T is the thrust force from the actuator disk. In the model, one considers the two control volumes on each side of the disk. The assumptions used for the model as specified in Bachynski-Polic, (2022) are described as:

1. Homogeneous, incompressible, steady-state flow
2. No frictional drag
3. Infinite number of blades, and uniform thrust over the disk
4. Non-rotating wave
5. Pressure jump at the rotor disk with continuous velocity across the rotor disk
6. Pressure equal to ambient pressure far from the disk

By the establishment of the conservation of momentum between the inlet and outlet, one may express the thrust force from the actuator disk as given by Bachynski-Polic, (2022):

$$T = v_0(\rho A_0 v_0) - v_1(\rho A_1 v_1) \tag{38}$$

Where A_0 and A_1 are the areas of the inlet and outlet respectfully, and ρ is the density of air. By the use of conservation of mass between the control volumes, one may see that the mass flow rates is identical at the inlet and outlet. Hence, Equation 38 may be simplified to:

$$T = \dot{m}(v_0 - v_1) \tag{39}$$

For the quantification of the power, one may calculate the change in kinetic energy between the inlet and outlet as:

$$P = \frac{1}{2}\dot{m}(v_0^2 - v_1^2) \tag{40}$$

For simplification, the axial induction factor is introduced. This factor represents the relative change in velocity between the inlet and the rotor disk as:

$$a = \frac{v_0 - v_a}{v_0} \tag{41}$$

From this, one may derive expressions for the velocity at the disk and the outlet as:

$$v_a = v_0(1 - a) \tag{42}$$

$$v_1 = v_0(1 - 2a) \tag{43}$$

From these expressions, it may be seen that if the axial induction factor $a > 0.5$, the flow would stop behind the rotor. This would make the theory invalid and hence, not applicable. Furthermore, Equations 39 and 40 may be re-formulated by the means of the axial induction factor as:

$$T = \frac{1}{2}\rho A v_0^2 4a(1 - a) \tag{44}$$

$$P = \frac{1}{2}\rho A v_0^3 4a(1 - a)^2 \tag{45}$$

From this, one may express the power coefficient defined as the ratio of power extracted by the disk and the total power content of the incoming wind as:

$$C_P = \frac{P}{0.5\rho v_0^3 A} = 4a(1 - a)^2 \tag{46}$$

The theoretical maximum power coefficient may be found by taking the derivative of the power coefficient with respect to a, and setting it equal to zero. This leaves one with $a = \frac{16}{27}$. This is known as the Betz limit. This limit is the theoretical upper limit of the efficiency of a turbine. There are a couple of factors that make it impossible to reach this upper limit. Due to this, one is required more advanced theory for describing the aerodynamic phenomena in a sufficient manner.

3.8.2 Ideal Turbine with Wake Rotation

One of the reasons of why the 1-D momentum theory is not sufficient is the fact that it disregards the rotation of the airflow wake. When the air passes through the disk, the blades impose energy onto the wake in the form of rotation. To fully explain this phenomena by the means of equations, one has to introduce the angular induction factor a', the tip speed ratio λ, and the local speed ratio λ_r. The angular induction factor is defined as:

$$a' = \frac{\omega}{2\Omega} \tag{47}$$

Where ω is the angular velocity imparted to the free stream and Ω is the angular velocity of the rotor. The tip speed ratio (TSR) is defined as the ratio between the tangential speed of the blade to the actual wind speed as:

$$\lambda = \frac{\Omega R}{v_0} \tag{48}$$

Where R is the radius of the rotor. The local speed ratio is the same formula as the TSR but at a specific radius increment of the total blades r and is defined as:

$$\lambda_r = \frac{\Omega r}{v_0} \tag{49}$$

By this, one may express the ideal turbine power coefficient as:

$$C_P = \frac{8}{\lambda^2} \int_0^{\lambda} a'(1-a)\lambda_r^3 d\lambda_r \tag{50}$$

By this, one may notice that the power coefficient is a function of the TSR. For lower TSR, the turbine exerts a larger fraction of energy onto the airflow wake. For larger TSR, the power coefficient will approach Betz limit.

3.8.3 Blade Element Momentum Theory

Blade element momentum theory is a theory developed based on past work within the field of aerodynamics. It is a combination of the described momentum theory, and blade theory. The blade theory is a description of the behavior of airfoils. To describe the principles behind an airfoil, one would first refer to an illustration of an airfoil as in Figure 3.5.

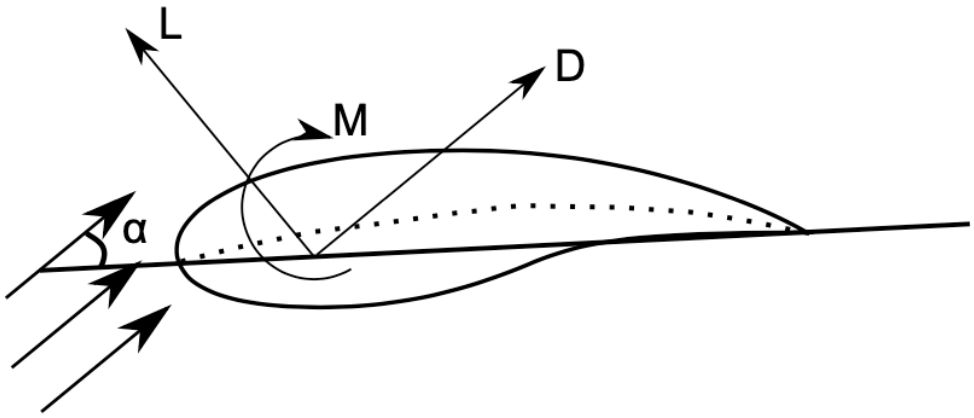

Figure 3.5: Airfoil Bachynski-Polic, (2022)

With reference to the figure, there are there are two forces acting on an airfoil due to wind. These are called the lift and drag and they are caused by a pressure differential between the upper and lower side of the foil. In addition the frictional force between

the surface of the foil and the wind contributes. This results in a lift force acting perpendicular relative to the direction of the incoming wind. A quantification of this force may be expressed in a 2D non-dimensional manner as:

$$C_l = \frac{L/l}{\frac{1}{2}\rho U^2 c} \tag{51}$$

Where l is the length of the foil perpendicular to the cross section, L is the lift force, U is the incoming relative velocity of the wind and c is the chord length. The lift force is in general the dominating force, and the driving factor of the rotation of the blades. The drag force on the other hand is a force acting parallel to the incoming wind. In a similar manner, the drag coefficient C_d may be defined as:

$$C_d = \frac{D/l}{\frac{1}{2}\rho U^2 c} \tag{52}$$

From this, one may define expressions for the thrust and torque of the airfoil sections as:

$$dT = 4a(1-a)\frac{1}{2}\rho v_0^2 2\pi r dr \tag{53}$$

$$dQ = 4a'(1-a)\frac{1}{2}\rho v_0 \Omega r^2 2\pi r dr \tag{54}$$

If one further looks at one section of the airfoil, one may identify one force normal to the rotor plane, and one tangential. In which the normal force is defined as:

$$p_N = Lcos(\phi) + Dsin(\phi) \tag{55}$$

Here, ϕ is accounts for the combined blade pitch angle and angle of attack α. With its non-dimensional coefficient defined as:

$$C_n = C_l cos(\phi) + C_d sin(\phi) \tag{56}$$

$$p_T = Lsin(\phi) - Dcos(\phi) \tag{57}$$

$$C_t = C_l sin(\phi) - C_d cos(\phi) \tag{58}$$

From this, the thrust and torque for the sections may be expressed as:

$$dT = B(Lcos(\phi) + Dsin(\phi)dr \tag{59}$$

$$dQ = Br(Lsin(\phi) - Dcos(\phi))dr \tag{60}$$

Where B is the number of blades. For the solution process of the theory, ϕ, C_n and C_t are all dependent on the angular and axial induction factor. Hence, to reach

a solution, an iteration procedure is required. First, one would guess the starting values of a and a', then one would calculate α, C_l and C_d. With these calculated, one updates a and a' and check for convergence of the results within a specified tolerance.

3.8.4 BEM Corrections

Several assumptions are imposed in the BEM theory. In order to describe the aerodynamics in an adequate manner, some corrections have to be imposed.

Prandtl Correction

The airflow around the surface of a foil tends to follow the pressure gradient, and hence flow around the blade from the lower to the upper side. The result of this comes in the form of reduced production of aerodynamic force compared to the optimal conditions. This is corrected by the Prandtl correction factor.

Glauert Correction

Based on Equation 43, one may notice that if the axial induction factors $a > 0.5$, then the velocity in the wake would appear negative. This is the reason of why the BEM theory is not applicable for such values of the axial induction factor. To account for this, the Glauert correction is used for induction factors $a > 0.4$.

Dynamic Inflow/Wake

For the current BEM-theory, the induction factors are immediately updated if a change in incoming wind, blade pitch angle or rotor speed occurs. In a realistic scenario, with increasing rotor diameters, reacting to these changes becomes more complicated and time-consuming. The "dynamic wake effect" is a time lag in induced velocities due to shedding and downstream convection of vorticity.

Dynamic Stall

Dynamic stall is described as a sudden attachment and re-attachment of the flow around the surface of the foil. For these instances, the lift and drag coefficients may not be described by their static values. The consequences of this may be severe, and lead to large transient loads.

4 Offshore Substructure Concepts

4.1 Overview of the floating wind turbine concepts

To this date, several floating foundation classes have been researched and implemented. Each of these have their own benefits and drawbacks. The main categories of floater concepts may be observed in Figure 4.1. Many of these may share similarities with designs in the oil and gas industry. This is to be expected considering the FOWTs are mostly developed by similar companies as those of the oil and gas industry.

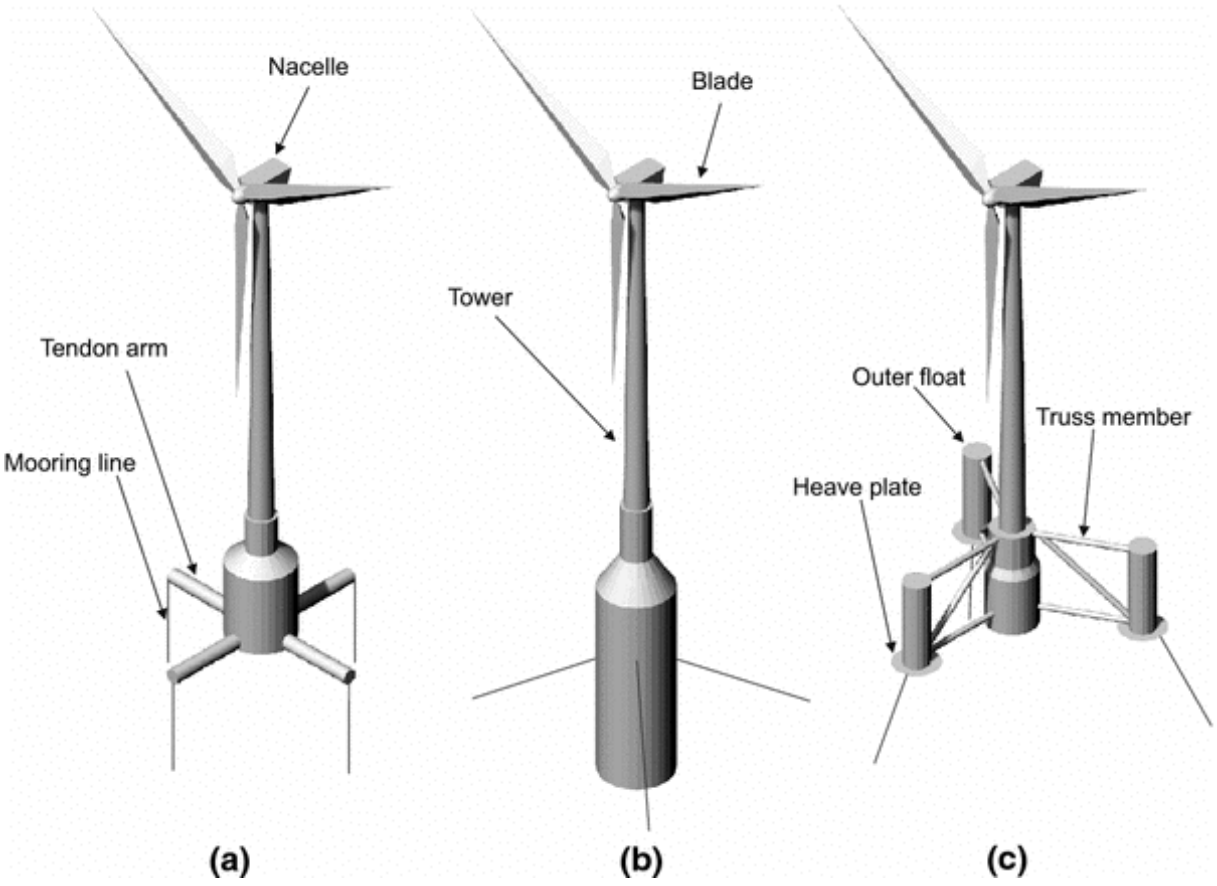

Figure 4.1: The three classes of offshore FWT support platforms from the left, TLP. spar-buoy, semi-submersible (Karimi et al., 2017)

4.1.1 Semi-Submersible

Semi-submersible floating wind farms, also known as column stabilized foundations, are typically composed of columns and pontoons. The columns provide stability by restoring moments, while the pontoons provide buoyancy (Du, 2021). By using surface-piercing columns instead of a solid flat deck, wave forces are reduced. However, the water-plane area of a semi-submersible is still larger than that of a spar design, which can lead to increased loads on the columns and potentially reduced stability (Anaya-Lara et al., 2018).

One of the main advantages of semi-submersibles is their flexibility in terms of water depth, which makes them well-suited for use in deeper waters. In addition, they often have lower mooring costs due to the use of catenary mooring, and the fact that the transportation and installation is typically simpler than other floating wind farm designs.

4.1.2 Tension Legged Platform

Tension legged foundations (TLPs) are a type of offshore wind farm foundation that is kept in place by vertical tendons anchored to the seabed (Bachynski et al., 2012). The stability of a TLP comes from the tension in these tendons, which allows the structure to move horizontally like a soft spring, while stiffening in the vertical direction. This results in smaller motions, smaller footprint on the seabed, and less steel weight.

However, the main disadvantage of TLPs is the difficulty of installation. This process can be time-consuming and challenging, particularly due to the need to work within a limited weather window. As a result, simpler installation methods are generally preferred.

4.1.3 Spar-Buoy

The spar-buoy is a foundation that consists of a large, vertical buoyant cylinder. The cylinder has a deep draft, which is ballasted at the bottom, and is kept in place by catenary mooring lines. The deep draft and small water plane area of the spar-buoy provide stability, allowing it to move slowly and smoothly (Bachynski-Polic, 2022a).

One advantage of the spar-buoy design is its simplicity, which makes it easy to manufacture. However, the tall hull structure of the spar-buoy can make it difficult to install, especially since this often requires the structure to be turned upright at deep waters. This can expose the installation process to more challenging environments, which is considered the main disadvantage of the spar-buoy design (Anaya-Lara et al., 2018).

4.2 INO-WINDMOOR

The WINDMOOR project is a research effort funded by the Research Council of Norway and industry partners Equinor, MacGregor, Inocean, APL Norway, and RWE Renewables. The project has a main goal of understanding the loads that affect the mooring system design of FOWTs. The WINDMOOR semi-submersible, designed by Inocean and Equinor, is displayed in Figure 4.2 and consists of three vertical columns connected by deck beams and pontoons. The design specifications can be found in the design report from SINTEF (Souza et al., 2021).

Figure 4.2: INO WINDMOOR design (Souza et al., 2021)

Displacement [t]	141176.1
Draft [m]	15.5
CG_X^***[m]**	[-0.37, 0.37]
CG_Y^***[m]**	[-0.37, 0.37]
CG_Z^***[m]**	4.23
R_{XX} **[m]**	43.67
R_{YY} **[m]**	44.18
R_{ZZ} **[m]**	30.26
Static heel angle at rated thrust [deg]	6.4
Still water air-gap to column top [m]	15.5
Still water air-gap to deck beam bottom [m]	12

Table 4.1: Full FWT main properties (including ballast). The radii of gyration refer to the FOWT CoG, assuming the turbine's own CoG at the tower center. $^*CG_x$ and CG_y are dependent on the nacelle orientation. (Souza et al., 2021)

Column diameter [m]	15
Column height [m]	31
Pontoon width [m]	10
Pontoon height [m]	4
Center-center distance [m]	31
Deck beam width [m]	3.5
Deck beam height [m]	3.5
Total substructure mass [t]	11974
Total substructure CG_X[m]	-5.91
Total substructure CG_Z[m]	-9.7
Total substructure R_{XX} [m]	23.66
Total substructure R_{YY} [m]	18.63
Total substructure R_{ZZ} [m]	28.10

Table 4.2: Geometrical parameters of WINDMOOR floater (including ballast)(Souza et al., 2021)

DOF	Surge	Sway	Heave	Roll	Pitch	Yaw
Natural period [s]	97.3	98	16.3	29.5	31.4	88

Table 4.3: Reference values for natural periods (Souza et al., 2021)

4.3 INO-WINDMOOR Wind Turbine

For this thesis, the INO WINDMOOR is used as the substructure of the system. In addition to this, the WINDMOOR 12MW turbine is mounted on top of the floater. This turbine is an up-scaled version of the International Energy Agency (IEA) 10 MW turbine, utilizing the same design. The properties of the turbine and the tower are given in Tables 4.4-4.5.

Rated electrical power [MW]	12.0
Specific power $[W/m^2]$	324.8
Rotor orientation	Upwind
Number of blades	3
Rotor diameter [m]	216.9
Hub diameter [m]	5.0
Blade length [m]	105.4
Blade prebend [m]	6.8
Rotor precone [deg]	6.0
Hub height [m]	131.7
Cut-in/rated/cut-out wind speed [m/s]	4.0/10.6/25
Generator efficiency [%]	94.4
Cut-in/rated rotor speed [rpm]	5.5/7.8
Blade mass [kg]	3*63,024
Hub mass [kg]	60,000
Nacelle mass [kg]	600,000

Table 4.4: WINDMOOR 12MW wind turbine properties (Souza et al., 2021)

Diameter at top [m]	5.97
Diameter at bottom [m]	9.90
Thickness at top [mm]	30.1
Thickness at bottom [mm]	90.0
Length [m]	110.20
Mass [t]	1161.6
CG_z **from base [m]**	56.65

Table 4.5: WINDMOOR 12MW wind turbine tower properties (Souza et al., 2021)

5 Environmental Conditions

5.1 Choice of Site

There are several factors to consider when choosing a site for offshore wind development. Some of the most important factors include the opportunities for transportation, the water depth, the distance to shore, and the quality of the wind. A key quantity to consider when evaluating potential sites is the wind power density P_0. It is expressed as

$$\frac{P_0}{A} = \frac{\rho u^3}{2} \tag{61}$$

Where A is the area of the wind turbine rotor, ρ is the density of air, and u is the wind speed. The wind power density is a way of quantifying the wind resources disregarding the area of the turbine rotor. The downside of utilizing these measurements is the fact that it doesn't separate normal wind conditions and extreme conditions. Hence, hurricanes and storms are included in the measurements (Bachynski-Polic, 2022a).

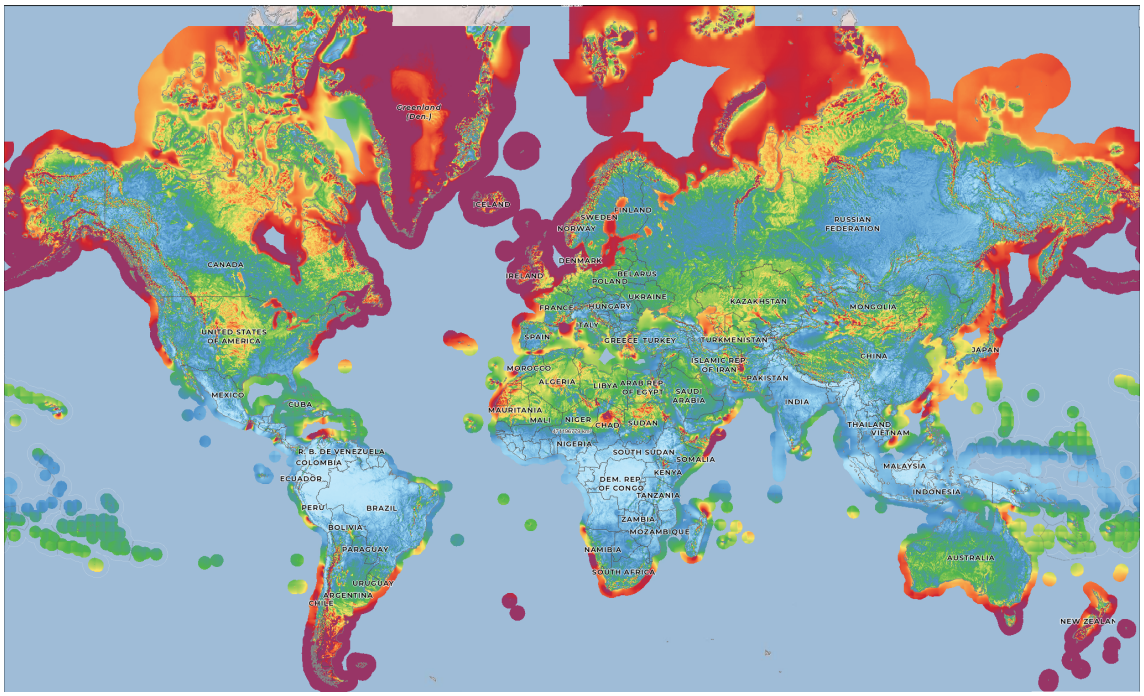

Figure 5.1: Map illustrating the global variation in wind power density. It ranges from highest to lowest as purple, red, orange, yellow, green, blue. (Global Wind Atlas (2022))

As seen in figure 5.1, the mean power density has large values in Northern Europe. There are other locations suitable for extracting wind energy such as New Zealand, the southern parts of South-America, but also Japan.

Norway is a significant contributor to the global shift towards renewable energy, but has not yet developed large offshore wind farms due to the challenging conditions in its deep waters. This may be observed in Figure 5.2. However, the Norwegian

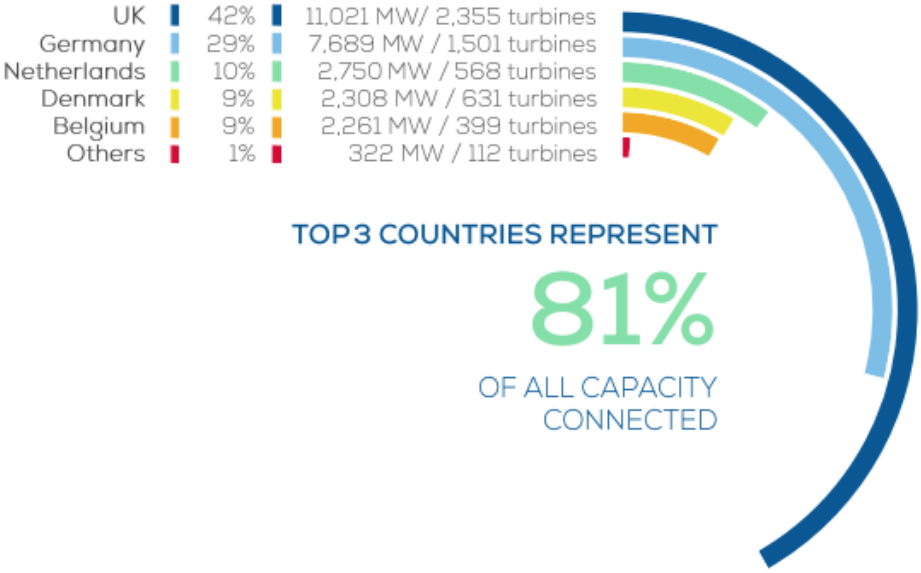

Figure 5.2: Europe's installed capacity (WindEurope, 2021)

government has set a goal of 30GW of offshore wind capacity by 2040, indicating a focus on further advancement on this technology (Vatnøy, 2022). One company leading the way in this area of research is Equinor, which has designed a flexible floating wind concept for use in the Hywind Tampen area, approximately 140km off the coast of Norway. This area has water depths of around 280 meters, making it suitable for FWTs (Equinor, 2022). By focusing on the costs and benefits of offshore wind development in these challenging conditions, Norway and companies like Equinor can continue to play a key role in the global transition to renewable energy. The Hywind Tampen area has been chosen as the site for this thesis due to it's significance in the transition, but also the challenges concerning deep waters.

5.2 Establishment of Project Environmental Data

The environmental parameters at the specific location, Hywind Tampen, were to be determined by 1-hour data of wind, wind sea and swell over a period of 36 years. For wind modeling, DNV-C205 (2019) specifies that for design, site specific wind data should preferably cover a 10-year period or more with a sufficient resolution. Sufficient resolution in this manner, refers to an averaging period between 1-60 minutes. In many long-term probability calculations in the past, NORA10 data have been used. This is a database of 3-hour measurements. For this master thesis, data was gathered for the use in creating an environmental distribution. After some further investigation, it was established that generating a whole environmental distribution based on measurement data was a large task that would take a lot of time. Due to this, other means were used to gather the environmental descriptions required for the time-domain analyses. The selected source for the distribution of environmental data was chosen to be the work by Li et al. (2013), in which joint environmental data at several European offshore sites have been documented. These offshore sites are displayed in Figure 5.3, in which for the present analysis, site 14

was chosen due being close to the selected site location.

Figure 5.3: Illustration of the locations of the offshore sites used for establishments of distributions (Li et al., 2013)

The environmental data applied by this study are of a numerical hindcast model from National and Kapodistrian University of Athens (Li et al., 2013). Since the study develops combined wind and wave energy concepts, larger databases are required for comparisons of site conditions, and hence, numerical hindcast data are more appropriate than observational records. The hindcast data applied for the prediction of long-term environmental conditions have been sampled and archived hourly for both wind and waves in a database from 2001 to 2010. From these samples, the marginal and joint distributions were acquired by fitting analytical distributions to the raw data of the mean wind speed U_W, the significant wave height H_S and the wave spectral peak period T_P as shown in the next Section.

5.3 Joint distribution

This Section presents the general establishment of the environmental distribution provided by Li et al. (2013).

Waves

By the consideration of only wave data, a joint probability density function (PDF) of H_S and T_P was established. This distribution consists of a marginal distribution of H_S and a conditional distribution for T_P given H_S as follows:

$$f_{Hs,Tp}(h,t) = f_{Hs}(h) \cdot f_{Tp|Hs}(t|h) \tag{62}$$

For the marginal distribution of H_S, the main part of the raw data followed a log-normal distribution, while the tail of the data followed a Weibull distribution. Based on this, the hybrid log-normal and Weibull distribution called the Lonowe model was decided to be the best fit. From this, the probability density function is expressed as:

$$f_{Hs}(h) = \begin{cases} \frac{1}{\sqrt{2\pi}\sigma_{LHM}h} exp\left(-\frac{1}{2}\left(\frac{ln(h-\mu_{LHM}}{\sigma_{LHM}}\right)^2\right) & \text{if } h_0 \geq h \\ \\ \frac{\alpha_{HM}}{\beta_{HM}}\left(\frac{h}{\beta_{HM}}\right)^{\alpha_{HM}-1} exp\left[-\left(\frac{h}{\beta_{HM}}\right)^{\alpha_{HM}}\right] & \text{if } h_0 < h \end{cases} \tag{63}$$

Here, h_0 defines where the distribution of H_S shifts from following the log-normal distribution to the Weibull. μ_{LHM} and σ_{LHM} are the corresponding parameters of the log-normal distribution, while β_{HM} and α_{HM} are the shape and scale parameters of the Weibull distribution.

Wind

The raw data of the mean wind speed at reference height 10m are suggested to follow a two-parameter Weibull distribution by Li et al. (2013). The PDF is expressed as:

$$f_{Uw}(u) = \frac{\alpha_U}{\beta_U}\left(\frac{u}{\beta_U}\right)^{\alpha_U-1} exp\left[-\left(\frac{u}{\beta_U}\right)^{\alpha_U}\right] \tag{64}$$

Here, α_U and β_U are the shape and scale parameter for the wind respectively. This revolves around a preliminary study of the variation of wind speed at different levels, in which indicates a power law profile with exponent $\alpha = 0.1$ being applicable to several of the sites. The power law profile takes the form:

$$U(z) = U_{10}\left(\frac{z}{10}\right)^{\alpha} \tag{65}$$

Where U_{10} is the mean wind speed at reference height 10m and z is the height.

Joint distribution

The two-parameter Weibull distribution is utilized to define the conditional probability density function (PDF) of significant wave height with respect to the mean

wind speed as:

$$f_{Hs|Uw}(h|u) = \frac{\alpha_{HC}}{\beta_{HC}}\left(\frac{h}{\beta_{HC}}\right)^{\alpha_{HC}-1} exp\left[-\left(\frac{h}{\beta_{HC}}\right)^{\alpha_{HC}}\right] \tag{66}$$

Here, α_{HC} is the shape parameter and β_{HC} is the scale parameter of the distribution. The last component consists of a conditional distribution of the spectral peak period with respect to given mean wind speed and significant wave height. This PDF is formulated as:

$$f_{Tp|Uw,Hs}(t|u,h) = \frac{1}{\sqrt{2\pi}\sigma_{ln(T_p)}t} exp\left(-\frac{1}{2}\left(\frac{ln(t)-\mu_{ln(T_p)}}{\sigma_{ln(T_p)}}\right)^2\right) \tag{67}$$

in which $\mu_{ln(T_p)}$ is the mean value of the conditional log-normal distribution and $\sigma_{ln(T_p)}$ is the standard deviation of this distribution. With these components, Li et al. (2013) have established a joint distribution of U_W, H_S and T_P which is given as:

$$f_{Uw,Hs,Tp}(u,h,t) = f_{Uw}(u) \cdot f_{Hs|Uw}(h|u) \cdot f_{Tp|Uw,Hs}(t|u,h) \tag{68}$$

Due to time-management, validating the extracted raw environmental data against the distribution wasn't done. Despite this, for the time-domain simulations, proper environmental variable combinations for the selected location were of interest. For this, Figures established by Li et al. (2013) were used. This described the variations of parameters and their correlation for site 14. This figure may be found in their report as Figure 8 (Li et al., 2013). In addition to this, a more extreme case was of interest for the coming simulations, and hence, the reference 50 year values presented by Li et al. (2013) were used. These are shown in Table 5.1 as load case number 3.

5.3.1 Current

For the establishment of corresponding current conditions in relation to the joint environmental distribution, it was decided to follow DNV-RP-C205 for the calculation of wind generated current velocity (DNV-RP-C205, 2010). For deep waters, when no statistical data are available, an equation for the current velocity may be expressed as:

$$U_{C,Wind}(0) = kU_{1,Hour,10m} \tag{69}$$

Here, k is a factor ranging between 0.015-0.03. Here, a factor of 0.03 is chosen as it's of interest to investigate the more extreme cases.

5.4 Design Load Cases

For the design load cases, considering the fact that the existing rules for FOWTs coming up short in terms of e.g. damage stability, it was seen as more interesting to look closer into some of the more extreme environmental load cases in order to highlight the differences. The damage cases chosen are presented in Table 5.1, in an ordered manner. The first and second load case were chosen to be similar due to wanting to investigate the effect of increasing hydrodynamic loads due to an increase

in significant wave height. The third load case is of a 50-year return period, and is seen as an extreme load case in which the turbine is parked. The last load case targeted the investigation of emergency shutdowns.

Load case nr.	U_w**[m/s]**	U_C**[m/s]**	H_S **[m]**	T_P **[s]**	**State**	**Operation**
1	18.5	0.555	5.25	11.2	Operational	PP
2	18.5	0.555	7.25	13	Operational	PP
3	33.49	1	10.96	11.06	Extreme	P
4	18.5	0.555	7.25	13	Operational	Shutdown

Table 5.1: Environmental load cases, P - Parked, PP - Power Production

6 Methodology

6.1 Software

In order to conduct a coupled analysis of a damaged FOWT, several steps must be taken. First, a panel model with a compartment model must be developed for the radiation-diffraction analysis. Then, the time-domain coupled analysis can be performed using a software such as SIMA, which requires a complete model of the FOWT system including the mooring, turbine, and blades. Additionally, wind data must be generated for the analysis. One potential extension of this work could involve creating a time-domain script to calculate water ingress forces on the FOWT.

6.1.1 GeniE

GeniE is a software package developed by SESAM for modeling high-level geometry, such as beams, stiffened plates, and shells. It can also include load transfer, explicit loads, and wind loads ('GeniE User manual V7.3', 2016). As such, it can be used both as a conceptual modeler and code checker for beams and panels. Here, GeniE will be used to create the finite element panel models and compartment model for further analysis.

6.1.2 HydroD

HydroD is another component of the SESAM software suite. It is a tool for performing hydrostatic and stability analysis, as well as hydrodynamic wave load and motion response analysis ('HydroD User manual V4.9', 2016). The input for these analyses includes a panel model, compartment model, and free-surface model (DNV, 2022b). The panel model is used specifically for the frequency-domain solution of the hydrodynamic analysis in HydroD, while the compartment model is used to define damage cases for the floater. Lastly, the free-surface model is used for full second-order difference frequency effects analysis.

6.1.3 SIMA

The SIMA workbench is a complete tool for modeling, simulation and results presentation of marine operations (DNV, 2022b). The analyses performed in SIMA are performed in the time-domain, which allows the visualization of the transient response of a system. This can be useful for identifying specific points in time where coupling effects occur. It also allows the inclusion of the aerodynamics of the turbine and the control system of its operation. The workbench includes several calculation software such as SIMO and RIFLEX. SIMO provides the possibility of simulating motions and station-keeping of floating vessels and the hydrodynamic forces affecting the system. RIFLEX is a software for analysis of flexible slender structure systems such as mooring lines, risers and wind turbine blades. When applying RIFLEX for the

simulation of aerodynamic forces, one is required to define the airfoils, and applying BEM theory.

6.2 Finite Element Panel Model

In order to perform frequency domain hydrodynamic analyses, T*.FEM panel models are required. These are constructed in the software GeniE. When these are established, the panel method is applicable for the analyses.

6.2.1 Floater Panel Model

As preliminary work for the thesis, a panel model of the INO-WINDMOOR 12MW semi submersible was created and verified. The dimensions of the panel model were extracted from the official SINTEF report presented in Tables 4.1-4.2 in Section 4.2. The panel model represents the submerged wetted surface of the floater by the means of shell elements. The geometry of the wetted surface is displayed in Figure 6.1. As shown, the model applies XZ-symmetry, which in return reduces the computational effort of the analyses.

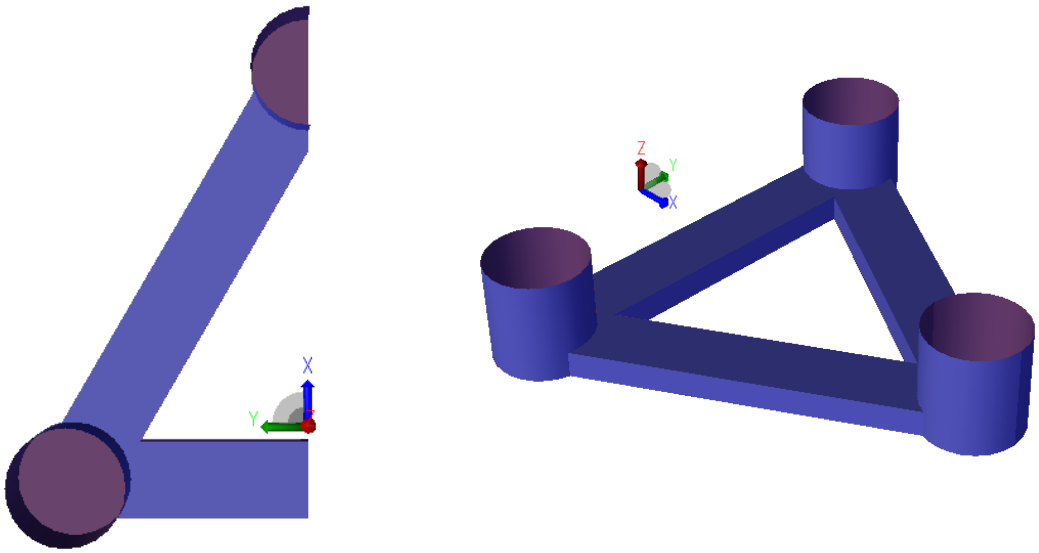

(a) Model of the geometry top view (b) Model of the geometry mirrored

Figure 6.1: Modeled geometry in GeniE

For the modeled geometry, a mesh sensitivity study was performed for a series of mesh densities. The results of this study concluded that a mesh density of $\Delta x = 0.75$m proved sufficient in representing the hydrodynamic properties of the structure. The final mesh is displayed in Figure 6.2.

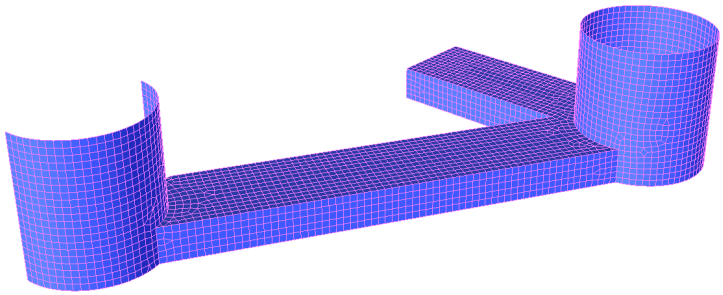

Figure 6.2: Panel model mesh $\Delta x = 0.75$m

6.2.2 Compartment Model

A compartment model is an addition to the SESAM package, in which one is able to model the internal closed off compartments of a structure or compartments that are damaged. The benefit of applying such a model in an analysis is the possibility of analyzing the ballast mass within internal compartments of a structure. In addition to this, one may define damage cases for the compartments, in which one may investigate the damage stability of a structure in-depth. These damage cases would as a result update the loading condition of the structure, but also include the effects of damage/internal ballast in the calculations of hydrodynamic coefficients.

For the preliminary work of the thesis, two compartment models for the WINDMOOR substructure were created. With these, investigations on the effect of including ballast water in analyses were investigated. In detail, these effects regarded the inclusion of internal dynamic effects of the ballast mass, and the effect of using partially filled tanks. The results provided insight into the dynamic behavior of the internal fluid, but also the importance of detailed information regarding the distribution of the internal ballast mass. The SINTEF report does not specify the amount of internal ballast water (Souza et al., 2021). The inputs for HydroD specifying the COG and the radii of gyration excluding the contributions from the ballast water proved time-consuming to establish. The conclusion from this was to not including internal tanks for the ballast water, but instead only for the exposed areas of the columns. For this thesis, the compartment model was included to account for the exposed area close to the waterline in which damage could occur. This compartment model is displayed in Figure 6.3.

Compared to the wetted surface panel model, a significant difference comes in the form of not being able to apply symmetry for the model. On the other hand, this also makes it possible to establish analyses with un-symmetrical filling ratios which is of interest. The compartment model was designed based on the suggested extent of damage by DNV as shown in Figure 3.1. Hence, it's designed to cover 3m below the water surface, 5m above, and a penetration extent of 2.5m. For the initial configuration, the compartments are split at 4m vertical distance, and hence,

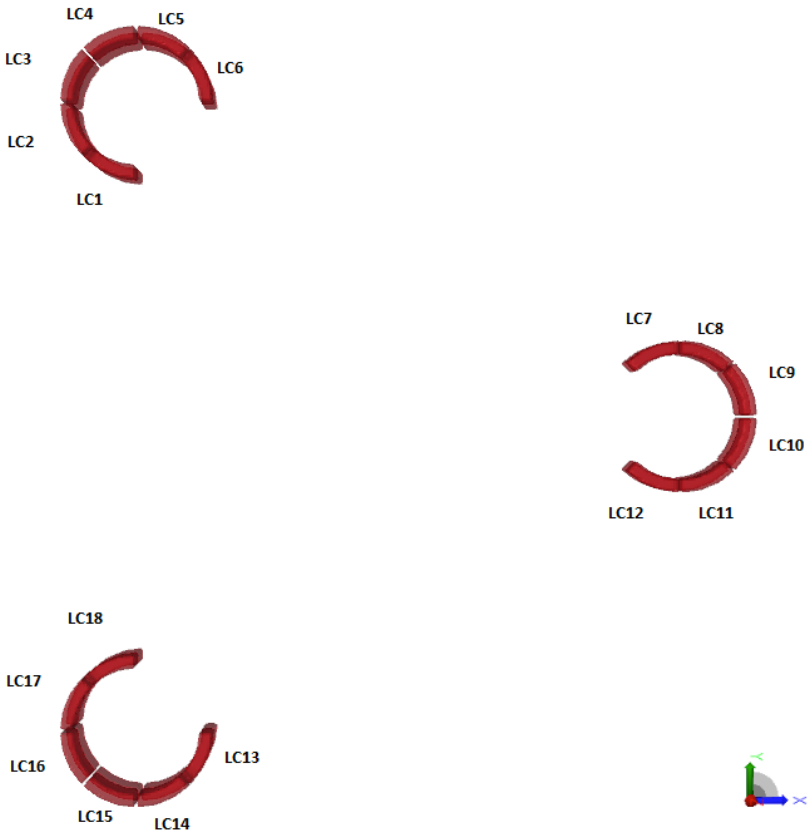

Figure 6.3: Column compartment model, load case 1-18

the number of compartments is doubled. Each compartment consists of a volume of approximately $49m^3$. The compartments with their numbering may be seen in Figure 6.3 displaying the upper compartments, but the numbering refers to the lower ones.

6.2.3 Free-Surface Panel Model

Based on the literature review conducted prior to the thesis, the second-order effects were highlighted as significant for moored structures. The SESAM package offers the possibilities to quantifying these effects. This requires a second-order frequency domain analysis. To perform such an analysis in HydroD, one is required to quantify the free-surface by the means of a finite element panel model. This may be done by the means of the software HydroMesh or GeniE in the SESAM package. For this thesis, GeniE was used due to the prior engagement in the software for the other models. The model of the free surface is established in a similar manner, in which one models the geometry of the surface excluding any surface piercing components of the body. Then a hydro-pressure load is defined in the Z-direction with a normal component pointing downwards. The panel model following the procedure is displayed in Figure 6.4.

The free surface panel model applies the same XZ-symmetry as the wetted surface. In order to converge towards the correct results, an appropriate selection of the outer

boundary radius has to be selected. This selection takes into account the decaying local waves, and the wavelength of the environmental conditions. The Wadam user manual specifies that the radius of the outer boarder should exceed 50% of the water depth. The radius of the outer boarder was decided 250m, and this was due to wanting to investigate the effects of extreme conditions in addition to those of the normal.

Furthermore, there were several constrictions to account for. Similar to the wetted surface panel model, a constriction regarding the maximum amount of panels for the free surface is 10000 panels. In addition to this, the mesh is to consist of only four-node panels. The process of eliminating the remaining triangular panels in the mesh proved time-consuming, but was achieved. The surface was divided into 4 sections, in which each correspond to their own mesh density. This allowed finer mesh closer to the body surface, and hence, more accurate results. The mesh densities were decided based on approaching the maximum number of panels as it didn't affect the computational effort by a large amount. The final densities for the different zones are concluded in Table 6.1. Here, zone 1 appears as enclosing surfaces 2m around the columns, while the other zones cover the whole surface with a radius defined from the center of the plane.

Zone nr.	**Inner-Outer radius [m]**	**Mesh density [m]**
1	2	1
2	0-50	1.5
3	50-100	3
4	100-250	4.5

Table 6.1: Free Surface zone properties

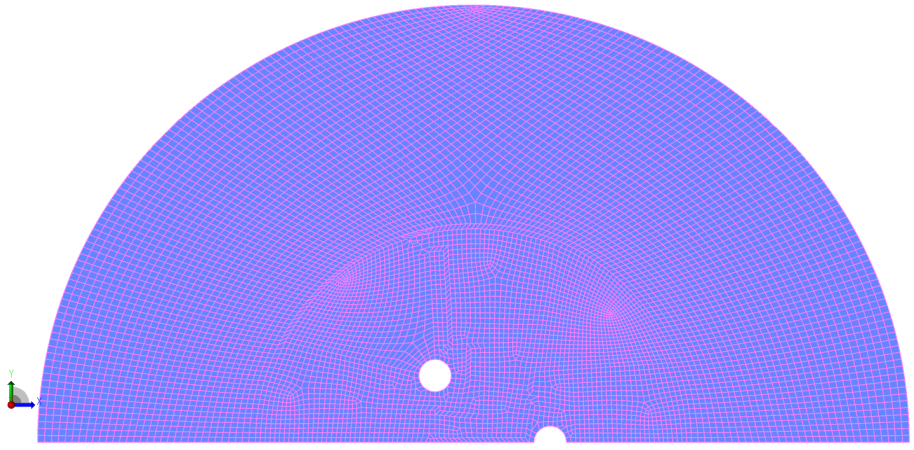

Figure 6.4: Free surface FE panel model mesh

Despite being sufficient for the intact condition, when defining unsymmetrical damage cases for the substructure modeled in HydroD, the loading condition of the structure is updated automatically in order for it to reach equilibrium. In several cases this simplifies the calculation and setup procedures. When the platform reaches a new equilibrium it is no longer symmetric in any plane because of the inclination, hence, the free-surface is not aligned so that one may use the symmetric

version. When the angle of heel is different from the angle of trim, this produces a different radius of the free surface in the x- and y-direction with respect to the global system. In terms of second order analyses, the result of this is an analysis incapable of running. To make up for this issue, a panel model of the free-surface corresponding to the same zones as in Section 6.2.3 had to be created. The difference between these being that the new one contains no symmetry. The panel model of the outer surface of the body also had to be updated so that it could account for a level of submersion of the substructure. Despite changing the models, the properties stated in regards to mesh densities and zones remained close to identical. The updated free-surface model is displayed in Figure 6.5.

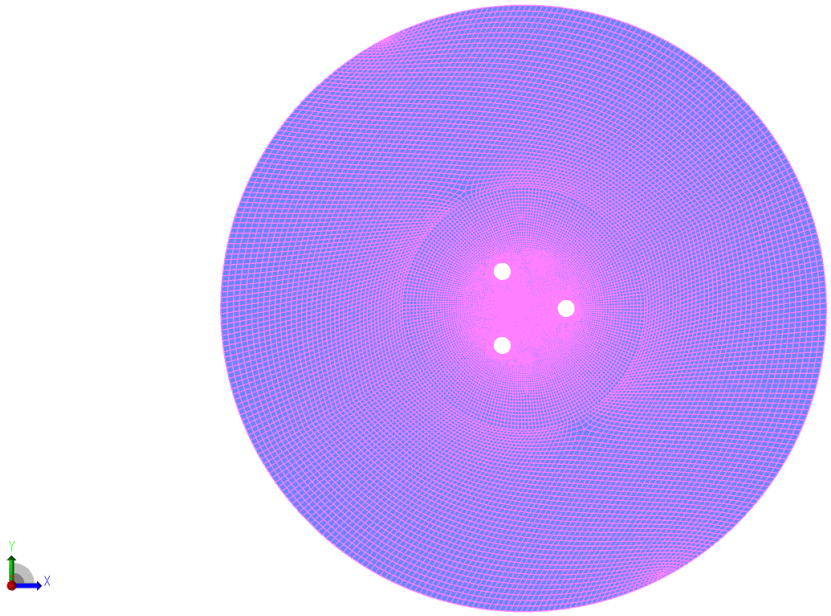

Figure 6.5: Free surface FE panel model mesh with no symmetry

6.2.4 Mesh Quality

For the preliminary work of the thesis, a convergence study of the body panel model was performed in order to find a panel size sufficient in describing the hydrodynamic parameters of the substructure. This was performed in order to minimize the computational cost of the analyses while still providing accurate results. The study performed in the project thesis involved the added mass coefficients, the damping coefficients, the response transfer functions and the wave excitation transfer functions. The results concluded that the hydrodynamic coefficients did converge, and that at a mesh panel size of approximately $\Delta x = 0.75m$ was sufficient. As an addition to this previous study, the drift forces are calculated for the mesh configuration by the two methods direct pressure integration and conservation of momentum which is presented in Section 7. The total number of elements for the models utilized for the intact and damaged conditions are summarized in Table 6.2.

Model	Number of elements	Number of elements on free surface	Mesh density [m]
Intact	5913	8919	0.75
Damaged	11621	16204	0.75

Table 6.2: Panel model properties

6.3 Damage Cases

In order to establish the hydrodynamic data for the damaged substructure in HydroD, damage cases specifying the extent of damage has to be established by the means of the compartments. The compartment model has been established by the means of satisfying the exposed portions of the columns as shown in Figure 3.1. The thesis considers the collision with a low-speed service vessel as these are the vessels traveling the closest to the FOWTs.

6.3.1 Damage Load Cases

The damage cases to be investigated in the thesis are established in order to look closer at several scenarios, including minimal and critical damage cases. Taking into account the alignment of the compartments, it is assumed possible to penetrate up to four compartments in one accidental scenario. Considering the volume of the compartments, it would then be possible to have about $127.2m^3$ of damaged space. For the damage cases, the initial transient phase of the flooding has been ignored, and the focus is on the behavior after the damage has taken place. This means that for the analyses, the focus is on 100% filled compartments of different configurations. The damage cases established are also made to investigate the effect of the damage location. When updating the damage of the compartment model in HydroD, the model is automatically balanced in order to reach a new equilibrium condition. This comes in the form of the waterline, trim- and heel angle. For the damage cases specified in Table 6.3, these parameter changes are specified. Originally, the damage cases were meant to include damage of the upper compartments as well. Despite this, considering the simplification of neglecting the transient phase, the angle of heel and trim together with the change in waterline was not large enough to reach the upper compartments. Hence, these were neglected for the frequency-domain analyses.

In addition to the investigation of the hydrodynamic parameters changed due to the damage cases, an investigation is performed in order to investigate the significance of the hydrodynamic parameters dependency on the angle of heel and trim. This is due to the application of symmetry in the panel model of the floater and the free surface. In principle, the application of symmetry reduces the computational cost of the process. This is why it would be valuable to investigate whether these angle of inclinations are significant to the results. This investigation is to be performed for the first load case defined, and may be looked closer at in Sections 8.2 and 8.5.

Load case nr.	Damaged compartments	Total mass [kg]	Waterline Z [m]	Trim angle [deg]	Heel angle [deg]
1	9, 10	100.6E+03	0.1845	1.5153	0.0046
2	8, 9, 10, 11	201.2E+03	0.4711	3.9512	0.0021
3	14, 15	100.6E+03	0.1845	-0.8306	1.4552
4	13, 14, 15, 16	201.2E+03	0.4711	-1.5375	2.7756

Table 6.3: Damage case definitions

6.4 Frequency-Domain Analysis

Frequency domain analysis is a mathematical approach which is used to study wave body interaction within the field of hydrodynamics. The approach involves analysis of the response of a structure in regards to a range of wave frequencies and directions. By utilizing the FE panel models of the geometry and the free surface within HydroD, Wadam may be used in order to calculate the wave loads and motion response. The analyses may then be used to provide insight into the behavior of the structure in regards to several sea conditions. This allows for the possibility of evaluating the design in order to maximize the safety and efficiency prior to construction. The results in regards to the first and second order frequency domain analysis consists of the following data:

- Mass matrix and hydrostatic stiffness (including compartments)
- Frequency dependent added mass, damping, with respective retardation functions
- First order excitation transfer functions
- First order response transfer functions
- Horizontal mean drift forces
- Quadratic transfer functions

6.4.1 First Order Analysis

The first order frequency domain analysis are performed for the direct wave heading of 0° and 90° with wave periods 5-35s with a step of 1s. The parameter inputs of the total mass, COG, etc. correspond to the quantities defined by Souza et al. (2021) as shown in Table 4.2. As specified in the project thesis, additional critical damping of 5% was included in heave, roll and pitch in order to obtain reasonable motion transfer functions. For the analyses, additional restoring matrices were also included in the horizontal DOFs to represent the mooring system. These additions were included in compliance with Souza et al. (2021). For the preliminary work of the thesis, hydrodynamic coefficients from the first-order analyses of the structure was verified up against the official results provided by the reference article. This comparison is included in Section 7.

6.4.2 Second Order Analysis

Based on the conducted literature study, the significance of the second-order effects on moored structures are of important consideration. The two possible ways of performing this analysis is by pressure integration on the body, and Newman's approximation. The difference between these two comes in the calculation procedures. The Newman's approximation utilizes the mean drift forces, and neglects the second order velocity potentials. Since the pressure integration takes into account this second order contribution, it is more computationally expensive, but produces more accurate results. For this study, the pressure integration approach was selected.

In regards to the analysis, the goal is the investigation of the difference-frequency effects. These are the effects resulting from the structures interaction with the combination of two wave frequencies. Considering the second-order analysis being more time-consuming than the first-order, the span of wave frequencies analyzed had to be reduced. The analysis considers all combinations of the frequencies, and hence, including the same number of frequencies as for the first-order analysis would take a very long time to perform. This is also the reason of why only the wave heading of 0° was used. The frequency range to be solved for was defined between $\omega = 0.5 - 1.4 rad/s$ with an interval of $\Delta\omega = 0.025$ based on the radius of the modeled free-surface. This choice was based on a number of analyses performed at different ranges, and their computational cost. The reasoning behind keeping the computational costs low resides in the task of performing these analyses for a set of damaged conditions in addition to the intact one. Considering the non-symmetric models, this is already a computationally demanding task.

For the calculation methods applied for the analyses, the direct pressure integration method was utilized due to it being capable of calculating all degrees of freedom in one analysis. As mentioned previously, the method relies more on the quality of the mesh, which was accounted for in the previous processes.

Considering the issue mentioned in Section 6.2.3 regarding the symmetry of the models for the damaged conditions, an effort was made to investigate whether one could ignore these rotations and still achieve accurate results for the hydrodynamic coefficients and transfer functions. If this is a possibility, the computational efficiency would increase considering the applicability of symmetric models.

After the frequency-domain simulations, the results are to be formatted and transferred into the SIMA workspace to be used in further time-domain simulations.

6.5 SIMA Coupled Model

The behavior of the FOWT is to be analyzed by the means of several fully coupled time domain simulations within the SIMA workbench. The output results files from the frequency-domain analyses performed in Wadam were converted and imported into SIMA as a SIMO body by the means of a SESAM interface file. The mooring system was defined within the environment by the means of mooring segments. In addition to this, the tower model and the turbine were imported into the system. These models were provided by Erin Bachynski from The Department of Marine Technology. The properties of these models are described in Section 4.3. These components were connected by the use of the master-slave technique within the SIMA environment, in which the tower base and the mooring fair-leads were defined as slaves with respect to the floating body. Figure 6.6 presents the visual view of the SIMA model of the intact FOWT.

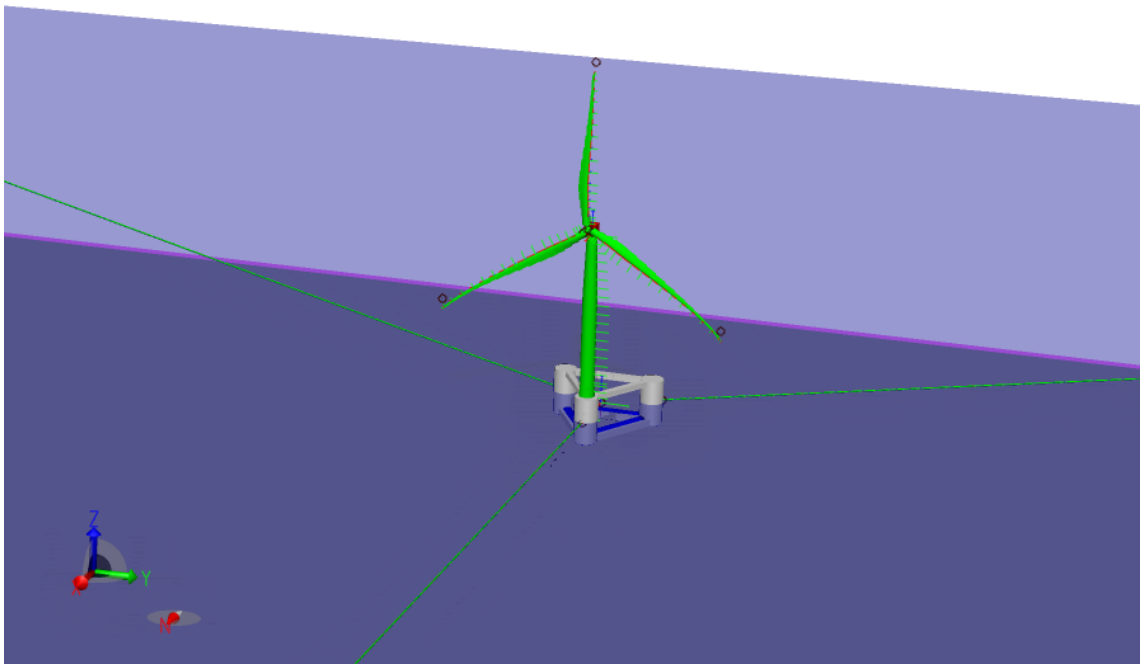

Figure 6.6: SIMA coupled coupled numerical model

6.5.1 Corrections to Hydrostatic Restoring Data

The hydrodynamic results imported from the frequency domain analysis performed within HydroD takes into account the complete FOWT mass properties. The SIMO body imported is to account for the data of the floating body only. Due to this, corrections to the parameters had to be performed within SIMA in regards to the hydrostatic data of the floater. These new restoring coefficients may be determined by the means of Equation 70.

$$C_{ii} = \rho g I_{wp} + \rho g \nabla z_B - M g z_G \tag{70}$$

Here, ρ represents the water density, g the gravitational constant, I_{wp} the moment of inertia of the water plane, ∇ the displaced volume of water, M the mass of the floater, z_B is the z-coordinate of the center of buoyancy, and z_G is the z-coordinate of the center of gravity. There are several options regarding the hydrostatic data within SIMA. One of these is the option of including gravity. This represents the last term of Equation 70. The buoyancy on the other hand is included by defining a specific vertical force of corresponding magnitude which attacks at the center of buoyancy in the positive z-direction. As a result of this, the remaining hydrostatic restoring matrix accounts for only the contribution based on volume variations around the equilibrium. These contributions may be calculated by Equation 71 (Faltinsen, 1999).

$$\begin{aligned} C_{33} &= \rho g A_{wp} \\ C_{44} &= \rho g \int\int_{A_{wp}} y^2 ds \\ C_{55} &= \rho g \int\int_{A_{wp}} x^2 ds \end{aligned} \tag{71}$$

6.5.2 Wind File Generation

In order to capture realistic wind conditions within the SIMA environment, wind input files for the time-domain simulations are generated by the software TurbSim which is developed by NREL. TurbSim is a stochastic, full-field, turbulence simulator. The software uses a statistical model as opposed to a physics-based model in order to numerically simulate the time series of wind. The input file generated is a time-series of three-component wind-speed vectors at different locations in a two-dimensional rectangular grid (Jonkman, 2009). For the generation of wind files, there are a couple of relevant parameters in which needs to be changed. These are listed in Table 6.4. The wind files generated are based on the selected environmental conditions related to the load cases established in Section 5.4.

Parameter	Value
Grid-point dimension	32x32
Hub height [m]	131.70
Grid height/width [m]	250x250
Surface roughness [m]	0.0003
IEC turbulence type	NTM/ETM
Turbulence model	Kaimal

Table 6.4: TurbSim input parameters

6.5.3 Turbine Controller

The wind turbine controller applied for this thesis is adopted from NREL Open-Source controller (ROSCO), which is configured according to the turbine properties. This controller applies the principle of variable-speed-pitch (VSVP), and in addition, peak shaving when approaching the rated wind speed of the turbine (Souza et al., 2021). The variable speed allows the rotor to turn at different speeds, while the variable pitch allows the blade pitch angles to be actively controlled and varied. The main objectives of the controller are explained in more detail in Bachynski-Polic (2022-b), but are mentioned here in short:

- Maximize energy capture
- Limit aerodynamic loads in high wind
- Damp out torsional resonance (e.g. drive train)
- Produce smooth power (power quality)
- Damp out other dynamic modes
- Limit actuator activity

For the control of the system, there exists different strategies for the different conditions. For basic control systems, the objective below rated wind speed is the maximization of the power capture of the turbine. This is done by the means of adjusting the torque while keeping the blade-pitch angle at zero degrees. Above rated wind speeds, the rotor speed does not increase. At the above-rated conditions, both the torque adjustment and the blade-pitch controller are active. For the generator torque, there are two options for the generator torque specified as:

- Constant power: The generator torque is adjusted to maintain constant power
- Constant torque: The generator torque is kept constant when the rotor speed is above or equal to the rated speed. This strategy is mostly used for FWTs

For the second option, the constant value may be found if the rated power and rated generator torque is known as:

$$Q_{gen} = \frac{P_{rated}}{\omega_{rated}} \tag{72}$$

Here, P_{rated} is the rated power and ω_{rated} is the rated rotor speed.

6.5.4 Quadratic Drag

As mentioned previously in Section 3.4, the wave loads are estimated on the submerged parts of the floater by the means of Morison's equation. To apply this calculation in SIMA, the different parts of the submerged semi-submersible had to

be discretized into slender elements. The floater consists of three surface piercing columns, and three cubic pontoons connecting them. The quadratic drag contribution on these elements are to be calculated by the means of strip theory within the SIMA workbench.

Table 6.5 presents the non-dimensional drag coefficients following the guidelines of DNV-RP-C205, 2010. In addition to this, some modifications are made to the damaged columns which is specified in detail in Section 6.6.3

	C_D
Column	1
Pontoon, z-axis	1.4
Pontoon, y-axis	2.3

Table 6.5: Slender element drag coefficients in SIMA

6.6 Mooring System Design

For the selected location of the thesis, a water depth of 300 m is chosen. For this depth, a new mooring system configuration is required for the FOWT. The design of the mooring system is adapted from the preliminary mooring system design as used in Souza et al. (2021). This design consists of three hybrid (chain+polyester) catenary mooring lines. The difference in depth is accounted for by the means of adjusting the pretension of the system in order to maintain the surge natural period.

6.6.1 Design

For the adaptation of the mooring system configuration to a new water depth, several procedures were performed. The first step of the process was the determination of the anchor radios. For this thesis, it was established by a factor relating the radius to the water depth, by the use of reference ratios based on existing facilities. The data was given in Wu et al., 2019, in which for a water depth of 300 m provided a factor of $R/d = 3.5$. This factor provided an anchor radius of 1050 m.

The second step is finding a value for the non-stretched mooring line. In this case it is assumed 1128m. Since the design is based on Souza et al. (2021) the same fraction of the chain-polyester-chain configuration is implemented to the assumed non-stretched mooring line length.

Lastly, a free decay test is performed in order to check the natural period in surge while adjusting the pretension in order to achieve the wanted natural period of 97.3s in surge for the respective FWT. The decay tests are presented in Section 7.3.

6.6.2 Final Mooring Configuration

The segments utilized for each of the three mooring lines have their own properties which are represented in Tables 6.6-6.7. Here, the mass/length of the first two segments account for 100mm marine growth, while the two last account for an additional 50mm growth.

Segment	**Type**	**Length [m]**	**Mass/length [kg/m]**	**Axial Stiffness [MN]**
1	130mm studless chain	40.6	377.7	1433
2	190mm polyester	138	60.7	228
3	190mm polyester	138	46	228
4	130mm studless chain	811.4	353.6	1433

Table 6.6: Mooring line properties (1)

Segment	**Equivalent diameter [m]**	**Ca,T**	**Ca,L**	**Cd,T**	**Cd, L**
1	0.234	1	0.5	6.1	2.9
2	0.190	1	0	2.5	0.1
3	0.190	1	0	1.8	0.1
4	0.234	1	0.5	4.2	2

Table 6.7: Mooring line properties (2), T - transverse, L - Longitudinal

From the design described in the previous section, the final configuration of the mooring lines are represented by their parameters in Table 6.8. Figure 6.7 displays the top view of the final mooring configuration within the SIMA workbench. The global SIMA coordinates of the mooring line configuration is presented in Table 6.9.

Property	Value
Water depth [m]	300
Number of mooring lines	3
Angle between lines [deg]	120
Anchor radius [m]	1050
Non-stretched mooring line length [m]	1128
Pretension [kN]	2768

Table 6.8: Mooring line configuration

	Fair-lead			**Anchor**		
Line nr.	x [m]	y [m]	z [m]	x [m]	y [m]	z [m]
ML1	42.7	0	0	1092.9	0	-300
ML2	-21.4	37	0	-546.46	946.5	-300
ML3	-21.4	37	0	-546.46	-946.5	-300

Table 6.9: Fair-lead and anchoring positions in global system

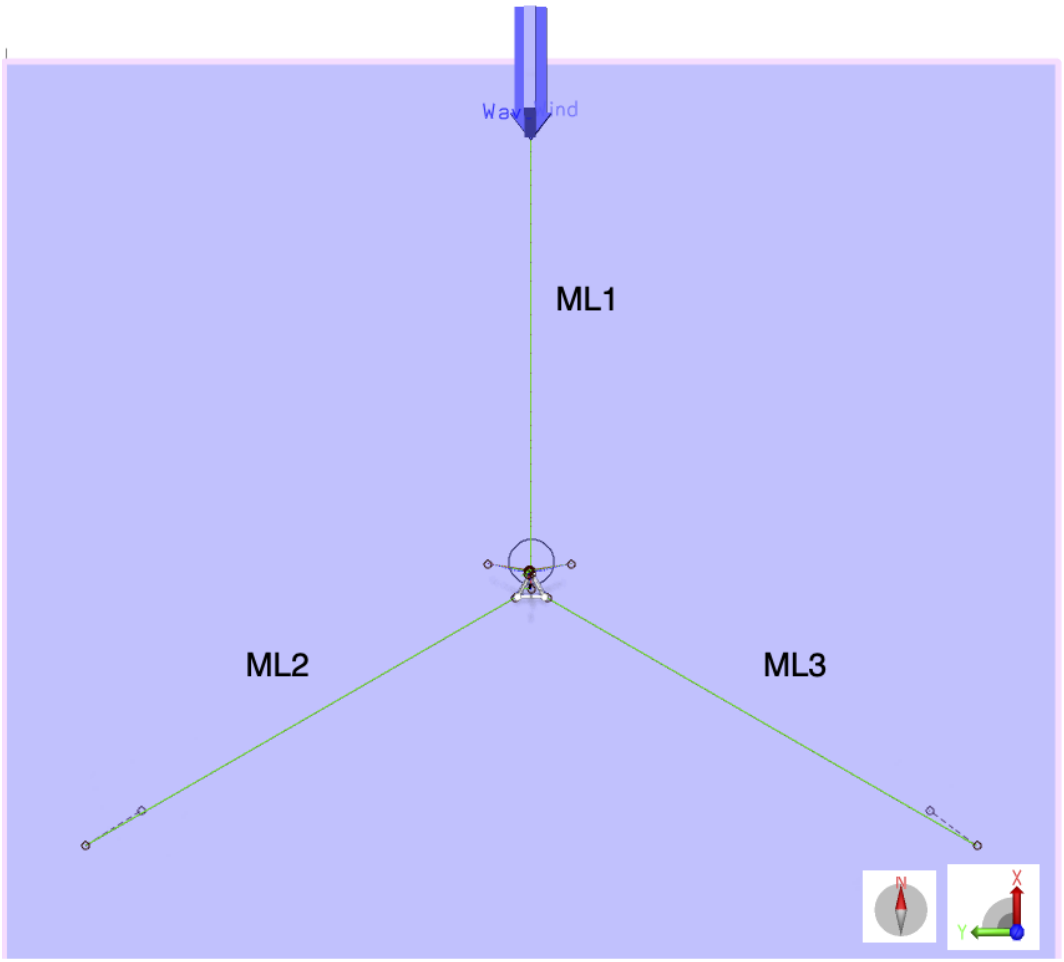

Figure 6.7: Top view of mooring configuration from SIMA

6.6.3 SIMA Coupled Model for Damage Conditions

In addition to the SIMA environment configured for the intact condition, environments has to be configured for the damage conditions as well. For the establishment of these environments, the same principles as for the intact conditions has been applied. The hydrodynamic results files used in these environments corresponds to the ones for the damage cases in which were extracted by the means of Wadam and HydroD. The hydrostatic corrections are performed similarly to the intact condition as seen in Section 6.5.1. As with the intact condition, the same mooring configuration is used.

The difference between the environments comes in the form of the hydrodynamic parameters, and the buoyancy. As mentioned previously, the buoyancy is specified as a direct force vector at the center of buoyancy. This center of buoyancy changes due to the damage in the different damage cases, and the center of buoyancy in the SIMA environments is updated correspondingly. This leads to the first limitation of the environments. If one were to change the position and inclination of the model in the SIMA environment, the coordinates of all the components have to be modified as well. This task is tedious and often leads to the simulations not running, and hence, the change in waterline is neglected. The inclinations of the platform is accounted

for by the change in center of buoyancy. Together with this, an additional time interval is included at the start of each run so that the platform may reach its proper equilibrium condition.

Another factor to account for is the drag formulation. For the damage cases, the waves propagate along the x-axis, and hence, the issue of misleading drag forces is not as critical for damage case 3 and 4. Despite this, in terms of damage case 1 and 2, the damage would face the waves, and will not experience drag in the same manner as of the intact condition. The drag coefficient of this column then has to be corrected. For this thesis, the drag coefficient of this platform is slightly reduced as specified in Table 6.10. It is then left as a research question up for discussion by the use of advanced computational fluid dynamics.

Damage case	Front column C_D
1	0.8
2	0.6

Table 6.10: Drag coefficient changes

7 Model Assessment

This section provides the verification of the numerical models established in the frequency domain before the transition into the time domain analyses. The first part of this section describes the properties and results for the intact condition established partly during the project thesis .

7.1 Hydrodynamic Analysis in HydroD, Intact Condition

7.1.1 Convergence Study

For the project thesis, a convergence study of the added mass, damping, response-, and wave transfer functions was performed for the structure in intact condition as shown in Figures 7.1-7.2. The results for the other degrees of freedom are included in the appendix in Figures A.1-A.4. The results shows the rate of convergence and were deemed satisfactory for the continuation of the thesis.

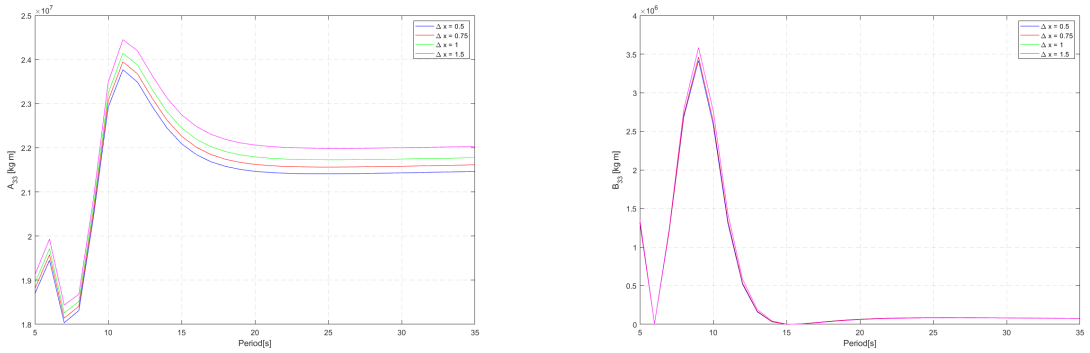

(a) Added mass (b) Damping

Figure 7.1: Convergence test (1) (**aarmo˙2021**)

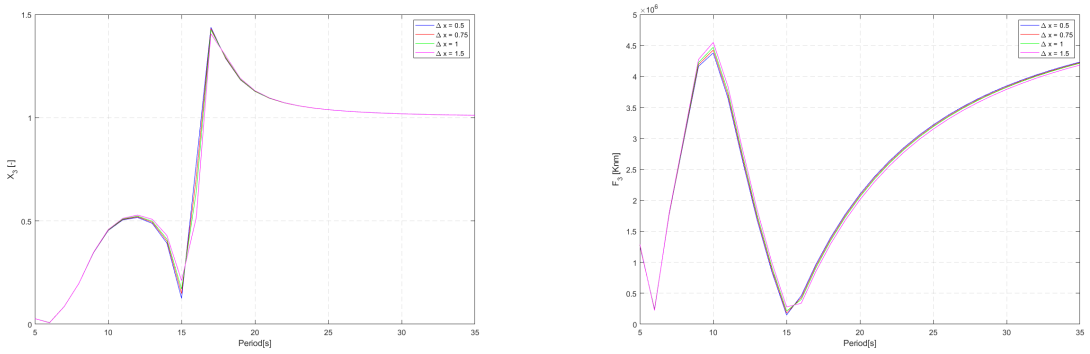

(a) Response transfer function (b) Wave force transfer function

Figure 7.2: Convergence test (2)

7.1.2 Verification Against Official Report

For the project thesis, a verification of the results was also performed up against the official hydrodynamic analyses performed by SINTEF. Since the SINTEF results only included the added mass and damping coefficients, these were the only comparisons performed. The comparisons may be observed in Figures 7.3-7.4, and the comparisons for pitch and yaw in the appendix in Figures B.5-B.6. The results display small differences from the official report, that are concluded to exist due to different mesh densities and period ranges and intervals.

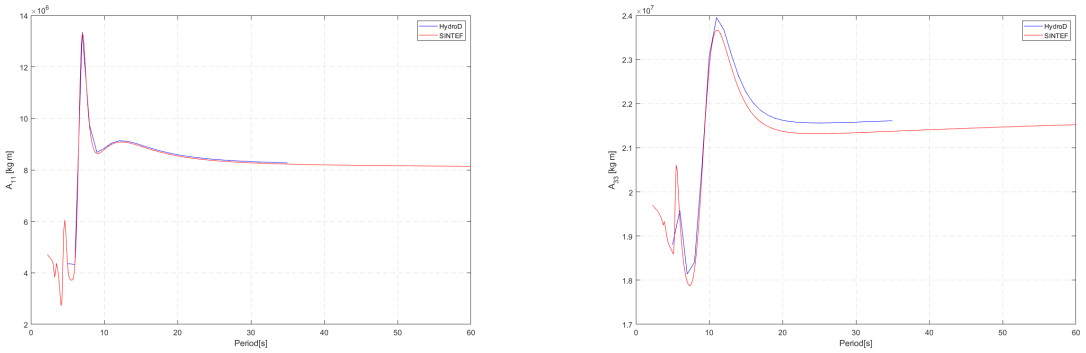

(a) Added mass surge (b) Added mass heave

Figure 7.3: Added mass verification up against official report

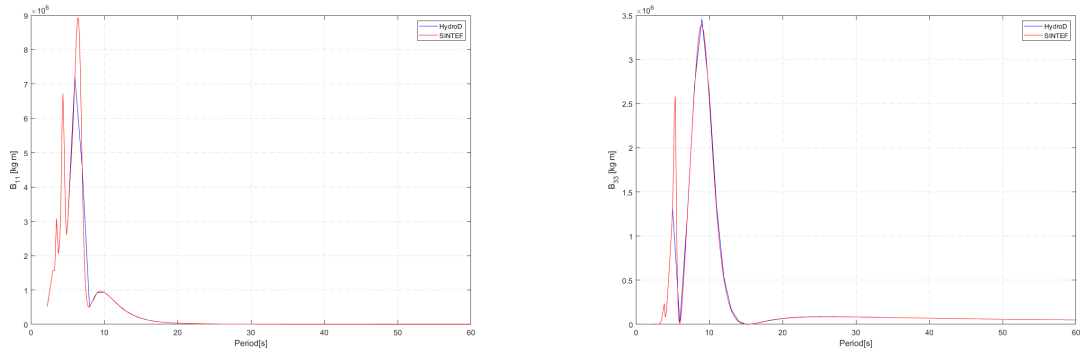

(a) Damping surge (b) Damping heave

Figure 7.4: Damping verification up against official report

7.1.3 Mean Drift Forces

There are two ways of calculating the second order mean drift forces in HydroD. It may be done by the means of the pressure integration method or the momentum conservation method. These calculations are performed by the means of Wadam, in which the pressure integration approach is often used with periodic boundary conditions which allows it to simulate the control volume around the structure. This is called the near-field approach, and is known to be a computationally expensive process. The momentum conservation approach is based on the principle of simulating

the behavior of the system using the principle behind conservation of momentum, and is called the far-field approach. Comparing the two, there exists possibilities of inaccuracy related to the pressure integration approach. This comes in the form of calculations close to sharp corners of the geometry in which would cause errors in the quadratic velocity term calculations from Bernoulli's equation (Faltinsen, 1999). In other words, the pressure integration approach is dependent on the quality of the meshed geometry. To investigate this, the mean drift forces of the two approaches are to be compared between two different mesh densities. The results are shown in Figures 7.6-7.8. The results shows that this is the case, and the continued thesis will still consider the $\Delta x = 0.75m$ mesh density.

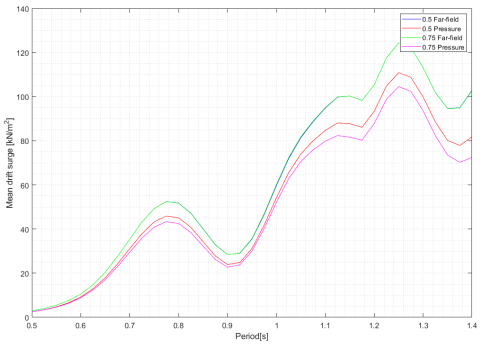

Figure 7.5: Mean drift forces surge

Figure 7.6: Mean drift forces in surge

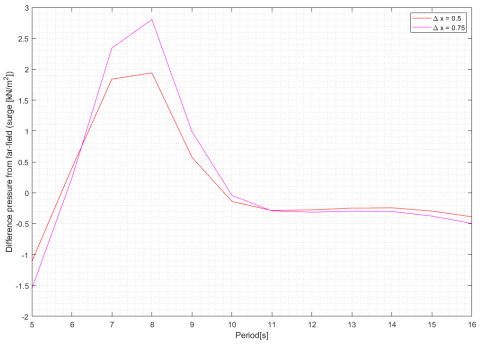

Figure 7.7: Mean drift forces difference in surge

Figure 7.8: Mean drift pressure vs. far-field difference

7.1.4 Quadratic Transfer Functions

Figures 7.9-7.11 represents the quadratic difference-frequency excitation loads for the surge, heave, and pitch degrees of freedom. These values are generated based on the performed second order frequency domain analysis which produced full quadratic transfer functions. Using these, the results were manipulated and visualized via Matlab. Something to consider for these graphs is the main diagonal of the contour and surface diagrams. Comparing the surge difference frequency excitation forces to Figure 7.6, one may notice that the difference frequency excitation diagonal retains the shape of the mean drift forces which is to be expected. For the three sets of figures, one may also notice the fact that the natural periods of the difference-frequency excitation forces appear quite far from the main diagonal, which is also to be expected. The smooth behavior close to the diagonal is to be expected in the surge and pitch QTFs (Haslum, 2000). In pitch on the other hand, the natural period appears lower, and the QTF experiences larger variations closer to the main diagonal.

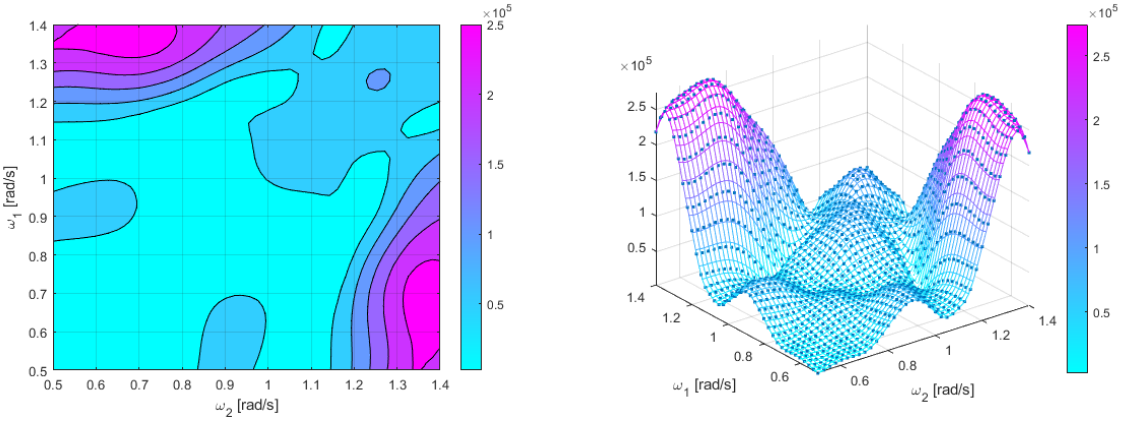

Figure 7.9: Difference-frequency QTF contour for surge (a) and surface diagram (b)

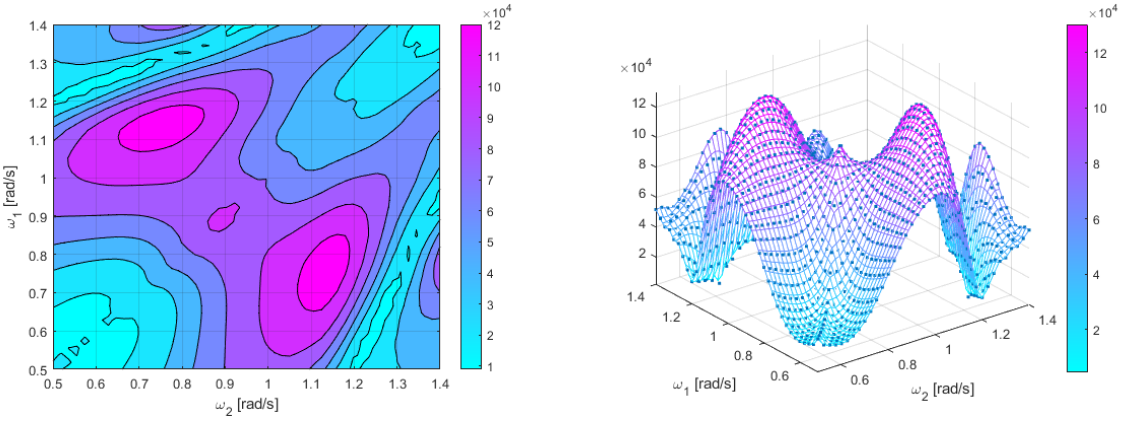

Figure 7.10: Difference-frequency QTF contour for heave (a) and surface diagram (b)

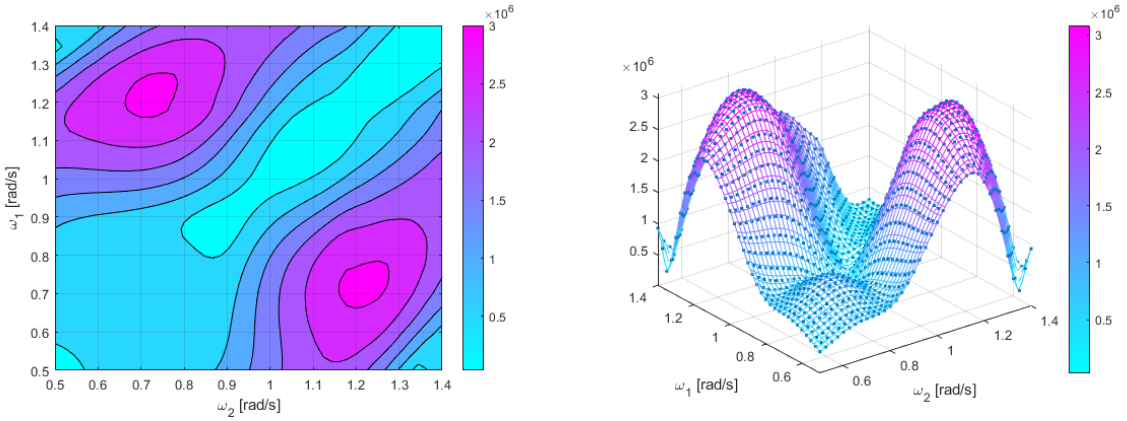

Figure 7.11: Difference-frequency QTF contour for pitch (a) and surface diagram (b)

7.2 Hydrodynamic Analysis Damaged Condition

For the four damage load cases established in Section 6.3.1, similar hydrodynamic analyses as with the intact conditions had to be performed which includes the first and second order frequency-domain analyses. This was performed in order to obtain the hydrodynamic coefficients, the quadratic transfer functions, the wave excitation force transfer functions, the RAOs, and the mean drift forces. These analyses were both performed for investigation purposes, but also for the continued use of the results in SIMA.

Error source: Mooring line stiffness should be changed due to a change in position. This might induce errors regarding the natural periods of the parameters.

7.2.1 Hydrodynamic Coefficients Comparison

For the several different damage cases, the first- and second-order frequency domain analyses were performed. This section presents the comparisons of the hydrodynamic coefficients obtained from these analyses in Figures 7.12-7.15 and in the Appendix Figures .9-.14. Considering the hydrodynamic coefficients being dependent on the body geometry, vicinity of free surface, water depth, water confinement and forward speed, large differences were not expected. This is shown in Figure 7.13, in which all of the damage cases remain almost identical despite their change in mass distribution and loading condition. This is also the case for the wave excitation transfer functions and response amplitude operators operating in one DOF only. Looking closer at Figures 7.13 and 7.15 one may notice that the off-diagonal components of the hydrodynamic coefficients and the mean drift forces are significantly more dependent on the loading condition and the mass distribution. This is seen due to the large change between the different damage cases. In order to investigate this further, Section 8.2 investigates the effect of the induced rotations due to the damage conditions.

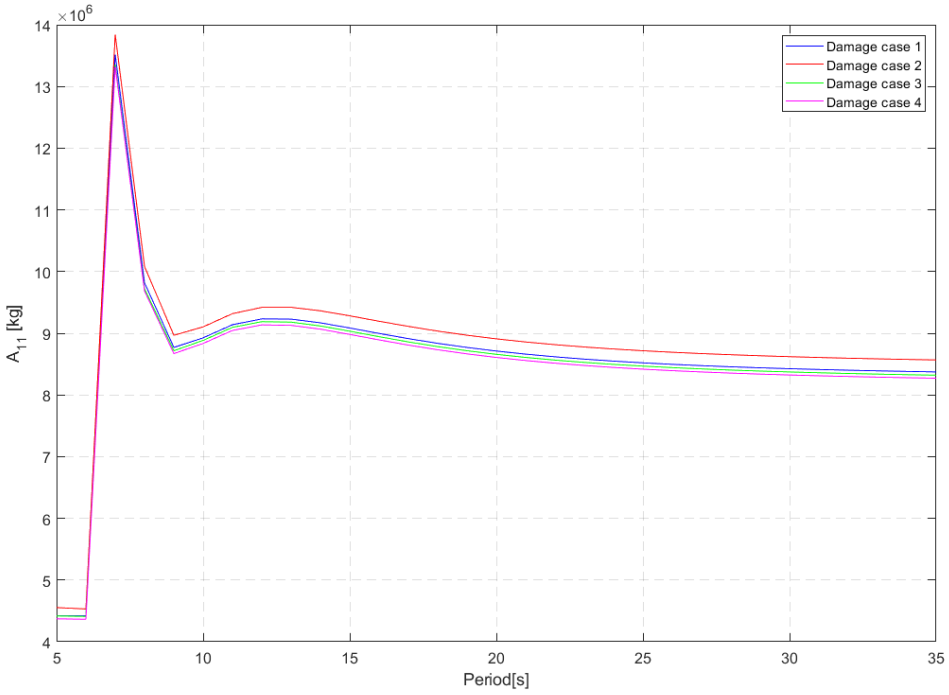

(a) Added mass surge-surge

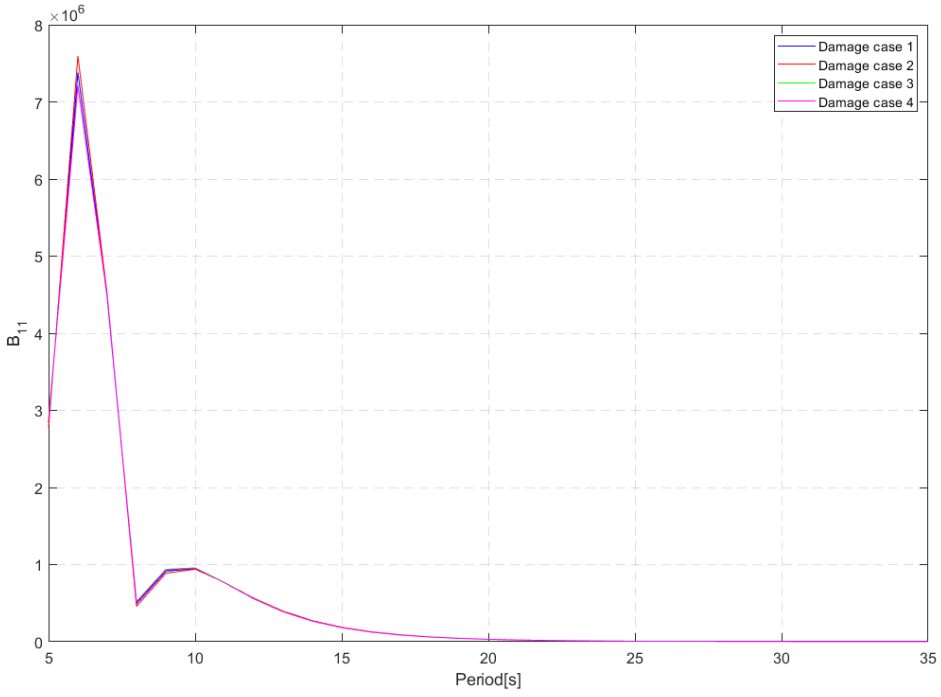

(b) Damping surge-surge

Figure 7.12: Added mass and damping comparison (surge-surge)

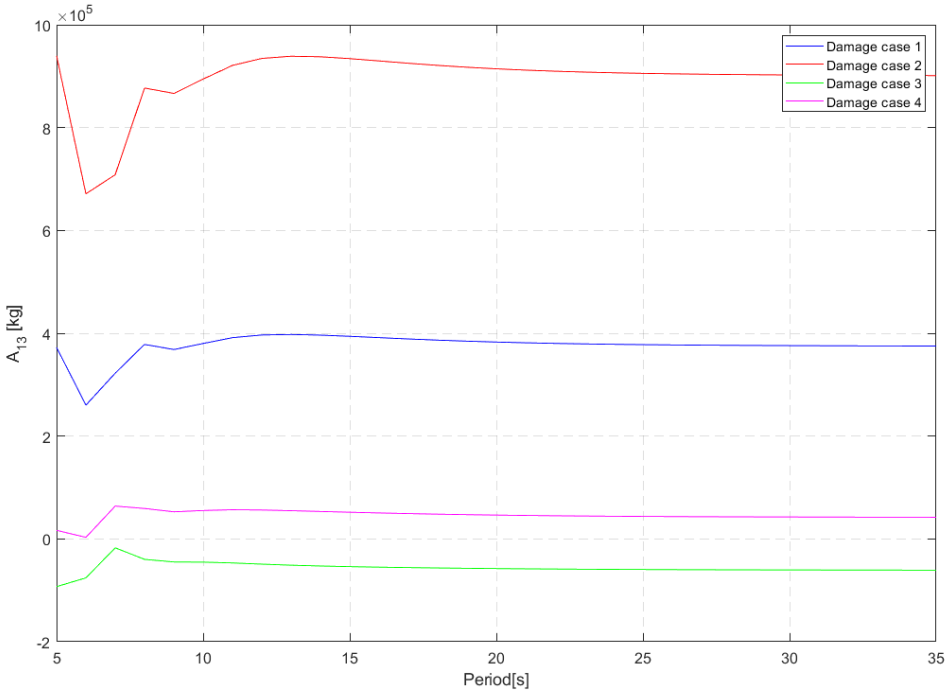

(a) Added mass surge-heave

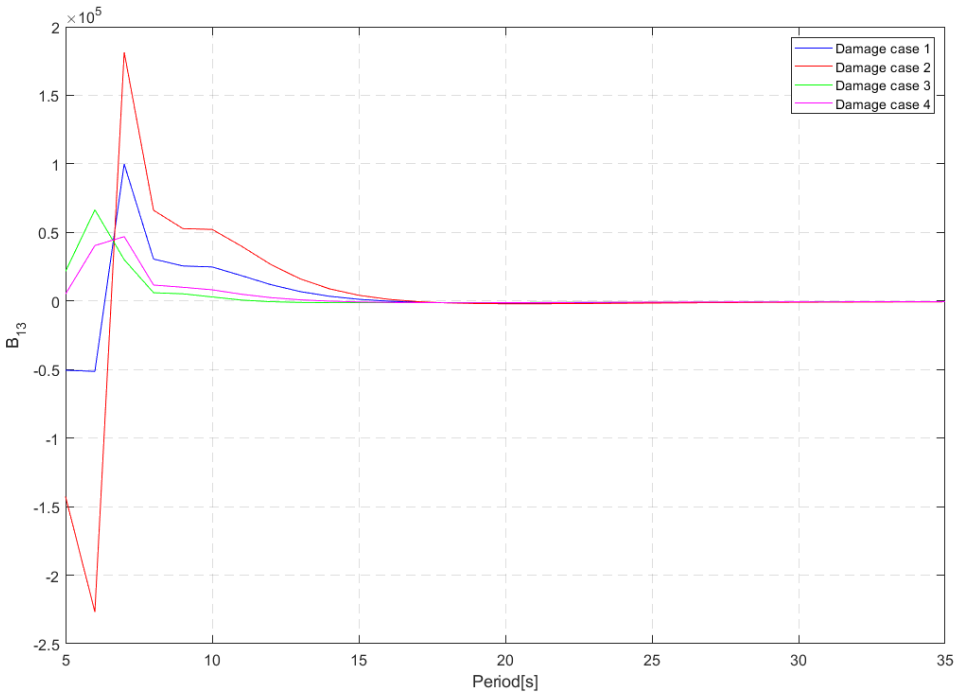

(b) Damping surge-heave

Figure 7.13: Added mass and damping comparison (surge-heave)

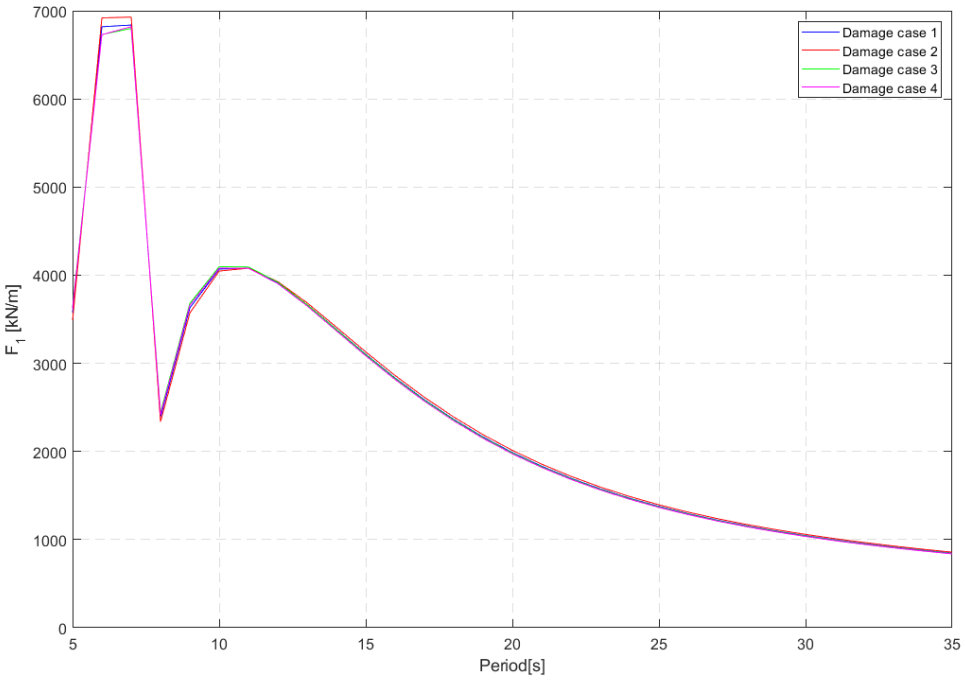

(a) Wave excitation transfer function surge

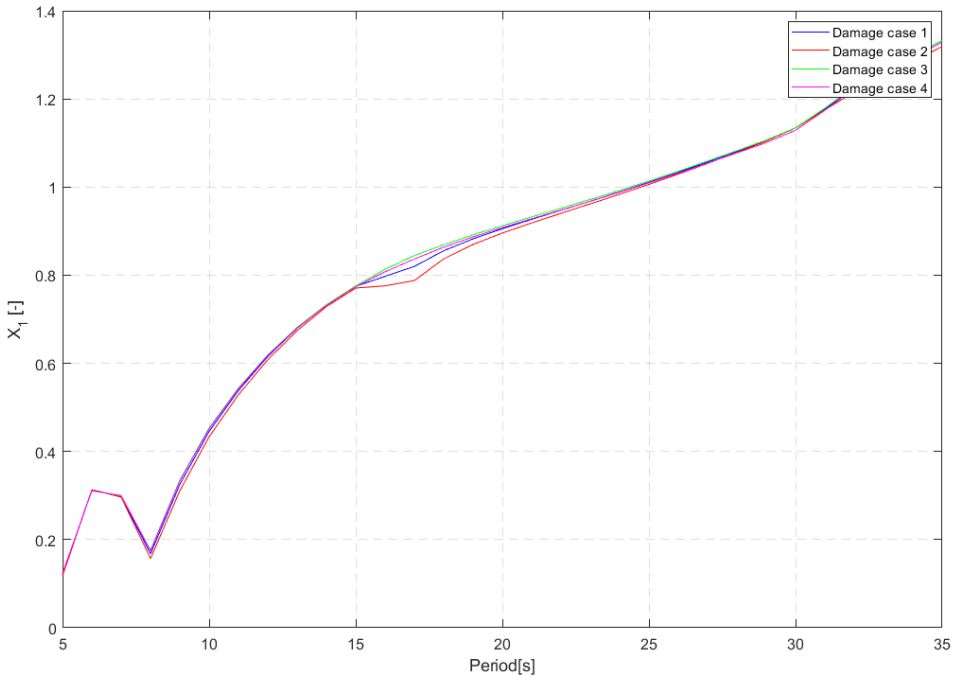

(b) Response amplitude operator surge

Figure 7.14: Wave excitation and response amplitude operator (surge)

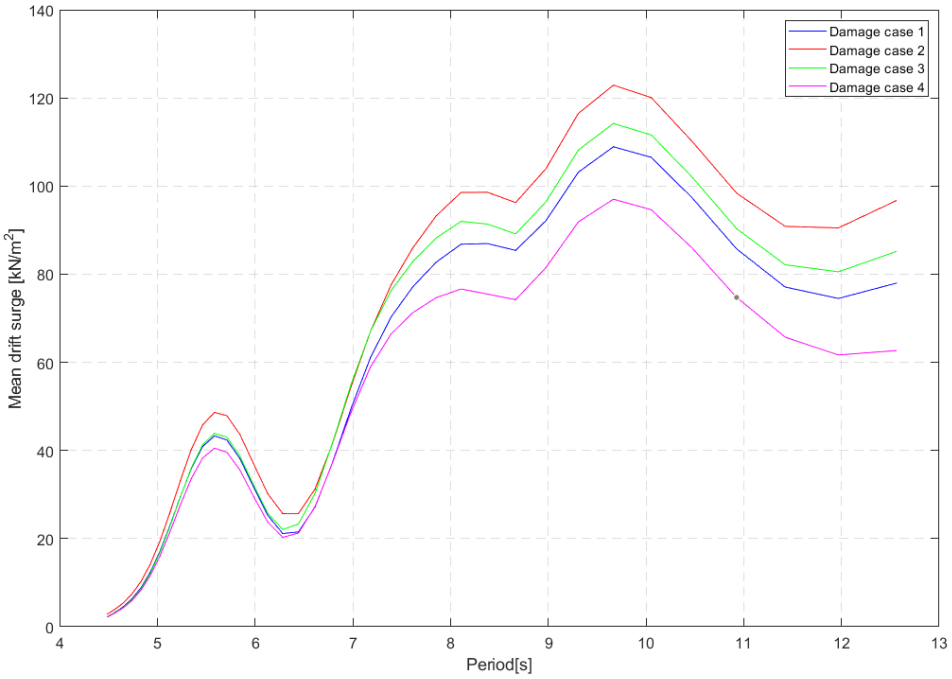

(a) Mean drift force surge

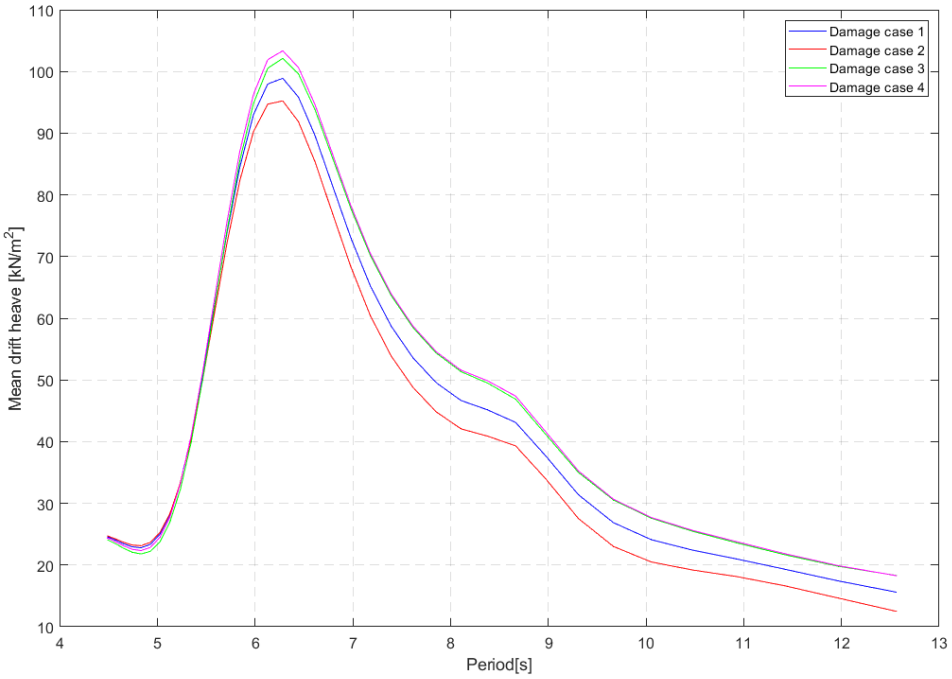

Figure 7.15: Mean drift force (heave)

7.2.2 Quadratic Transfer Functions

The quadratic second-order difference frequency QTFs may prove hard to compare considering their many dependencies. For the damage cases, small changes in the loading conditions are induced, and hence, a small difference in the QTFs are to be expected. Despite this, the general shape of the transfer functions are expected to remain similar. This section illustrates the results from the analyses, as well as it discusses some of the differences in comparison to the ones from Section 7.1.4 for the intact configuration.

Damage Case 1

Damage case 1 has experienced mild damage to two compartments, which are located in the positive x-direction. As a result of this, the structure is inclined, and experiences larger cross-sectional exposed areas in both surge and heave directions. For the surge QTF shown in Figure 7.16, one may notice a difference in peak values along the edges of the surface diagram. For the damage case, these are increased by about 32%. One may also notice some changes in peak resonance frequency combinations, in which for the damage condition, these move towards larger frequency variations of the two waves. Despite this, the general behavior is maintained. For the heave QTF displayed in Figure 7.17, one may notice similar changes. The rate of change of the QTF values increases, and the surface diagram appears steeper. This change is especially significant towards the higher frequency variations in which the change induces an even more significant change in resonant locations. For the pitch RAO displayed in Figure 7.18, the changes are less significant.

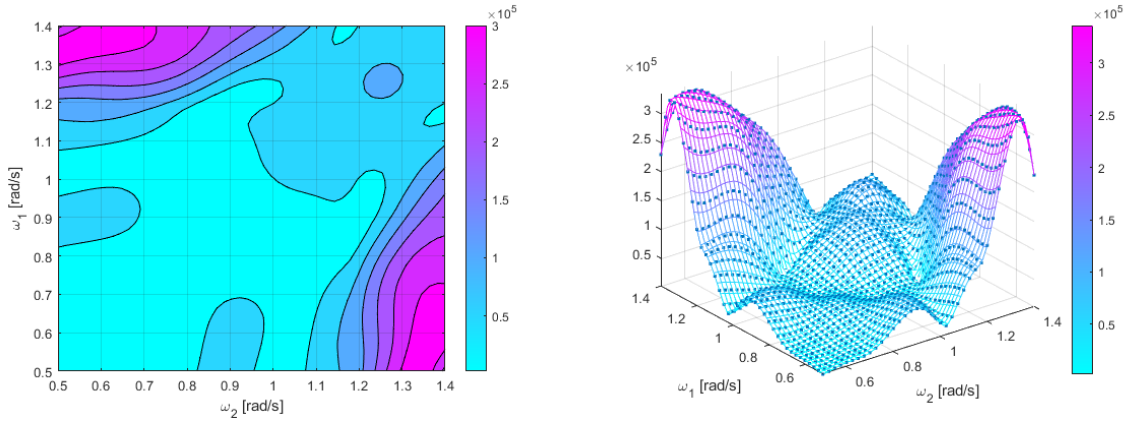

Figure 7.16: Damage case 1, difference-frequency QTF contour for surge (a) and surface diagram (b)

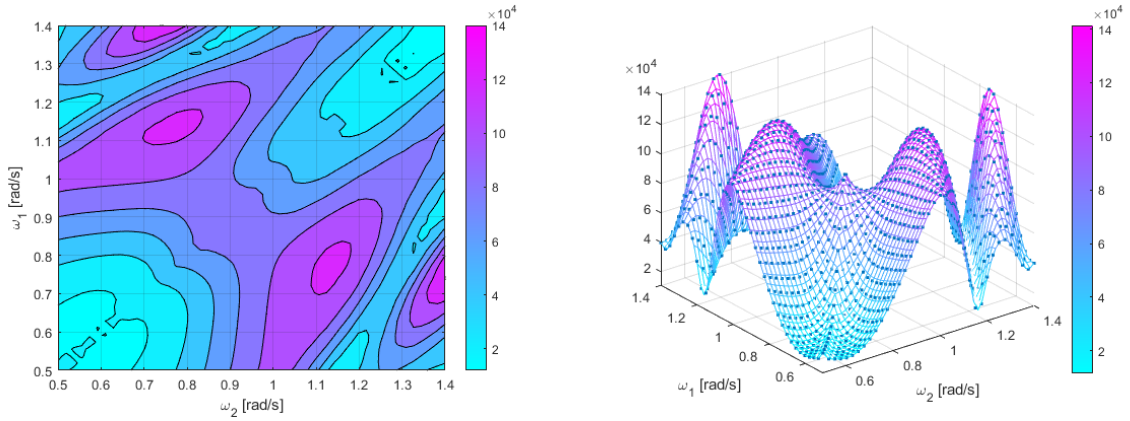

Figure 7.17: Damage case 1, difference-frequency QTF contour for heave (a) and surface diagram (b)

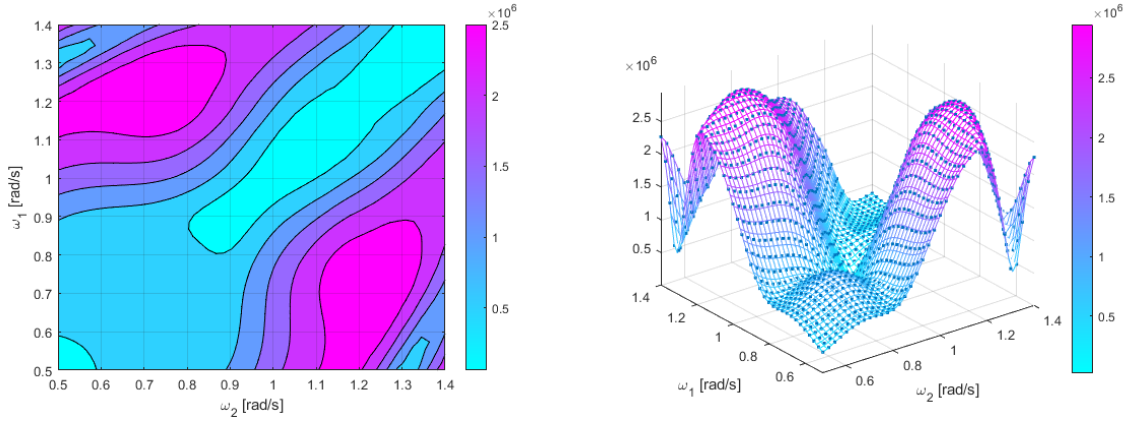

Figure 7.18: Damage case 1, difference-frequency QTF contour for pitch (a) and surface diagram (b)

Damage Case 2

The second damage case is similar to the first, but more severe. As a result, the quadratic transfer functions are expected to change even more due to the increased change in loading condition. Looking closer at Figure 7.19 representing the surge difference-frequency QTF, one may notice that this is not the case. One change may be observed in the contour diagram, in which the resonant peak along the main diagonal extends across a larger frequency area. One may also notice that the reduction appearing just outside the main diagonal and its trough appears closer to the main diagonal for the second damage case. In regards to the heave and pitch QTFs, no noticeable change occurs between the two damage cases.

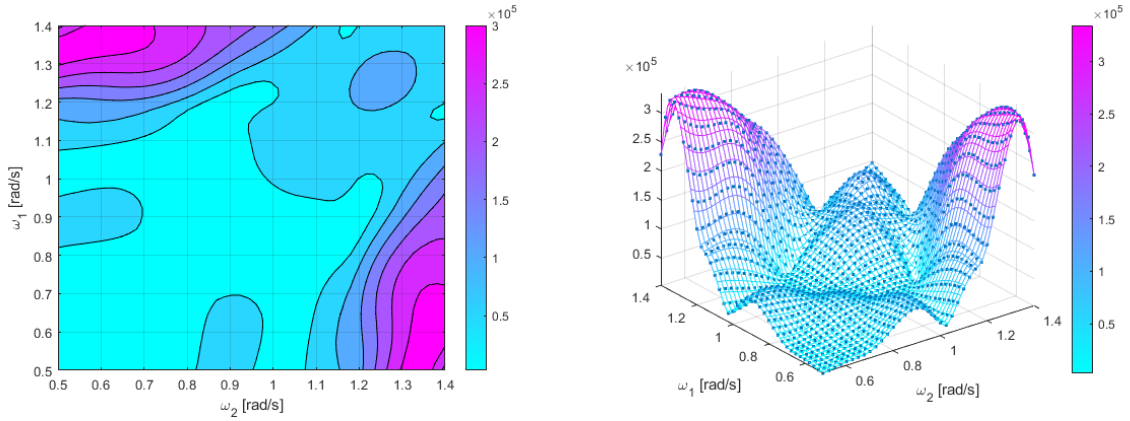

Figure 7.19: Damage case 2, difference-frequency QTF contour for surge (a) and surface diagram (b)

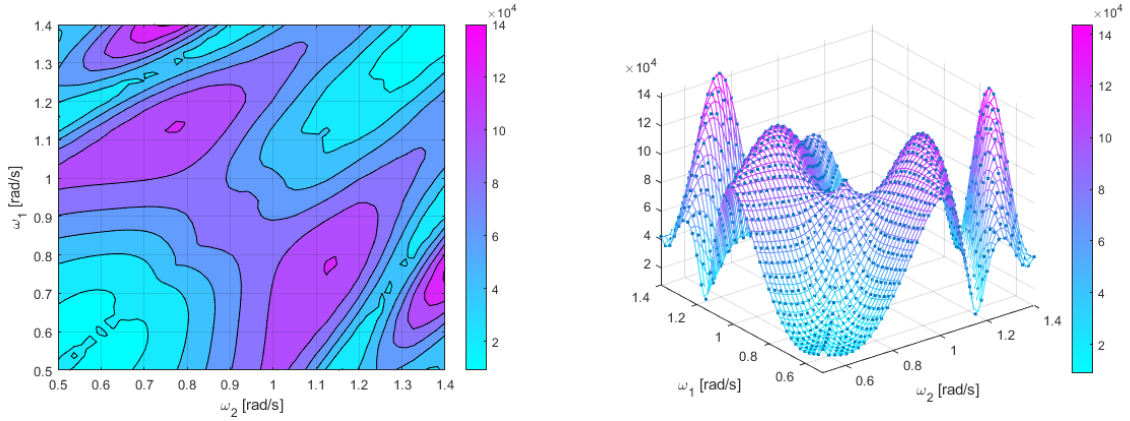

Figure 7.20: Damage case 2, difference-frequency QTF contour for heave (a) and surface diagram (b)

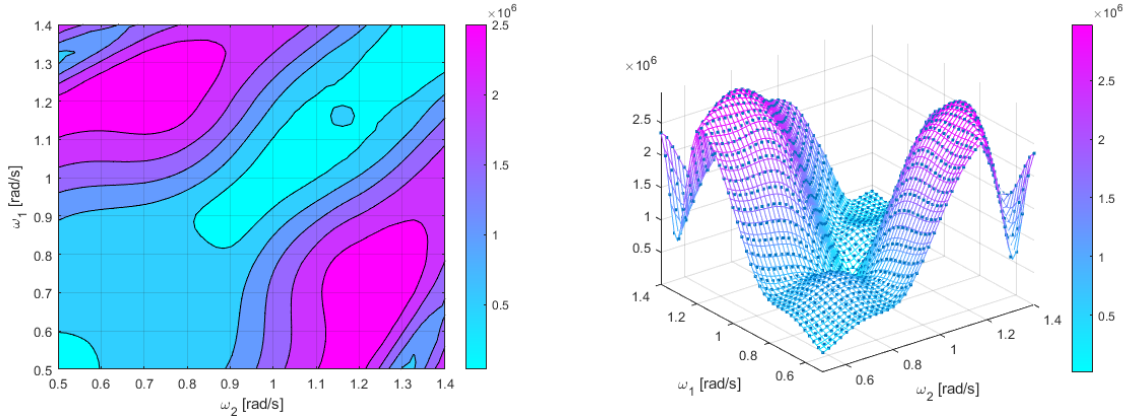

Figure 7.21: Damage case 2, difference-frequency QTF contour for pitch (a) and surface diagram (b)

Damage Case 3

For the third damage case, the damage appears on the outer perimeter of one of the two columns displaced from the origin on the y-axis. Here, two compartments are damaged, and hence, the in surge direction, the cross-sectional area is not increased by a large margin. The heave area is increased, and hence, the larger changes in the QTFs are expected to appear there. Looking closer at the surge QTF in Figure 7.22, one may notice the QTF retaining the behavior of the intact configuration both in terms of location of resonant frequency combinations, but also the magnitude at these locations. Moving onto the heave QTF in Figure 7.23 this repeats, and there are no significant changes in the diagrams.

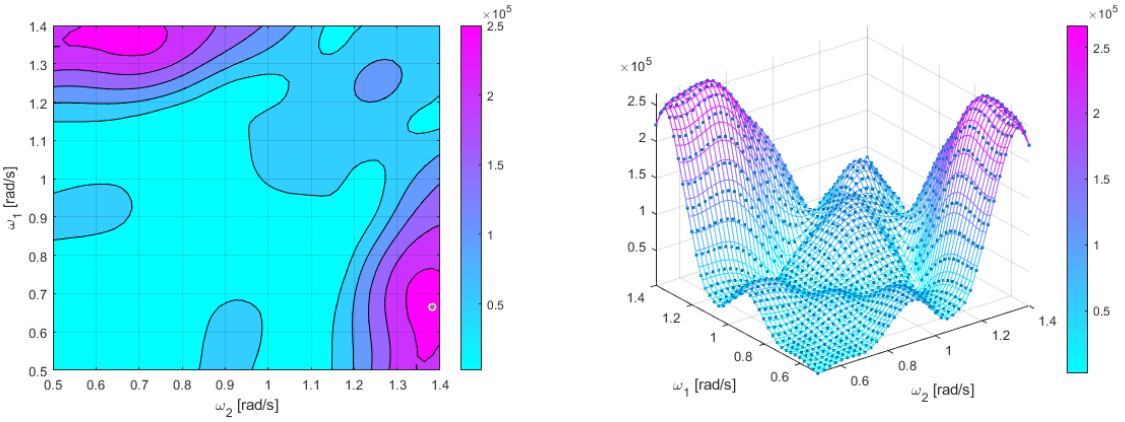

Figure 7.22: Damage case 3, difference-frequency QTF contour for surge (a) and surface diagram (b)

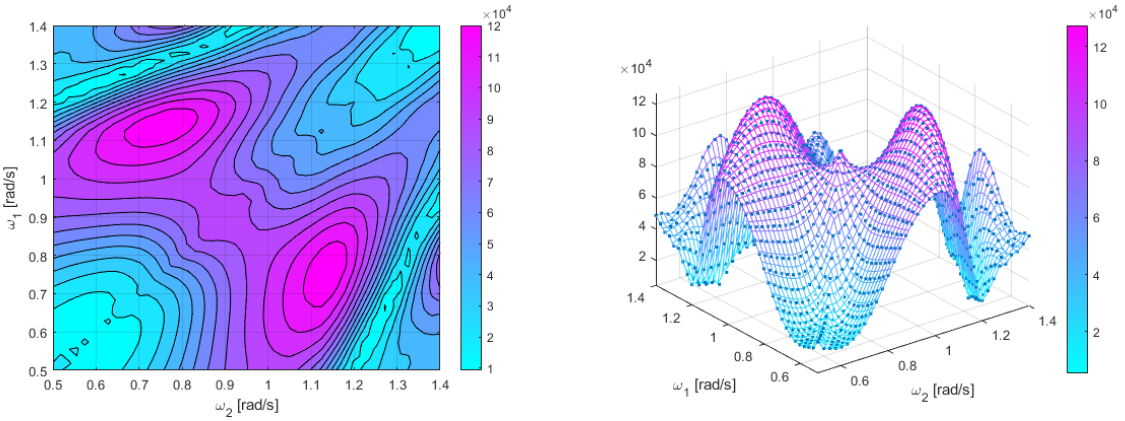

Figure 7.23: Damage case 3, difference-frequency QTF contour for heave (a) and surface diagram (b)

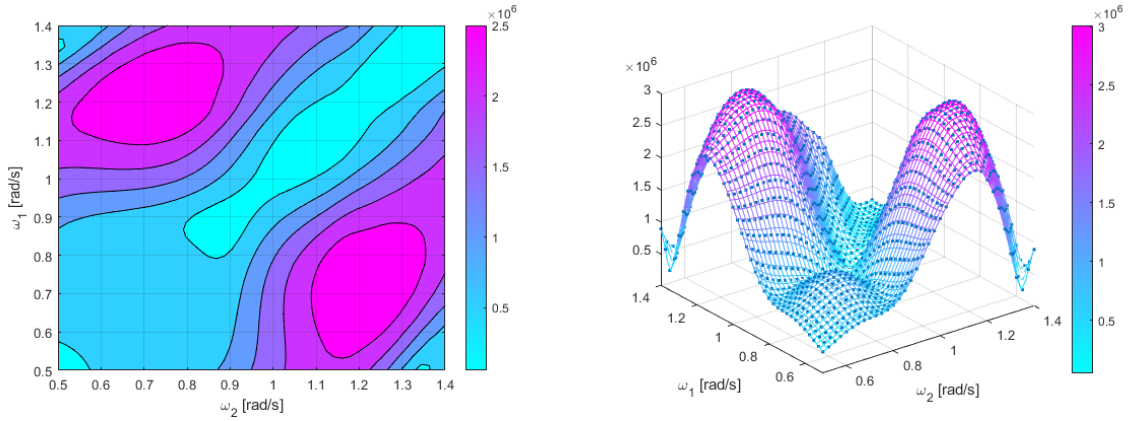

Figure 7.24: Damage case 3, difference-frequency QTF contour for pitch (a) and surface diagram (b)

Damage Case 4

Damage case 4 is of similar location to damage case 3, but has two additional compartments damaged. Focusing first on the surge diagrams in Figure 7.25, one may notice that the behavior has changed in a very similar manner to damage case 2. The difference between these two comes in the form of the frequency combinations close to the main diagonal. For damage case 4, the variations just outside the main diagonal are smaller, and the surface diagram appears more even. Moving onto the heave and pitch diagrams in Figures 7.26-7.27, one may once again notice similar behavior to the 2nd damage case. The differences here comes in the form of a change in peak values, in which the fourth damage case experiences a reduction.

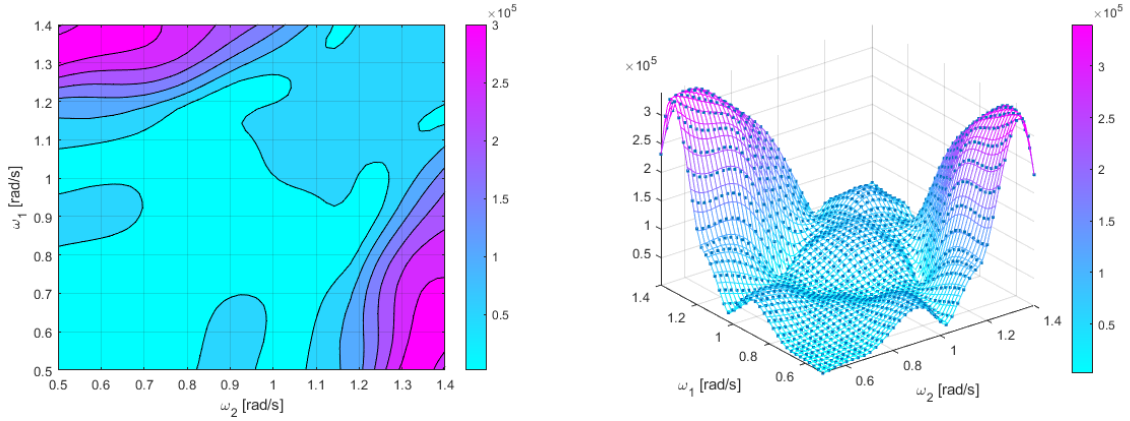

Figure 7.25: Damage case 4, difference-frequency QTF contour for surge (a) and surface diagram (b)

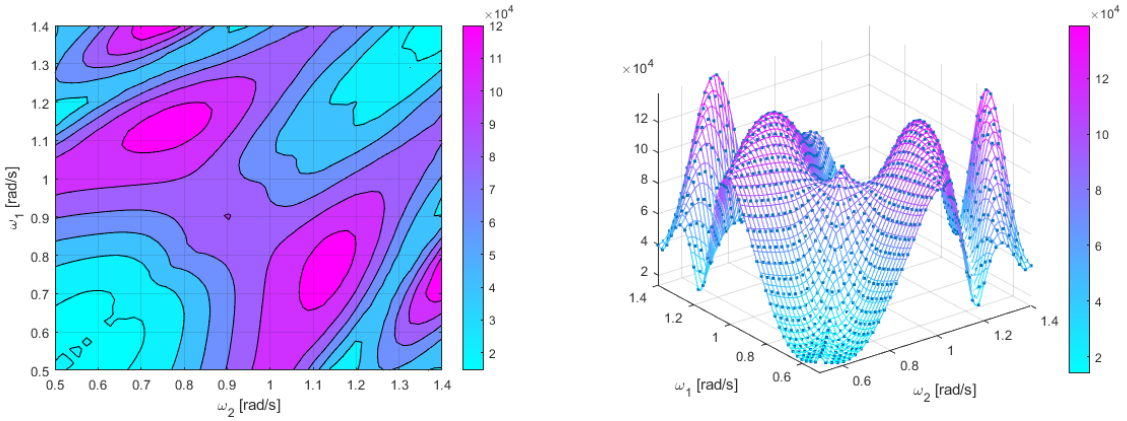

Figure 7.26: Damage case 4, difference-frequency QTF contour for heave (a) and surface diagram (b)

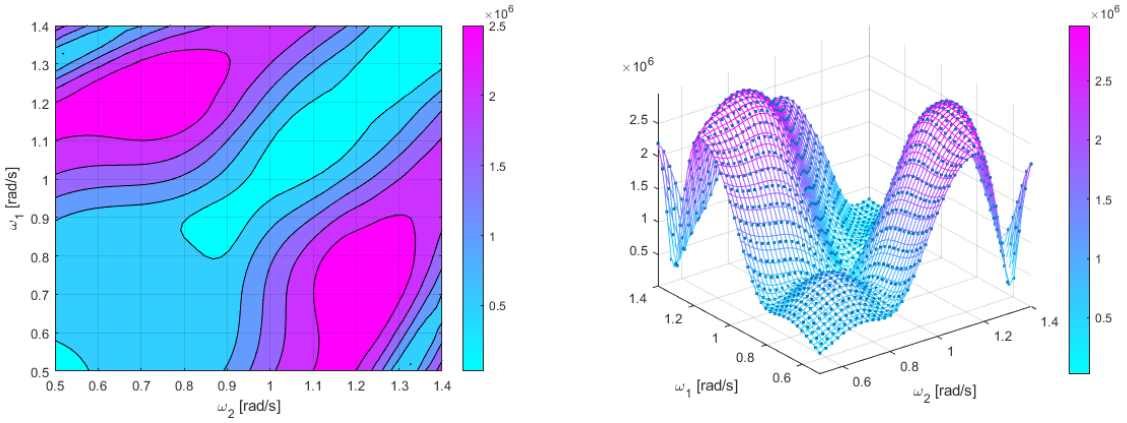

Figure 7.27: Damage case 4, difference-frequency QTF contour for pitch (a) and surface diagram (b)

7.3 Decay Test

The decay tests are performed for the documentation of the FOWTs natural period and damping. In this thesis, the free decay tests are performed for all the DOFs within SIMA. The initial displacements of the structure is achieved by applying a ramp force/moment, followed by a constant force in which both are applied at the global position [0, 0, 0]. After some time, the constant force will be released, and the achieved displacement will decay. This principle is displayed in Figure 7.28. The tests are performed in order to document the behavior of the structure without the interference of external environmental forces. Hence, for the condition of the turbine, it is set to a parked condition in which the turbine blades are feathered and fixed to the tower. Despite being a test in which neglects the environmental conditions, in order to make the simulation run, wind and wave conditions have to be included. In order for these to have a minimal effect on the platform behavior, the parameters are kept small. These environmental parameters are described in Table 7.1. The parameters applied in the simulations are displayed in Table 7.2, the corresponding results from the free decay tests is presented in Figure 7.29.

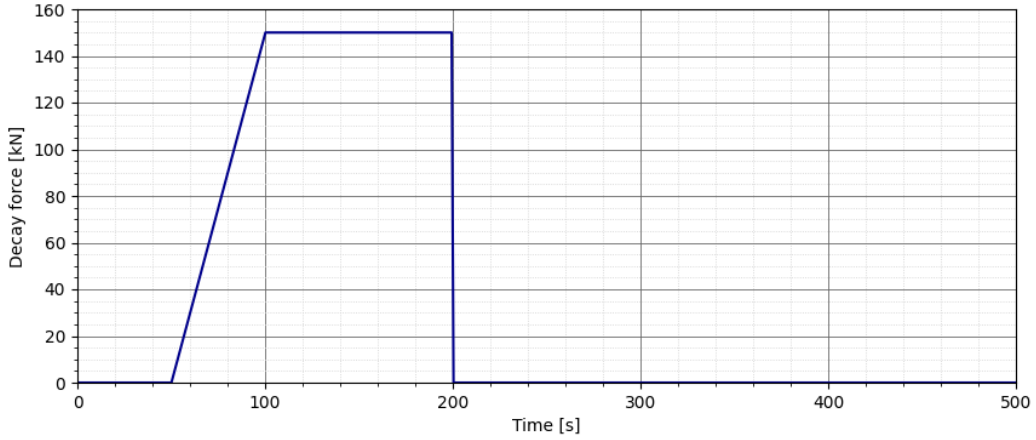

Figure 7.28: Example of decay test force parameters

H_S [m]	T_P [s]	U_w [m/s]
0.01	20	0.01

Table 7.1: Simulation environmental parameters

Motion	Force/Moment [kN/kNm]	Simulation Length [s]	Ramp duration [s]	Constant force duration [s]
Surge/ Sway	1700	1600	100	200
Heave	10000	800	50	100
Roll/ Pitch	220000	1000	100	100
Yaw	10000	1400	100	100

Table 7.2: Simulation parameters for decay tests

7.3.1 Intact Condition

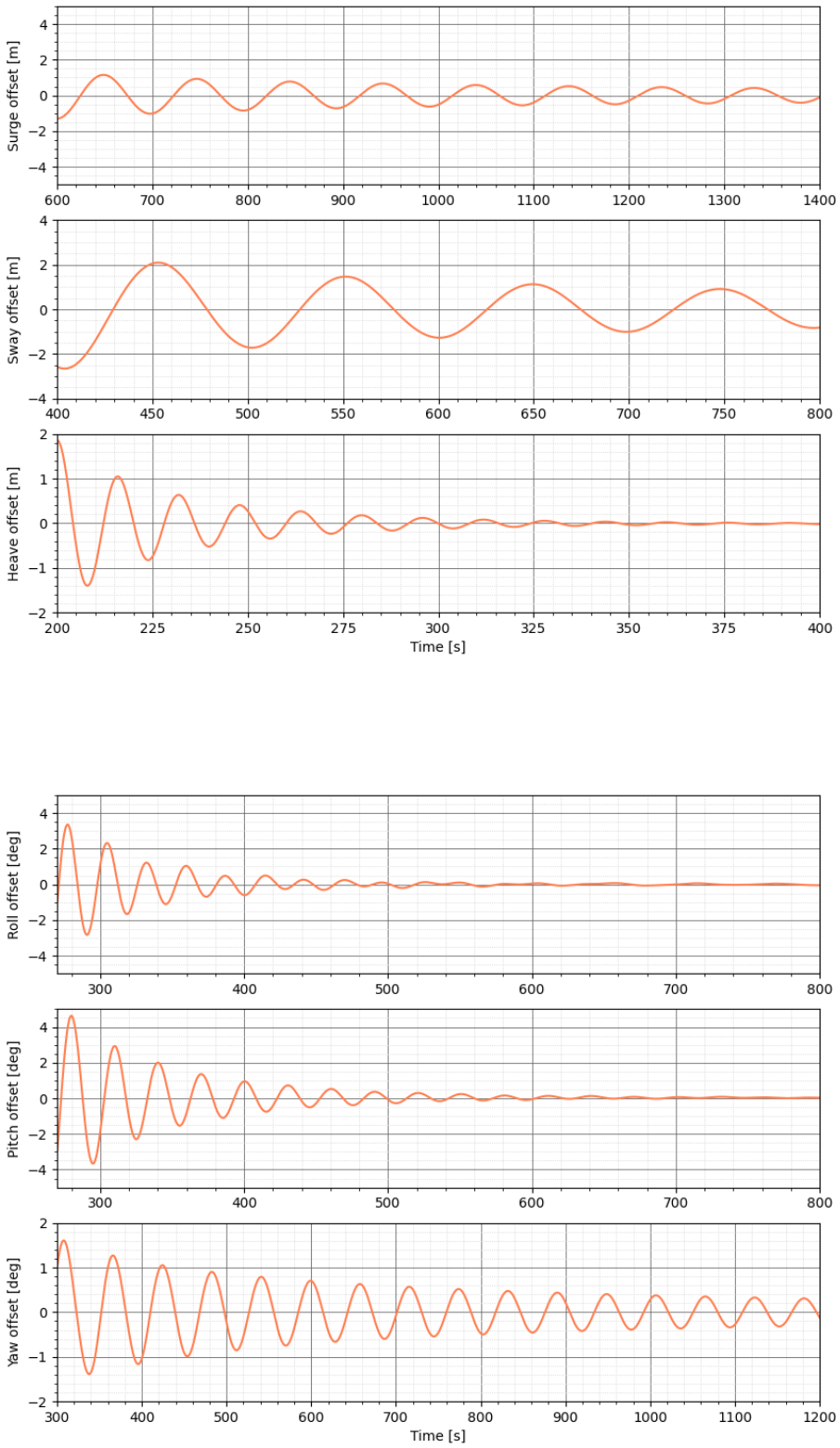

Figure 7.29: Decay test 6DOF

The result natural periods obtained from the free decay tests are presented in Table 7.3 along with the reference values from Souza et al. (2021). The results obtained from the simulation in SIMA correspond in a consistent manner with regards to the reference natural periods. The largest discrepancy from the reference periods occur for the roll and yaw motions. Here, the large discrepancy in the yaw period resides in the significant increase in pretension compared to the mooring system of the reference. Despite this, the tests prove sufficient results in regards to the verification of the model for further use in coupled time-domain analyses.

DOF	Free decay period [s]	Reference period [s]	Deviation [%]
Surge	97.4	97.3	0.10
Sway	98.3	98.9	-0.6
Heave	16.1	16.3	1.2
Roll	30	29.5	1.7
Pitch	30.1	31.4	-4.1
Yaw	58.3	88	-33.7

Table 7.3: Natural periods

7.3.2 Damage Cases

Decay tests were also performed for each of the damage cases in 3DOF. For these tests, little change in the systems natural periods were expected due to only small differences in hydrodynamic coefficients. The graphs for the decay tests for the damage conditions are included in Appendix F in Figures F.15-F.18. The calculated natural periods from the runs are presented in Table 7.4. Here, one may notice the small differences in the heave and pitch natural periods. These are similar to the natural periods for the intact configuration. When it comes to the surge natural periods, one may see larger deviance from the intact condition. Previously, changes in the cross-coupling terms in the hydrodynamic coefficients were observed, and this is believed to contribute to this change in natural periods. Despite this, the change in position due to the change in center of buoyancy may have an even greater effect. This change in position will cause a change in mooring line stiffness, and hence, the natural periods.

DOF	DMG1	DMG2	DMG3	DMG4
Surge	104.2s	104.6s	103.5	103.9
Heave	16.3s	16.4s	16.4	16.41
Pitch	30s	29.6s	29.8	29.7

Table 7.4: Natural periods damage cases

7.4 Regular Wave Test

The response amplitude operators were previously calculated by the use of Wadam in HydroD during the Master project thesis and may be observed in Appendix A in Figure A.4 . As an addition to the verification of the SIMA model, the response amplitude operators were also calculated in the SIMA environment. This was performed by exposing the FOWT to regular waves of amplitude $\zeta_a = 1$m with periods ranging between 5-35s with an interval of 0.5s. Each of the simulations were performed with a simulation time interval of 800s. The results displayed in Figure 7.30 are the averaged results of each condition which was taken after the transient phase had died out, and all that was left was the steady-state conditions.

In terms of comparison, the response amplitude operators correspond quite well with the ones produced in HydroD. Despite this, one may notice some changes. This is a result of a change in the mooring configuration. For the HydroD calculations, a dummy stiffness representing the mooring system is applied. Hence, the change in RAOs is expected. As a result of this, the RAOs were instead compared to the reference values from the Souza et al. (2021) report. These calculations were performed in the SIMA environment, with the same mooring configuration, but for a depth of 150m. Compared to these values, the RAOs correspond quite well. Taking this into account together with the decay tests presented in the previous section, the SIMA models were considered applicable for the continued use in simulations.

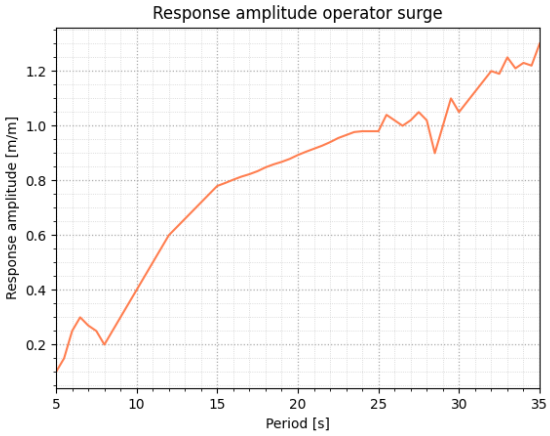

(a)

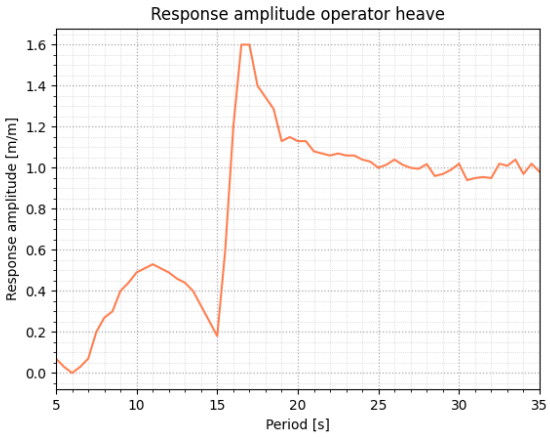

(b)

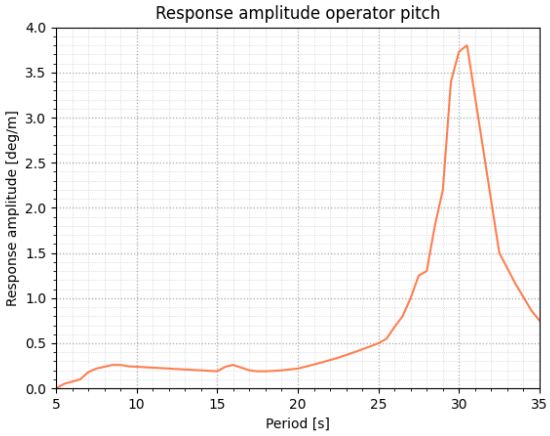

(c)

Figure 7.30: RAOs from regular wave tests in SIMA

7.5 Performance

The performance of the wind-turbine is to be checked in regards to the SIMA environment in order to validate its behavior for the continued use in operating analyses. In addition to validating the turbine itself, the tests also act as a verification of the controller applied to the turbine. In a similar manner to the previous tests, the simulations applied are of the time-domain configuration. The difference comes in the application of constant wind at wind speeds ranging from 4-24 m/s. The wind speeds are with an interval of 2 m/s, but includes the rated wind speed of 10.4 m/s. The wave parameters are kept the same as for with the decay test, and may be observed in Table 7.1. For the simulation, a step-wind input file is used in order to run through all the conditions in one single run. For this file, an initial period of 600s is included due to the fact that the turbine start-up takes longer for lower wind speeds. Then, each wind speed has a set duration of 800s in order to reach steady state results.

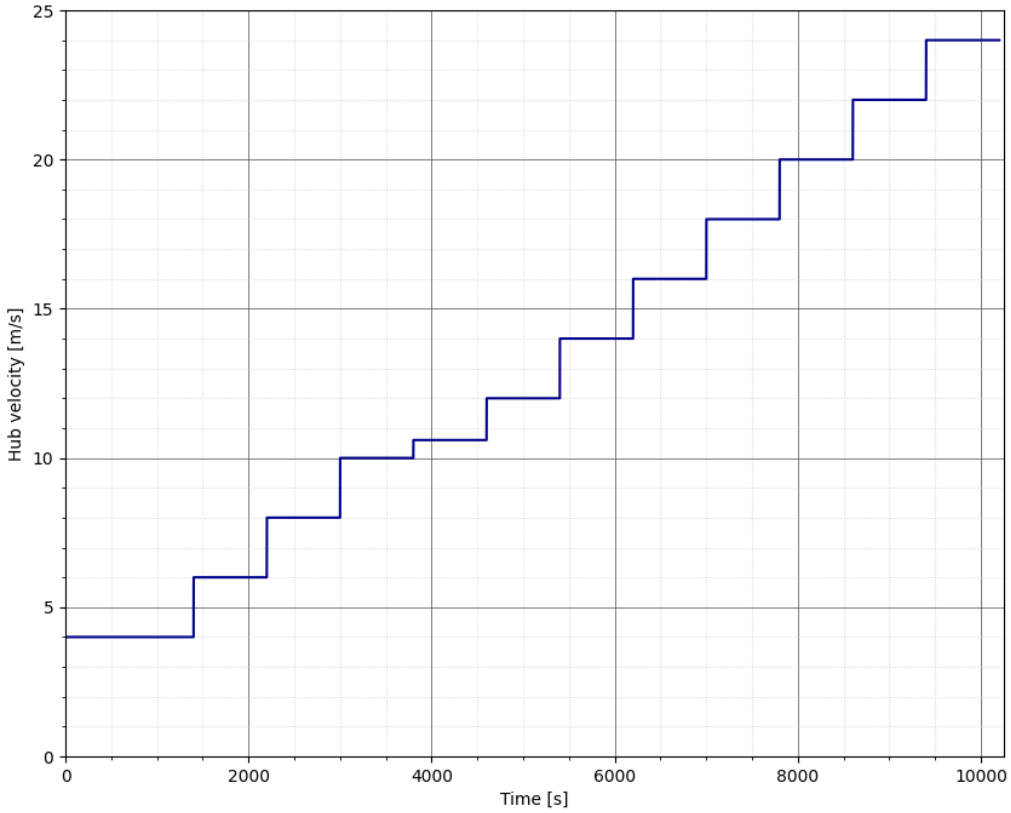

Figure 7.31: Step wind file for the performance simulations

The wind turbine performance curves may be observed in Figure 7.32. The statistics displayed are taken as an average of the steady-state conditions for each speed. In comparison to the reference performance curves presented by Souza et al. (2021), the results correlate in a good manner. Looking closer at the rotor speed, one

may see an increase up until the rated wind-speed. This is to be expected. The blade pitch controller may be observed in a pair together with the thrust force, in which one may notice the decreased rate of increase in thrust force after applying the pitching of the blades. Despite this, the thrust force increases, but is "shaved" before reaching its peak value. This is a feature of the controller applied in order to minimize the aerodynamic loads close to the rated wind speed. The generator power is kept close to constant after the rated wind-speed, in which is preferable. Hence, the performance of the turbine is proven sufficient, and ready for the continued simulations in operational conditions.

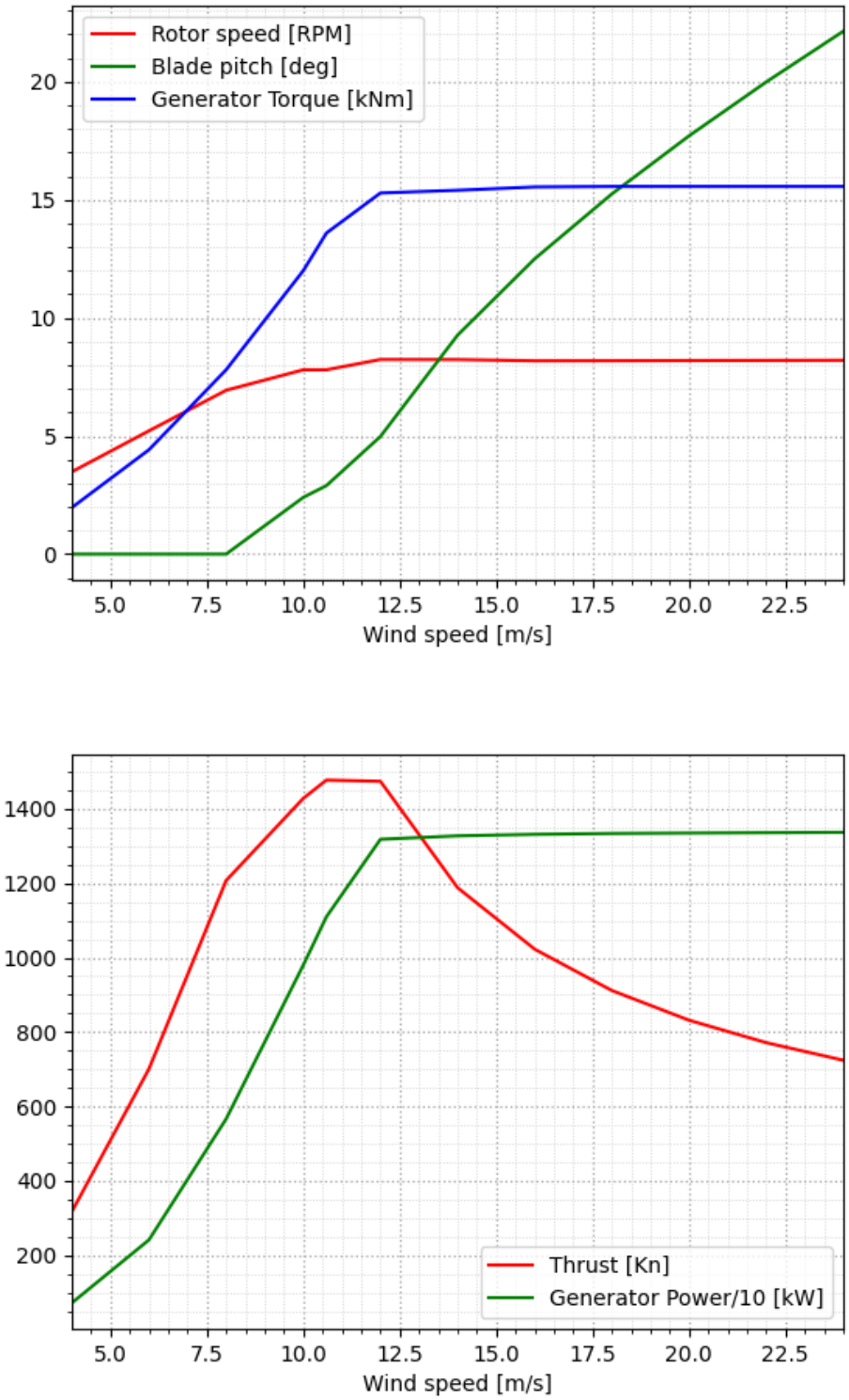

Figure 7.32: Performance curves from constant wind tests in SIMA

8 Analysis of Results

The results analysis is a continuation of the previous material presented, in which the analyses are targeted towards the response and behavior of the wind turbine in several loading conditions. The first two subsections goes further in-depth in regards to two additional findings from the frequency-domain analyses performed in HydroD, in which it should be noted that the model has been mirrored about the y-axis. The reasoning behind this comes from the SIMA environment being configured in a different manner, and from the fact that it was easier to update the HydroD parameters and results rather than changing all of the SIMA environments. The other subsections presents results from the coupled SIMA analyses. At that point of the study, the mistake regarding the mirrored results was uncovered, and fixed.

8.1 Newman's Approximation vs. Full QTF

This section investigates the applicability of Newman's approximation in regards to the estimation of the difference frequency excitation forces in surge. The reasoning behind only investigating the applicability in the surge DOF comes from the fact that it was discovered that the approximation was most reasonable for this direction. In addition to this, the second order difference-frequency analyses are only performed in one direction. The estimation is performed by the use of the main diagonal of the mean drift loads calculated by the means of pressure integration. If the model is made appropriately, these calculations should be identical. There are several dependencies in this case, but in most cases the important factors consist of the geometry modeled and the quality of the geometry meshed.

For this thesis, the damage cases are also of a big focus. As a result of this, additional results are included for one of the damage cases to look closer at the applicability of Newman's approximation in damage scenarios. The results from the frequency domain analyses are presented in Figure 8.1. When analyzing the results, one may notice the fact that the Newman's approximation and the quadratic transfer functions are identical for both the intact and damage condition. This is a good confirmation in regards to the applicability of both the panel model, but also the quality of the meshed free-surface.

Despite the Newman's approximation being a good estimate in terms of the surge difference-frequency QTF, the study is abandoned prior to the time-domain simulations. The reasoning behind this comes in the form of the other DOFs. From past studies its highlighted that Newman's approximation is questioned in regards to the non-horizontal DOFs, and hence, using these results in a simulation in which all DOFs are coupled becomes questionable and less accurate. Despite this, these results are highlighted as positive and applicable in single DOF analyses and simulations both for intact and damaged conditions.

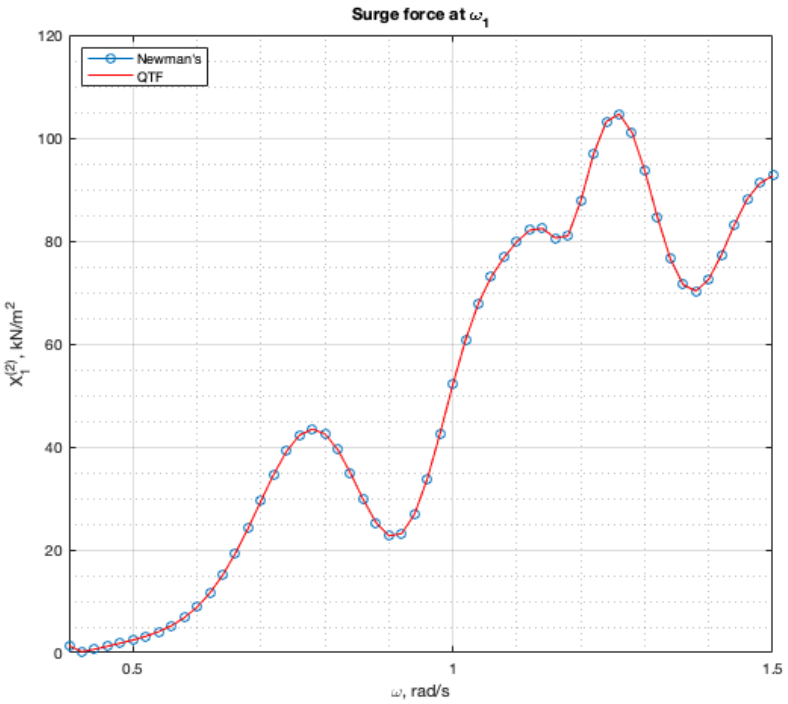

(a) Intact

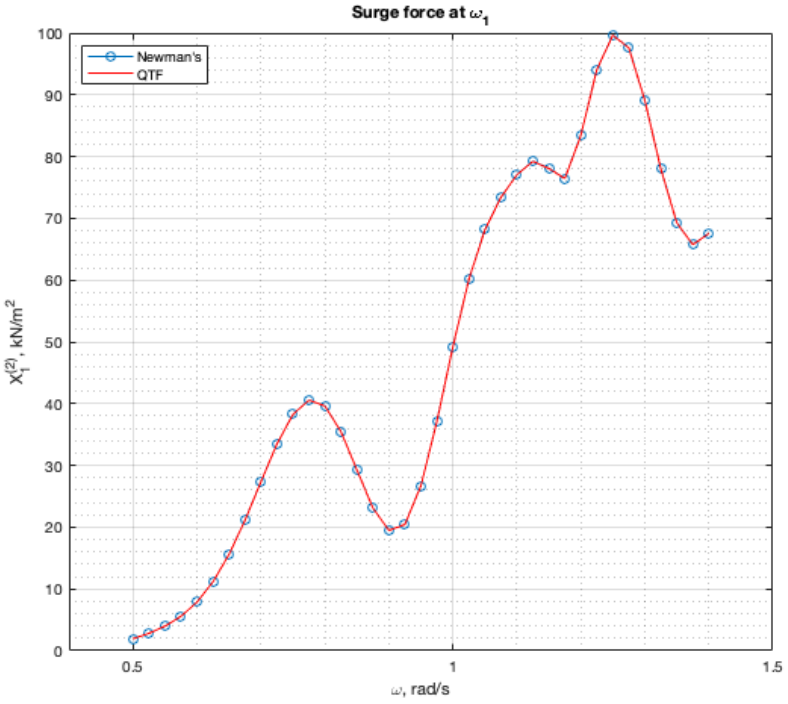

(b) Damage case 3

Figure 8.1: Newman's vs QTF (surge)

8.2 With and Without Applied Static Inclinations Damage Condition

This section was performed as a continuation of the second-order frequency domain analyses for the damage conditions. It was noticed that for non-symmetrical static inclination of the substructure, that the frequency-domain analyses could not be performed by the use of symmetric panel models. This causes the analyses to become more computationally expensive which isn't optimal. It was noticed that for the simulation parameters, that it was possible to manually force the inclinations to be neutralized after filling the compartments. As a result of this, the idea of running the model with an updated CoG, COB, and mass distribution without the updated inclination came to mind. If the changes between the results were minimal, this could be a large step in terms of performing analyses more efficiently in regards to non-symmetrically loaded structures. This study was performed simultaneous to the investigation in Section 7.2, and is of similar structure.

The frequency domain analyses were performed for damage case 2, which is one of the more severe damage cases in which the damage is located at the front of the substructure. Since the second-order results are also of interest, the same direction set as in Section 7.2 are used. In this case, it might have been more interesting to look into damage case 4, in which the exposed area would experience a larger change. This was not done, but despite this, interesting results were obtained. The results from the analyses are presented in Figures 8.2-8.5.

Looking first at the comparisons of the added mass and damping coefficients in Figures 8.2-8.3 one may notice similar changes to what's been shown in Section 7.2. When looking closer at the coefficients located on the main diagonal, one may notice little to no change in the results. For the low frequency values, this difference is negligible. The results for the other DOFs are not included but studied, due to similar differences. Despite this, one may notice that there is little to no difference in the other main-diagonal quantities as well. In regards to the off-diagonal coefficients on the other hand, the results are severely changed in a similar manner to the documentation in Section 7.2. In a pure one-DOF simulation, these results would be appropriate and applicable. Due to the highly-coupled system used in the time-domain simulations, this could prove to be an issue. This brings one to the force and response transfer functions of the body, in which the response is displayed in Figure 8.4. These calculations includes the overall effect of the cross-coupling terms. If one looks closer at the results one may notice little to no change between the configurations. For the surge and heave response, one may notice a slight deviations for higher wave periods, while the pitch response experiences a slight deviation at lower periods as well. Despite this, the deviations from the correct results are small. The wave force transfer functions are included in Appendix F in Figure F.19. The values presented experiences similar small deviations. Despite this, they are in the same way minimal.

Third, the results presenting the quadratic transfer functions presented in Figure 8.5 are looked closer at. For the results in the surge DOF, the results are approximately identical. A small difference may be noticed close to the main diagonal in which

the results excluding the inclinations of the substructure appears more even. For the heave results, larger differences may be noticed in which the peaks at frequency combinations of large difference. Here, the results with the inclinations are of increased magnitude, despite the change not being significant. The overall behavior of the surface diagram appears quite similar. For the pitch surface diagrams, one may notice that the through appearing along the main diagonal is more narrow for the results including the inclinations while the peaks at the largest frequency-difference are slightly increased.

Overall, the results with and without the inclinations appear almost identical, and of little to no difference. This should be further investigated in terms of time-domain analyses by the use of the results. The large changes in the off-diagonal terms leads to questioning in terms of how it would affect the results in coupled analyses, but it could be of large potential gain in terms of analysis time. The similarity between the condition might be due to the design of the substructure, and before concluding, one should keep in mind that this might just be different for another substructure design concept. The continued investigation of this hypothesis is performed in Section 8.5.

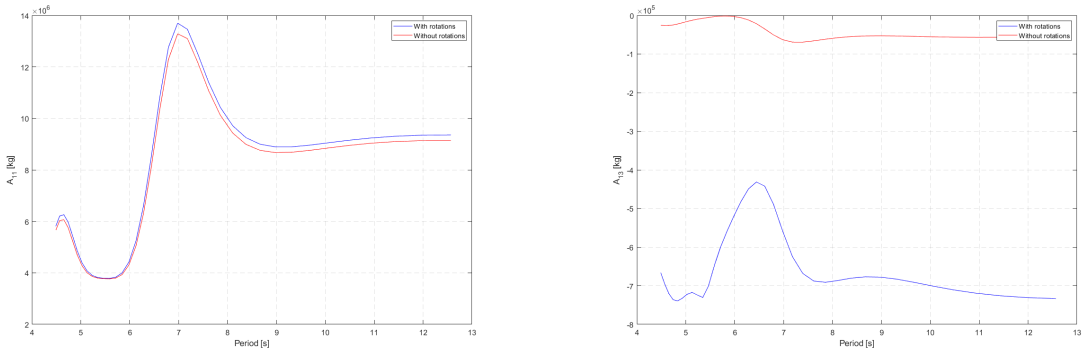

(a) Added mass surge-surge comparison (b) Added mass surge-heave comparison

Figure 8.2: Added mass comparison

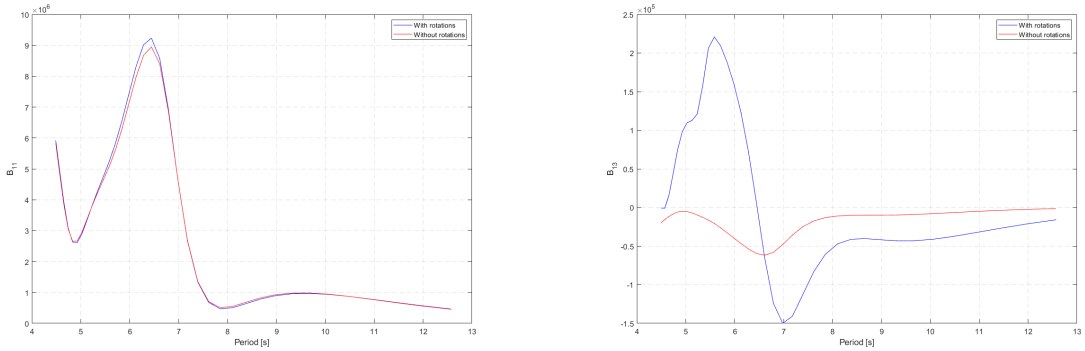

(a) Damping surge-surge comparison (b) Damping surge-heave comparison

Figure 8.3: Damping comparison

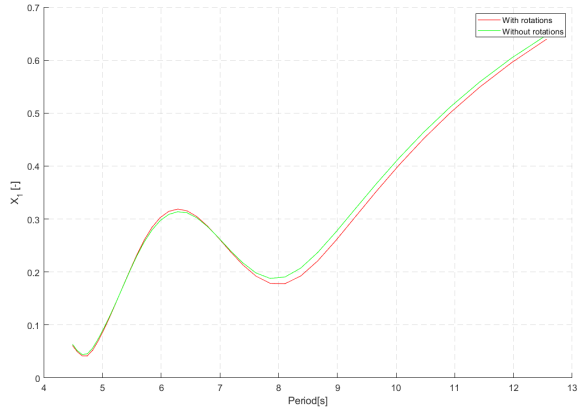

(a) Surge

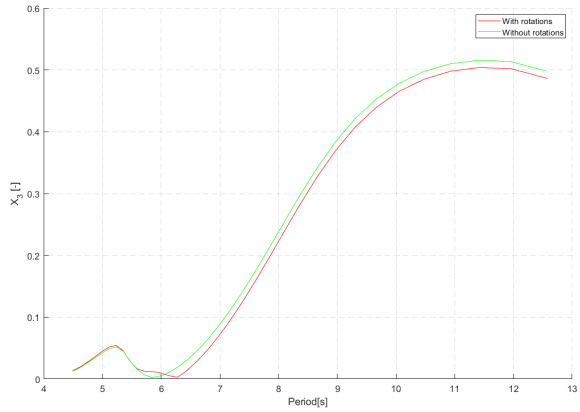

(b) Heave

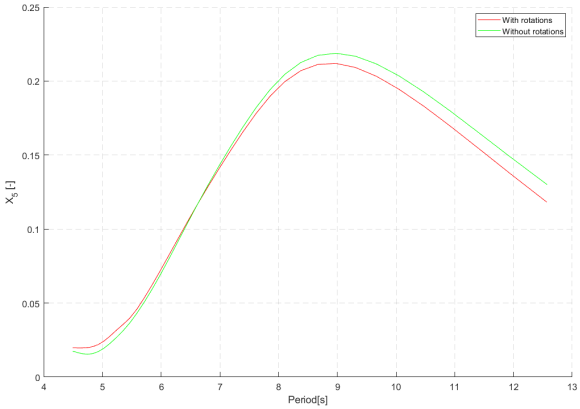

(c) Pitch

Figure 8.4: Motion transfer functions

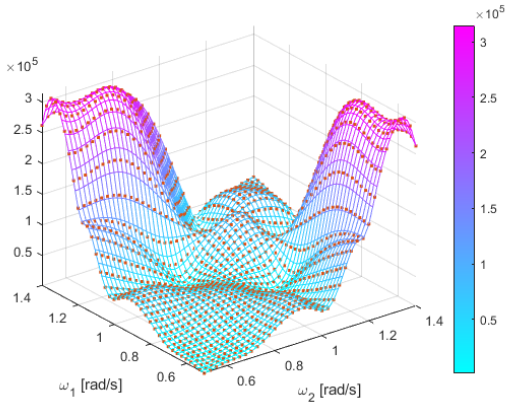

(a) Surge with inclinations

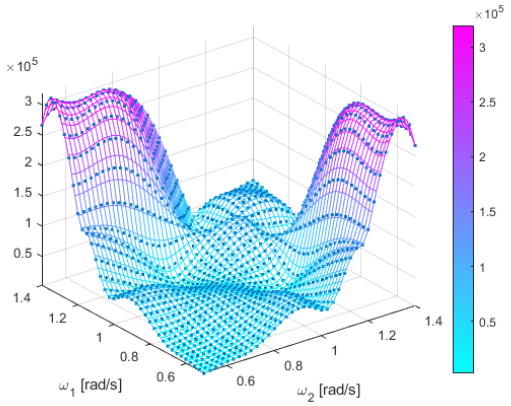

(b) Surge without inclinations

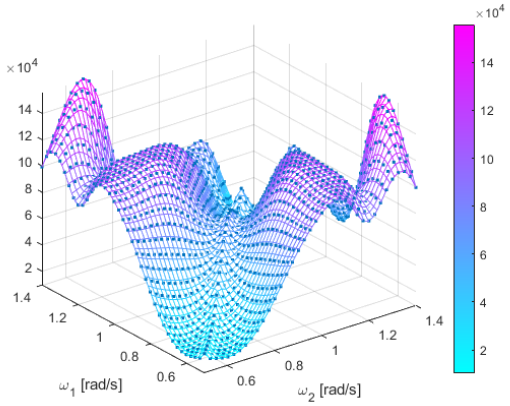

(c) Heave with inclinations

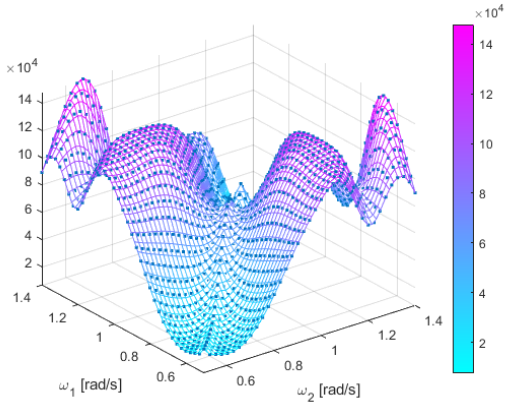

(d) Heave without inclinations

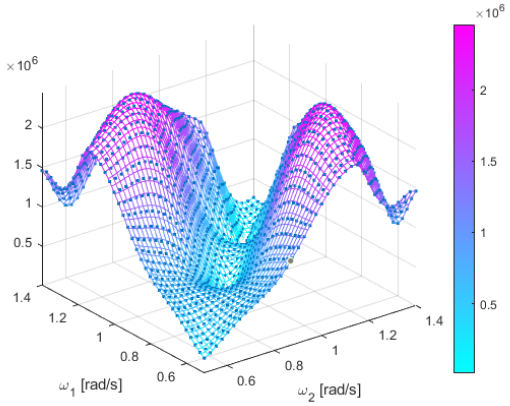

(e) Pitch with inclinations

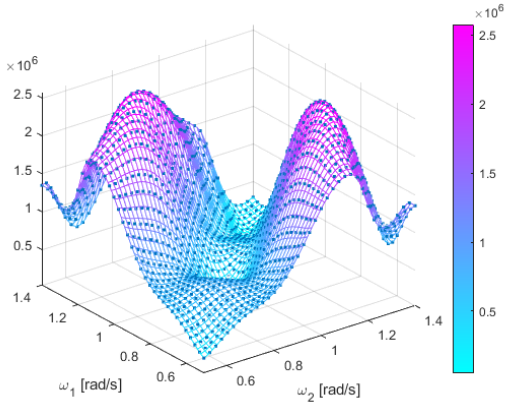

(f) Pitch without inclinations

Figure 8.5: Wave force difference frequency QTF surface diagram comparison

8.3 Motion Response Analysis

This section presents the motion response time series from the coupled time-domain analyses performed in SIMA. In this case the dynamic behavior of the damage cases is studied when subjected to different environmental conditions. Considering the first and third damage cases being less severe instances of the damages displayed in the second and fourth damage cases, their individual time series are included with the others in the Appendix G in Figures G.20-G.39. The floater is symmetric, and the incoming wind and waves are in the same direction. By this, the focus is on the surge and pitch direction, as these are the most critical in terms of the incoming wind and wave direction. The main focus of this study is the investigation of the difference in the floater response when subjected to different damage cases under several sets of environmental conditions.

The results displayed are as mentioned neglecting the transient condition of the collision causing the damage, but also the filling of the compartments. In this case, the possible sloshing within the compartments is also ignored, in which may lead to an even larger stability issue. This issue may be investigated by the use of computational fluid dynamics, in which is not performed within this study. Another limitation discussed previously is the modification of the Morison coefficient due to the damage facing the waves and current in damage case 1 and 2. This is another issue in which should be investigated further.

8.3.1 Environmental Load Case - LC1

The first load case presents typical operational environmental conditions. For these simulations, the turbine is kept operational for the whole simulation. The simulations are performed for a duration of 1 hour, including an additional 400s to account for the initial transient start-up. The results presented in Table 8.1 are the averaged results from a set of 15 conditions with different wave seeds. The individual time series of the simulations are presented in Appendix G, while the comparison of the time series for the intact configuration, damage case 2 and damage case 4 is presented in Figure 8.6. As an addition, the comparison of the power spectral density is included in Figure 8.7. All simulations are performed using the hydrodynamic results presented earlier, including the full QTFs for all conditions. The focus comes in the form of looking closer at the motion response of the different damage cases with respect to the influence of different aero- and hydrodynamic loading.

Looking closer at Figure 8.6 together with Table 8.1, one may notice that the second damage case experiences a significantly larger response in the surge direction. The mean value of the surge response is of about 19.46% increase. A factor that's likely to come into play with regards the surge response is the pretension of the mooring configuration. For these cases, this pretension is the same, and hence, eliminates this factor. The second and fourth load case have one significant difference, and that is the center of buoyancy. As observed in Figure 8.6, the pitching offset of damage case 2 is of large difference in relation to the intact condition. This inclination causes the submerged part of the substructure to expose a larger fraction of submerged frontal

area. In return, this leaves us with increased forces acting on the structure, and hence, an increased surge offset. In addition to this, the pitching angle would lead to reduced horizontal tension in mooring line ML1 for the second damage case, which would allow for a further increase in the surge offset. One may notice this effect in the standard deviation of the configurations, in which damage case 2 experiences a larger variation. Comparing the intact condition with the fourth damage case, one may notice very small differences. This occurs due to the fact that the differences appearing between the two configurations being located in the perpendicular plane to the wind, waves and current. Despite this, one may notice slight deviations from the intact condition.

Looking closer at the pitching of the turbines, one may notice even larger differences. Here, the difference in mean pitch angles between the intact configuration and the second damage case is of 9.77°. For the standard deviation, these configurations experience a difference of almost 22%. Between the intact configuration and the fourth damage case smaller differences are observed in which an interesting addition to the results would be displaying the same results when the wind and wave propagation direction is in sway. In this case, the fourth damage case would also show some larger differences from the intact condition. From the frequency domain analyses, ignoring the upper layer of damage compartments was decided on due to the small difference in static inclinations for the damage cases in regards to the intact condition. Looking closer at the time-series of the pitch offset for damage case 2, one may notice pitching of up to 7.5°. Considering the damage is located about 45m from the CoG, this would lead to a submersion of up to 5.9m. Not only is this significant enough to consider the upper layer of the damage compartments, and hence, increased severity of damage, but it's also significant enough for transient effects such as sloshing to appear. Another important effect to consider is the severity of damage case 2 if the wind-, wave-, and current direction were reversed. Under operational operating parameters such as these, it may well lead to capsize.

Load case 1						
	Intact		**Dmg 2**		**Dmg 4**	
	Surge [m]	Pitch [Deg]	Surge [m]	Pitch [Deg]	Surge [m]	Pitch [Deg]
Mean	-14.10	-4.80	-17.14	4.97	-14.23	-4.72
STD	1.26	0.82	1.30	1.02	1.28	0.77

Table 8.1: Average results of mean and standard deviation values of platform motions for LC1 from 15 realizations with different wave seeds, t = 2000-3500s

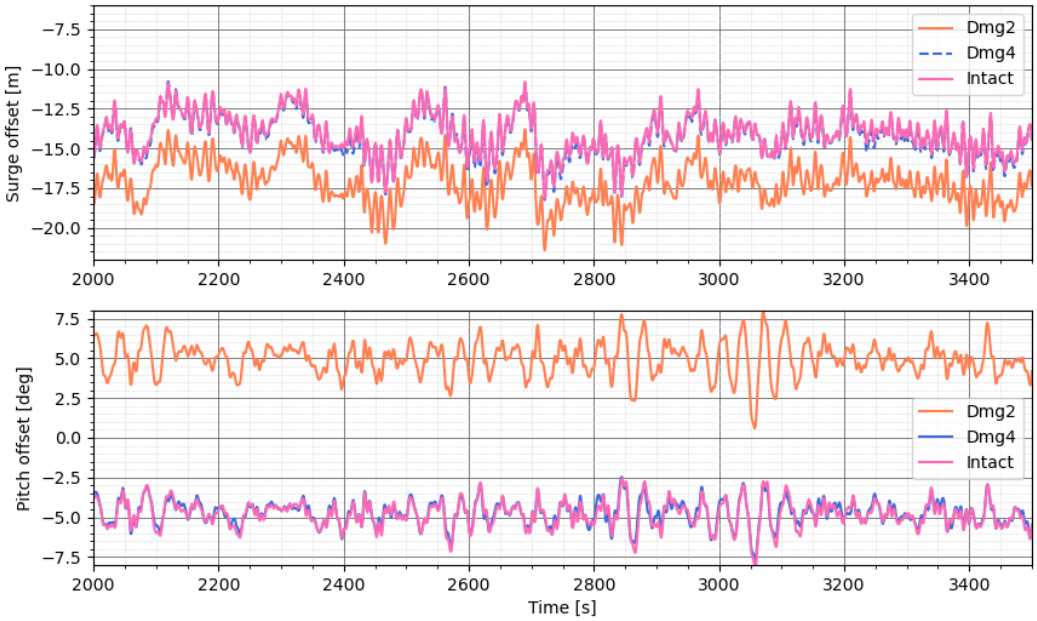

Figure 8.6: Response time series comparison - LC1

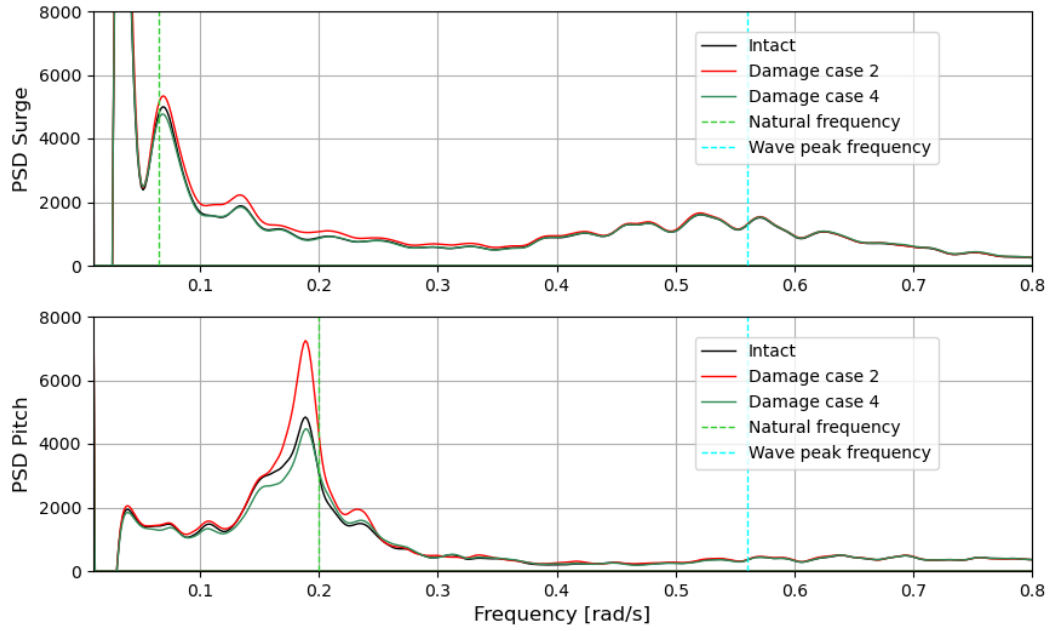

Figure 8.7: Power Spectral Density comparison - LC1

8.3.2 Environmental Load Case - LC2

The second load case is of similar environmental parameters as the first. The difference comes in the wave parameters, in which the significant wave height and the spectral peak period are increased. This way, its possible to look closer into the dependency on the wave forces for the different damage cases. For these simulations, the turbine is kept operational, and the same parameters are applied. The individual response time series are presented in Appendix G, while the comparisons of the intact condition, the second damage case and the fourth damage case is presented in Figure 8.8. The averaged results for all 15 seeds are presented by the mean and standard deviation values in Table 8.2. The comparison of the power spectral densities are presented in Figure 8.9.

For the mean surge offset, one may notice an increase of about 4.37% from the first environmental load case for the intact condition. For the second damage case, this increase is of only 3.95%. The fourth damage case follows the trend of the intact condition, in which reduces the gap in mean surge offsets between all the substructure configurations. As these results depend on several factors, including the phase of the wave, it is hard to justify exactly why the surge response converges between the different configurations. One theory resides in the reduced Morrison coefficient for damage case 2, and the fact that the hydrodynamic loads of this environmental load case is of increased importance. In regards to the mean pitch offsets, the changes between the first and second environmental conditions is minimal. This highlights the dominance of the wind loads and the buoyancy in terms of the mean pitching angles. Despite the small change, one may notice a larger variation in mean pitch angles for the intact condition between the environmental load cases.

In terms of the comparison of the different loading configurations for this environmental load case, one may notice that the difference in mean values in surge between the intact configuration and the second damage case is of about a 19% difference. This is a small reduction in regards to LC1, but as mentioned, a small difference. In regards to the standard deviations of these offsets, one may notice a difference of about 3%. The fourth damage case is still relatively close to the intact configuration in terms of both mean surge offset, but also the standard deviation.

For the pitch offset, one may notice a difference in mean pitch angles between the intact configuration and the second damage case of 9.76°. Here, the standard deviation experiences a 23.6% difference. Looking closer at this difference, one may draw a conclusion as this small increase in wave parameters increase the difference in standard deviation by almost 2%. From these results, one may highlight the convergence of the mean surge response for the different loading configurations for increased wave loads. One may also conclude with an increase in standard deviation in pitch of the second damage case due to the increase in wave loads. In terms of the fourth damage case, it would be interesting to look closer at the results for different environmental heading angles, considering the marginal differences with respect to the intact configuration.

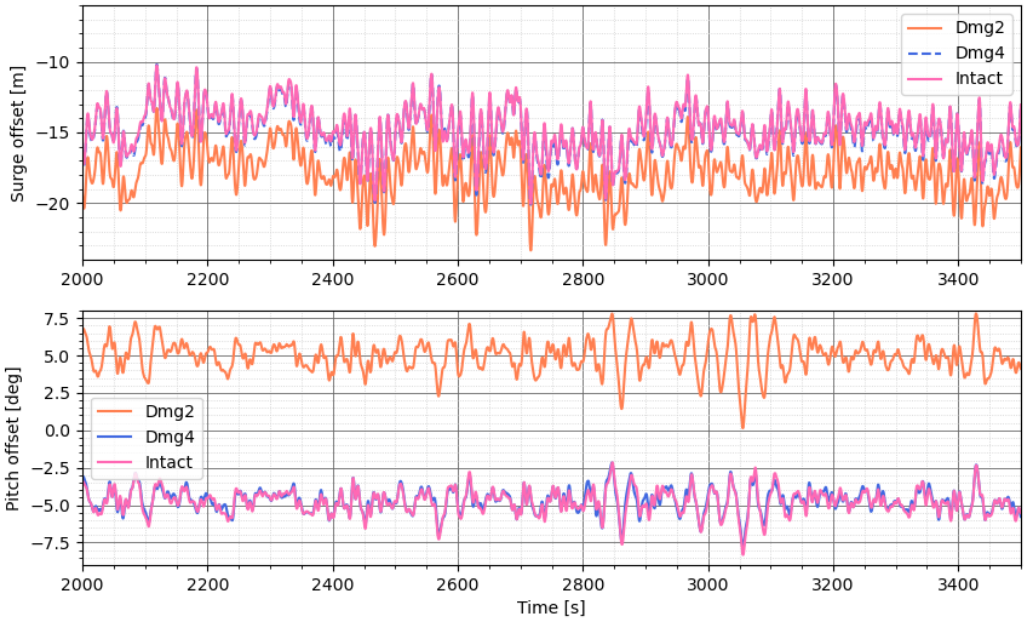

Figure 8.8: Response time series comparison - LC2

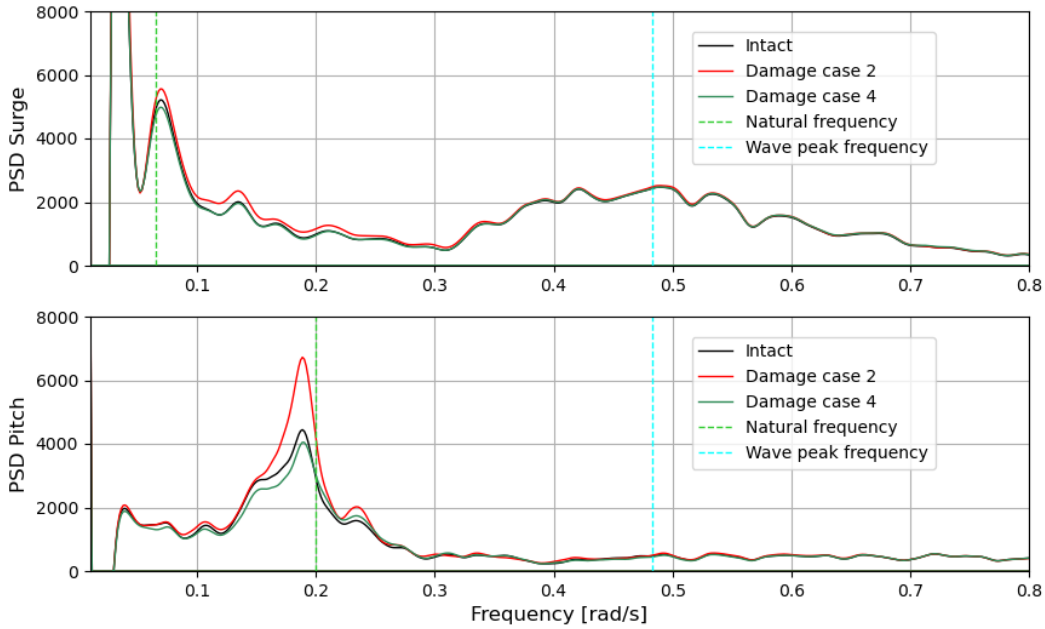

Figure 8.9: Power Spectral Density comparison - LC2

Load case 2						
	Intact		**Dmg 2**		**Dmg 4**	
	Surge [m]	Pitch [Deg]	Surge [m]	Pitch [Deg]	Surge [m]	Pitch [Deg]
Mean	-14.73	-4.76	-17.83	5.00	-14.87	-4.69
STD	1.58	0.82	1.63	1.04	1.60	0.78

Table 8.2: Average results of mean and standard deviation values for LC2 from 15 realizations with different wave seeds, t = 2000-3500s

8.3.3 Environmental Load Case - LC3

The third set of environmental conditions are of extreme state for all parameters. For these simulations, the turbine is parked for the whole simulation. The applied simulation length is of a duration of 1 hour, including the additional start-up interval of 400s. The individual time-series for the different configurations are presented in Appendix G. In addition, the dynamic behavior of the different configurations is compared by the means of a time-series of the response in surge and heave in Figure 8.10 while the average of the statistics for the 15 realization with different wave seeds is presented in Table 8.3. The comparison of the power spectral densities are presented in Figure 8.12.

For the mean surge response, one may notice severe differences compared to previous environmental load cases. This seems to be due to the lacking effect of the wind loads, and is to be expected considering the fact that the wind turbines are in parked condition. One interesting factor here is displayed by the difference in mean surge response between the intact condition and damage case 4. For previous environmental load cases these have been close to identical, but here, one may notice a difference of about 5.3%. In addition to this, the difference between the intact configuration and damage case 4 is of only 2.6%. From this, one may arrive at the conclusion that the large wave forces neutralizes the differences between the two configurations in which appear in the symmetrical plane. In addition to this, it seems to be less capable of neutralizing the differences in the perpendicular plane. In terms of the standard deviation, the most critical variations are observed for the intact configuration. Comparing the intact condition with the fourth load case, one may arrive at the conclusion that the difference in mean surge offset results in a larger horizontal tension for the fourth damage case, and hence, a smaller variation in offsets.

For the pitch results, one may investigate the phenomena closer. For these results, one may also notice the mean values for the intact configuration and damage case 4 increasing at different rates compared to previous environmental load cases. This opened up some new theories about why. It was therefore decided to look closer at the other degrees of freedom for clarification purposes. In Figure 8.11, the sway and yaw time series for the first seed are displayed respectively. From this, one may notice a significant decrease in the sway offset and an increasing yaw offset for the fourth damage case compared to the intact configuration. These additional displacements would also lead to a coupled horizontal tension from two mooring lines, resisting the offsets in both surge and pitch. Looking closer at the environmental forces could be interesting for the confirmation of this event for the other environmental load cases.

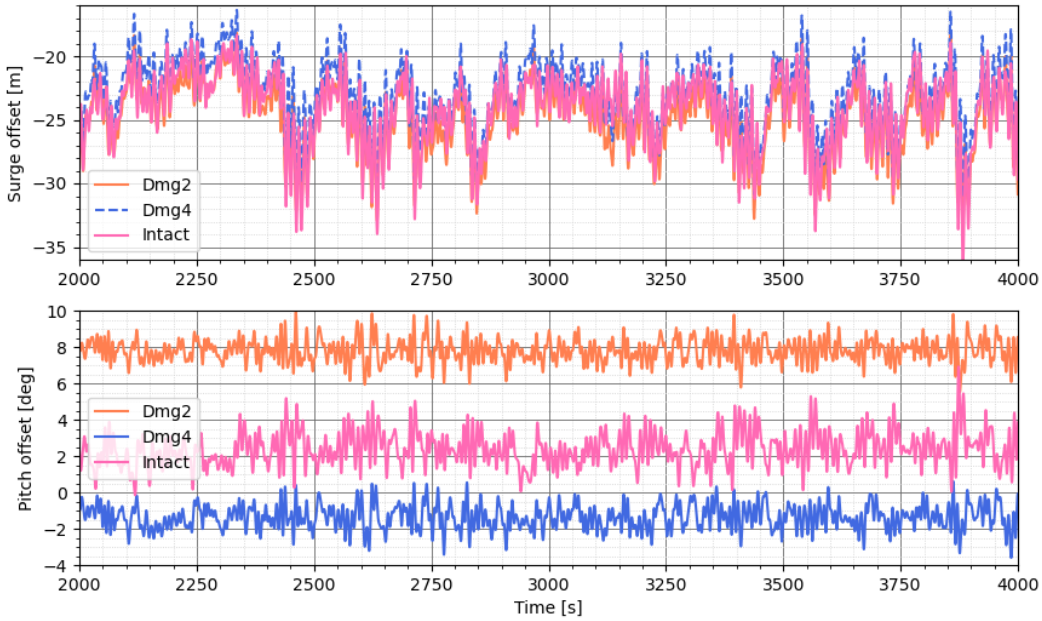

Figure 8.10: Response time series comparison - LC3

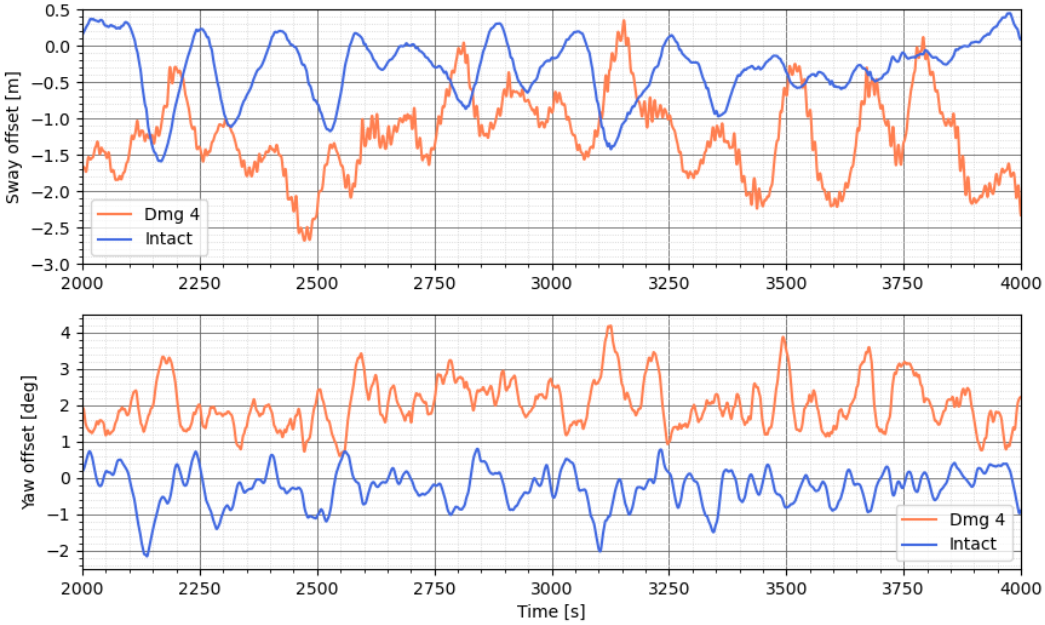

Figure 8.11: Sway time series comparison - LC3

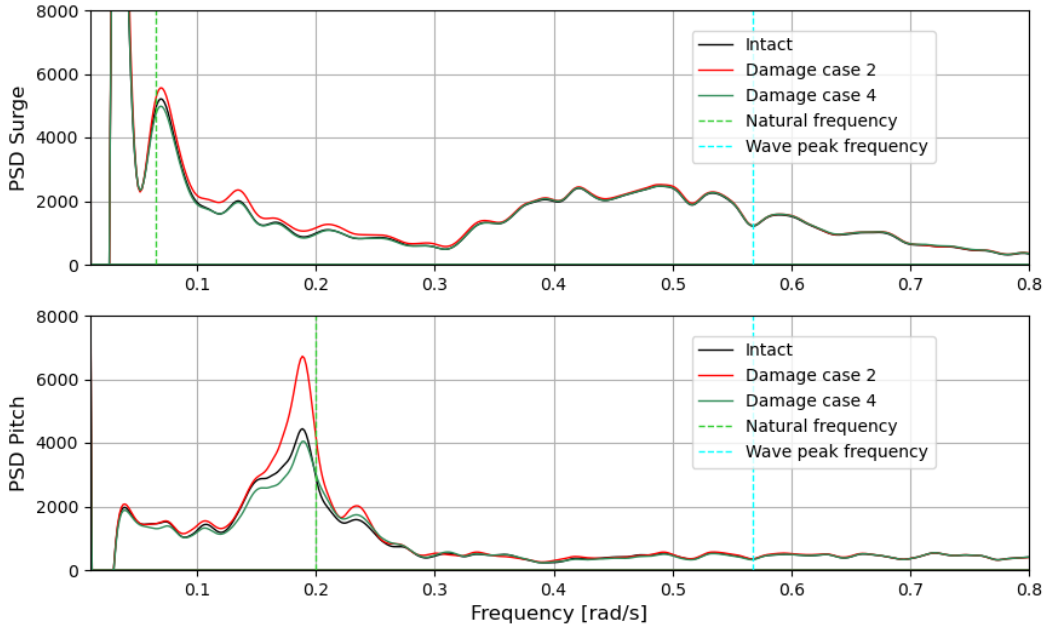

Figure 8.12: Power Spectral Density comparison - LC3

Load case 3						
	Intact		**Dmg 2**		**Dmg 4**	
	Surge [m]	Pitch [Deg]	Surge [m]	Pitch [Deg]	Surge [m]	Pitch [Deg]
Mean	-23.96	2.29	-24.60	7.79	-22.72	-1.36
STD	2.70	0.89	2.63	0.63	2.57	0.67

Table 8.3: Average results of mean and standard deviation values for LC3 from 15 realizations with different wave seeds, t = 2000-3500s

8.4 Emergency Shutdown - LC4

In the event of damages as discussed previously in this thesis, it may be necessary to shut down the turbine to prevent further damage or safety hazards. Emergency shutdown procedures are designed to quickly and safely stop the turbine in the event of a malfunction or damage. These procedures are typically activated automatically by the turbine's control system or manually by an operator on a control panel. The shutdown sequence may involve stopping the rotation of the blades, stopping the generator, or disconnecting the turbine from the power grid. In this section, the shutdown process is analyzed by the means of time-domain analyses by stopping the rotation of the turbine blades during the simulation. In this context, the severity of this procedure is to be looked further into, in regards to the safety of the operation for both the intact, and damaged conditions.

For the comparison of the emergency shutdown procedure for the different configurations, 1-hour simulations were performed with environmental condition corresponding to those of the second environmental load case. For these simulations, the emergency shutdown of the turbine is initiated at t = 1000s. The results from these simulations are presented by the means of individual response time series in surge and pitch in Appendix G, comparisons of the response time series in Figure 8.13, averages of the statistics for the 15 different realizations based on different wave seeds in Table 8.4, and calculations of the maximum axial acceleration at the nacelle in Table 8.5. In design of FOWTs, the axial acceleration at the nacelle is set to an operational limit, normally in the range 0.2-0.3g which is related to the safety of wind turbine components (R. Nejad et al., 2016). As a safety aspect, this would be a relevant factor to consider for potential emergency shutdowns, in regards to the overall safety of the operation. The main goal of this section is the investigation of potential differences in the loading configurations with respect to the event of an emergency shutdown. It is also of interest to look closer into the relations between the different instances of the process. The maxima of the responses are also of interest considering the mooring system, but also the possibilities of capsize.

During the shutdown process, one may notice a sudden decrease in the mean surge offset for all loading conditions. For the intact configuration and the fourth damage case, these reductions are of approximately 26%, while the reduction for the fourth damage case is smaller and at about 24%. The standard deviation of the surge motion is of interest when comparing the intact configuration to the fourth damage case, as one may notice a larger instability for the fourth damage case. For the second damage case, this instability is more severe, and it is about 10.95% larger than for the intact configuration. In regards to the pitch motions of the configurations, one may notice different rates of increase of the mean values. The mean pitch angle change due to the shutdown process is the most severe for the intact condition. Despite this, one should account for the large standard deviation of this motion in the second damage case which displays the instability of the motion for this damage case. An interesting factor to consider for this case is the maximum pitch angle. Looking at the second damage case in particular, one may notice a max pitch angle of 15.3° which is quite severe, and something that could lead to extreme tension in the mooring system.

After the shutdown process, one may see an even further decrease in the mean surge offset for all conditions. The most severe change in mean surge offset is observed for the fourth damage case, in which reduces by 28.4%, while the second damage case and the intact configuration reduces by 21.7% and 23.94% respectively. Despite decreasing the mean motion in surge, this would increase the tension on the mooring lines, and hence, it's hard to conclude whether it is positive or not. In terms of the standard deviation, the damage cases experiences smaller values compared to the intact configuration, signifying smaller changes in the motions. In terms of the pitching motion, one may notice the mean values for all configurations reducing. In addition to this, one may notice the fact that the standard deviation of all configurations are lower than both before emergency shutdown and during the shutdown process. This makes sense, considering the reduced thrust force. In many ways one could compare the statistical values of the motions before and after shutdown and conclude that the mean motions after shutdowns are severely lowered. From a safety aspect on the other hand, one should consider several additional factors such as the process of shutting down, in which the motions are severely increased.

Another factor to take into account is the maximum axial acceleration at the nacelle, and whether this may damage the wind turbine components. According to sources, a typical operational limit for this acceleration is in the range of 0.2-0.3g. In Table 8.5, the maximum axial acceleration at the nacelle for environmental load case 2 and the emergency shutdowns are documented. Here, one may observe one of the other reasons of why one doesn't perform an emergency shutdown unless it's necessary. For the intact configuration, the maximum axial acceleration increases by 44.5%, for damage case 2 it increases by 53.3%, and for damage case 4 it increases by 62.8%. One may notice that the damage cases experiences larger variation due to the emergency shutdown. One of the several reasons this may be, is due to the difficulty of finding the equilibrium. Despite the severe increases, all of the cases exceeds the typical operational limits, including environmental load case 2. For this part, it should be mentioned that the environmental parameters present in environmental load case 2 are well above typical operational parameters.

This study highlights the advanced decisions that are to be made in regards to the safety of the operation of these FOWTs. Unfortunately, the numbers are lacking in terms of an overall safety evaluation of the operation. If one is to do this, more advanced information on the mooring forces, anchor forces, sloshing resonance, fatigue limits have to be included. Despite this, the results documents some of the pros and cons in regards to emergency shutdowns. A takeaway point for further research from this section, would be the investigation of the tension in the mooring lines if the wind and waves appeared from the opposite direction for the second damage case. This might very well case the turbine to capsize.

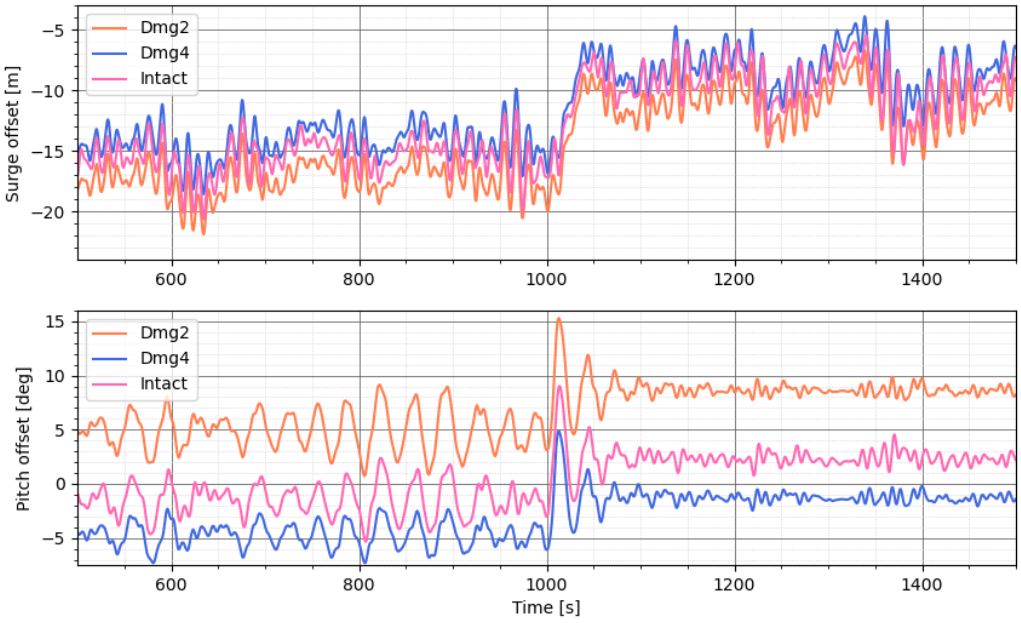

Figure 8.13: Emergency time series comparison

Emergency shutdown - before shutdown (t = 500-1000s)						
	Intact		**Dmg 2**		**Dmg 4**	
	Surge [m]	Pitch [Deg]	Surge [m]	Pitch [Deg]	Surge [m]	Pitch [Deg]
Mean	-15.56	-1.46	-17.33	4.96	-14.29	-4.70
STD	1.54	1.50	1.45	1.79	1.42	1.13
Max	-20.64	2.37	-21.91	9.15	-18.59	-2.25

Emergency shutdown - during shutdown (t = 1000-1050s)						
	Intact		**Dmg 2**		**Dmg 4**	
	Surge [m]	Pitch [Deg]	Surge [m]	Pitch [Deg]	Surge [m]	Pitch [Deg]
Mean	-11.97	2.77	-13.75	9.05	-10.98	-0.79
STD	3.28	3.38	3.66	3.54	3.44	3.09
Max	-17.23	9.02	-20.01	15.30	-16.86	4.85

Emergency shutdown - after shutdown (t = 1100-1500s)						
	Intact		**Dmg 2**		**Dmg 4**	
	Surge [m]	Pitch [Deg]	Surge [m]	Pitch [Deg]	Surge [m]	Pitch [Deg]
Mean	-9.41	2.33	-11.05	8.64	-8.25	-1.29
STD	2.07	0.55	1.88	0.40	1.83	0.39
Max	-16.16	4.55	-16.15	9.87	-12.99	-0.22

Table 8.4: Average results of mean and standard deviation values for emergency shutdown from 15 realizations with different wave seeds

Env load case	Intact [g]	Dmg 2 [g]	Dmg 4 [g]
Emergency	3.24	3.80	3.68
LC2	2.06	2.20	1.92

Table 8.5: Average maximum axial acceleration at the nacelle from 15 realizations with different wave seeds

8.5 Effect of Inclinations in Time-domain Simulations

This section presents the time-domain simulations for environmental load case 1 by the use of the frequency-domain results from HydroD displayed in Section 8.2. The results are generated by the means of frequency-domain analyses both with and without applied inclinations due to damage in compartments. The damage case presented is the second one, in which damage occurs in parallel plane to the wind and wave directions. The results in this section are performed by the inclusion of the full QTFs of both cases. In order to highlight possible differences in the dynamic behavior, the time-series of the analyses are included in Figure 8.14. In addition, the mean and standard deviation averages from 15 wave seeds are included in Table 8.6.

From Table 8.6, one may observe the statistics from both configurations. Based on previously performed frequency-domain analyses, the increase in the mean surge response is expected for the configuration without the applied inclinations. If one were to run the same analysis but by applying lower wave periods, the mean surge motion from the condition with the applied inclinations would be larger. As expected, this shows the dominance of the wave forces in this DOF. There is also a 7.17% increase in the standard deviation of the simulation without the applied inclination. This may be explained by a reduction in the hydrostatic restoring coefficients.

In regards to the pitch offsets, one may notice a small reduction in the mean value for the configuration without the applied inclinations. As this motion is largely affected by the aerodynamic forces, smaller changes was expected. This resides in the same environmental wind model being applied for the same wind turbine model for both simulations. If one were to base assumptions solely on the performed frequency-domain analysis, larger changes in the pitch motions would have been expected. The presence of the operating wind turbine seems to have reduced these differences significantly. One may still notice an increase in the standard deviation of 3.85% highlighting the difference in the behaviors of the two configurations.

Despite the changes in statistics, the configuration without the applied inclinations seems to be capturing the dynamic behavior of the damage case in quite a good manner. It should be mentioned that the difference in trim angles from the frequency-domain analyses were of about 4°, in which isn't very significant. From the literature review, some comments are made regarding potential flow methods' ability of capturing effects of static pitch. From an experimental point of view, it may be interesting to re-do the analyses in the same manner, but by the use of CFD methods. The comparison of these results might bring even further insight into the analysis of applied static inclinations of semi-submersible structures. In terms of the validity of the frequency-domain analyses performed without applying the correct static inclinations, the results highlight the importance of performing the analyses in a correct manner. Despite the reduced computational cost for the cases without the applied inclinations, the results are lacking. For these simulations, the difference between the trim angle of the configurations was about 4° which is minimal. Despite this, the results displayed show considerable differences in statistics despite the similar dynamic behavior.

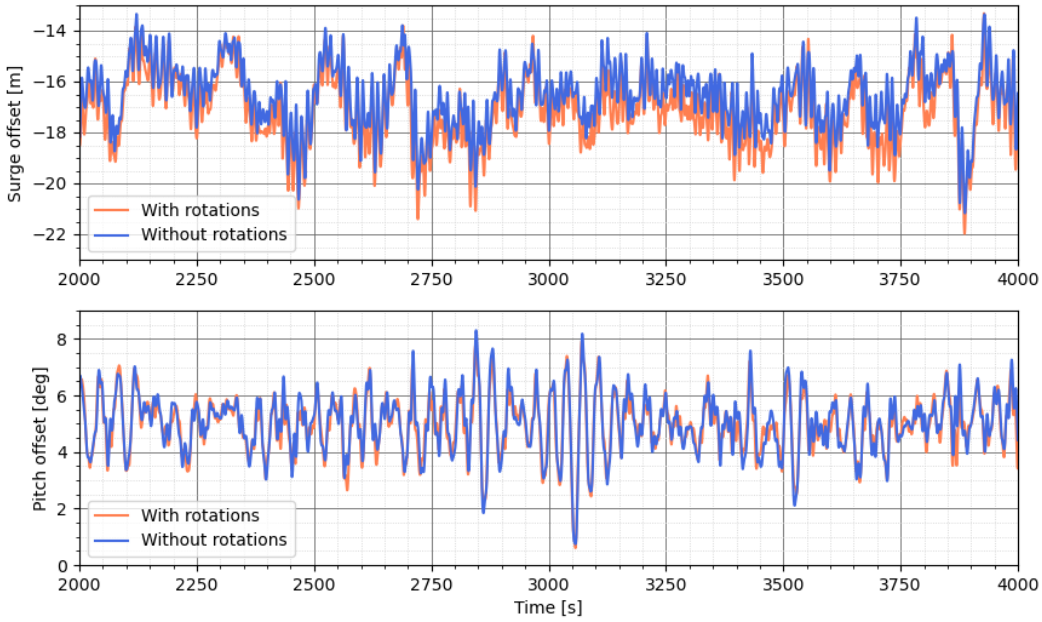

Figure 8.14: With and without applied inclinations comparison

Inclination comparison						
	With inclinations		**Without inclinations**		**Deviation**	
	Surge [m]	Pitch [Deg]	Surge [m]	Pitch [Deg]	Surge [%]	Pitch [%]
Mean	-16.52	5.02	-17.14	4.97	3.68	1.00
STD	1.21	1.06	1.30	1.02	7.17	3.85

Table 8.6: Mean and standard deviation values for comparison with and without applied inclinations, t = 2000-3500s

8.6 Environmental Loads

This section presents the environmental load results present for some of the performed time-domain simulations. The objective of this section is to look closer at the differences with regards to both the environmental load cases, but also the differences in relation to the loading configurations. One of the interesting aspects to investigate in this case is the differences between the second and fourth damage cases considering their difference in motions. The results presented in this section are averages from 15 realizations which are based on different wave seeds.

8.6.1 Hydrodynamic Loads

For the hydrodynamic loads, the environmental load cases of interest were decided to be LC 1 and LC 2, due to their similarities in wind and current. The results are presented in Table 8.7 by the means of standard deviations of the first-order forces, and the QTF forces. The results present are the surge, heave and pitch forces due to the direction of the wind and waves.

For environmental load case 1, increased wave forces are to be expected for the second damage case due to the increased mean displacement in surge. Looking at the table of results, this isn't the case. As seen, the fourth damage case experiences the highest first-order wave loads in surge. In comparison to the intact condition, one may notice about an 8.8% increase in the standard deviation of the surge forces for both damage cases. The resulting decreased motion of the fourth damage case may be explained by the coupled resistance in two mooring lines due to the displacements in sway and yaw. Looking closer at the second environmental load case one may notice an expected increase in hydrodynamic forces. These come as a result of an increase in significant wave-height. In terms of the increase, one may notice that the forces resulting from the QTFs increase at a higher rate due to the change in environmental conditions. Here, the first order forces increase by about 25% for the damage cases and 28% for the intact condition, while the QTF forces increase by about 37% for all conditions. Overall, the outcome of the standard deviations for the second environmental load case are similar to those of the first. Despite this, the forces on the intact loading condition seems to approach similar forces to the damage conditions for increased significant wave-heights. This was touched upon earlier in Section 8.3.2 in which the mean surge offset of both the intact condition and the fourth damage case approached similar mean displacements as the second one.

In terms of the hydrodynamic forces in heave direction, the intact condition seems to experience the larger forces. This is quite unexpected, and it seems to be connected to the change in hydrostatic restoring coefficients in which is not discussed in this thesis. For the comparison between the damage cases, one may notice a slight increase in the hydrodynamic forces for the fourth damage case. This was to be expected from previous frequency-domain results. Comparing the changes between the first and second environmental load case, one may observe a similar phenomena to what's already seen for the surge forces. The full QTF forces experience a larger

increase due to the significant wave height increasing. The difference coming in the form of a further increase in forces. In terms of the first-order forces, this increase is reduced compared to the surge forces. This increase is of 20.4%, 20.6% and 20.36% for the first-order forces for the intact condition, damage case 2 and 4 respectively. The QTF forces increases by 40.64%, 44.86% and 43.54% in the same order. By this, one may conclude that the INO-WINDMOOR is more sensitive in regards to the first-order wave forces when it comes to increasing wave-heights, while for QTF forces, it seems to be more critical in the heave direction.

For the hydrodynamic forces in pitch, large differences aren't as expected, due to the dominance of the wind forces in this direction. In terms of the comparison of the first-order forces with respect to the load cases, the damage cases experiences about a 5.25% increase with respect to the intact configuration. Here, when it comes to the QTF forces, one may notice the damage cases experiencing increased values. This is especially significant for the second damage case which experiences a 17.7% increase in regards to the intact configuration. In terms of the increase between the environmental load cases, we may see some changes in regards to the other directions. Here, on average, the first-order loads increase by about 13.2%. Here, one may notice the intact configuration increasing by a slight increased percentage than the damage cases. In regards to the QTF forces, one may notice quite the opposite. Here, on average, the increase in forces between the load cases are of about 45.7% increase, but here the damage cases increase by a larger amount.

By these results, one may conclude several points about the loads affecting a design such as the INO-WINDMOOR. One of the larger takeaways from this section is the fact that the fourth damage case experiences similar wave forces to the second damage case despite experiencing such large differences in the mean offsets. Another factor to keep in mind is the increased change in QTF forces for the damaged conditions when increasing the wave height, despite the overall decrease they experience with respect to the intact condition in surge and heave. In pitch on the other hand, they experience increased values for the QTF forces in both environmental load cases. Based on the overall results, it's also clear that damage of the substructure of the INO-WINDMOOR design would case severe increases in surge and pitch first-order forces.

Surge						
	Intact [kN]		**Dmg 2 [kN]**		**Dmg 4 [kN]**	
	First-order	Full QTF	First-order	Full QTF	First-order	Full QTF
LC1	5229.39	332.57	5708.97	270.85	5731.09	265.34
LC2	6954.94	480.96	7362.28	397.02	7405.50	390.72

Heave						
	Intact [kN]		**Dmg 2 [kN]**		**Dmg 4 [kN]**	
	First-order	Full QTF	First-order	Full QTF	First-order	Full QTF
LC1	4602.00	223.62	3974.40	198.07	4068.55	199.09
LC2	5648.42	337.71	4887.25	312.62	4990.83	309.90

Pitch						
	Intact [kNm]		**Dmg 2 [kNm]**		**Dmg 4 [kNm]**	
	First-order	Full QTF	First-order	Full QTF	First-order	Full QTF
LC1	62215.46	3695.60	65087.51	4413.10	65572.32	4248.72
LC2	71594.94	5819.87	73629.59	7018.82	74843.48	6854.23

Table 8.7: Standard deviation of hydrodynamic wave loads

8.6.2 Aerodynamic Loads

In terms of the aerodynamic loads, the environmental load cases of interest were selected to be LC1 and LC3, due to their differences in wind. An issue in regards to this comparison is the state of the turbine which makes it hard to directly compare the results. For environmental load case 3, the turbine is in parked condition, meaning it won't experience any aerodynamic forces acting on the blades. This, in addition to the increase in hydrodynamic forces makes it hard to justify a comparison between the two, considering the many other factors influencing the results. Despite this, the results were generated as an indication of potential differences in the results with regards to the damage cases. The results are presented by the means of standard deviations of the aerodynamic forces acting in the X-direction and the moment acting about the Y-axis. These are presented in Table 8.8.

For the first environmental load case, one may notice some unexpected differences between the intact configuration and the damage cases in terms of the forces in the x-direction. For this, the most severe difference is experienced between the intact configuration and the second damage case. Here, one may see a difference of about 4.78%, while the fourth damage case only deviates by about 2.56%. Based on previous time-series of the offsets, one may notice that the second damage case pitches in the opposite direction to the intact configuration. This is expected to be the main contributing factor to the difference in aerodynamic forces between the two cases. The difference between the fourth damage case and the intact configuration

is harder to justify due to their similar motions. There is a slight decrease in pitch angle for the fourth damage case, but also a reduced standard deviation of the pitching motion. Hence, it's expected that this configuration is better at maintaining maximum efficiency due to not having to adjust to the motions as much. For the third environmental load case, as mentioned, the justification of the results is a bit more tedious. Here, one mainly considers the drag forces on the turbine tower, and hence, the exposed frontal area. For this, based on previous results, it's known that the angle of pitching increases in the order starting from damage case 4, intact configuration and damage case 2 respectively. This brings up an interesting point considering the order of increasing aerodynamic forces being the exact opposite. A direct reason behind this has not been found. In this case, it might just have to do with the fact that the mean pitching offsets reduces the effectiveness of the pitching of the blades, and as a result, the aerodynamic forces acting at the nacelle are increased for increased mean pitch offset of the turbine.

For the pitching moment of the different load cases, smaller changes are to be expected for the operational turbine in environmental load case 1. As the second damage case leans into the wind by a positive mean pitch offset, the aerodynamic pitching moment is expected to be smaller for this configuration. This is also reflected in the results. The fourth damage case is also expected to experience slight reductions in the pitching moment due to the slight offsets experienced in sway and yaw. This may just cause a fraction of the total moment to be transformed into a moment about the x-axis due to these offsets. This is also the case by looking at the results. For the third environmental load case, the results appear increasing by the order of the second damage case, the intact configuration and the fourth damage case. As the increase in pitch offset appear by this order as well, its expected to be the main factor affecting these results.

Overall the results of the aerodynamic forces were of interest in regards to investigating the phenomena of the damage cases, in which overall changes the aerodynamic loads acting. Despite this, having two operational conditions with different wind speeds would have been nice in terms of having a better comparison between environmental load cases.

X-direction			
	Intact [kN]	DMG2 [kN]	DMG4 [kN]
LC1	189.60	198.89	194.52
LC3	18.88	19.17	16.60

Moment about y-axis			
	Intact [kNm]	DMG2 [kNm]	DMG4 [kNm]
LC1	8062.31	8050.22	8036.95
LC3	697.72	289.20	741.84

Table 8.8: Aerodynamic loads standard deviations

8.7 Mooring line forces

In order to establish a more complete picture regarding the behavior of the FOWT, one has to look closer into the axial forces acting through the mooring lines. This section presents the results from the first environmental load case in order to look at differences between the different cases. The objective of the section is to establish a more complete view of the relation between the platform motions, forces, and mooring lines.

The results are presented by the means of mean values and standard deviation of the axial forces which are averaged from 15 realizations using different wave seeds. These results are displayed in Table 8.9. For the motion response, the two damage cases had very different results in both pitch and surge mean values. This difference was reduced significantly when looking closer at the environmental forces on the two damage cases. This led to believing that the change in loading condition somehow led to coupling resisting forces in the mooring lines for the fourth load case, and that this helped in reducing the mean offsets of the motions. Looking closer at the results, one may notice significant differences between the damage cases and the intact configuration. Comparing the intact configuration with the second damage case, one may observe an average difference in 5.10% in the mean axial force for the different mooring lines. Performing the same comparison between the intact configuration and the fourth damage case, one may notice an average difference of about 4.6%. For the standard deviations, one may notice increased standard deviations for both the damage cases with regards to mooring line 1 (ML1). For the other mooring lines, the intact configuration experiences the largest standard deviations. Based on the results, its difficult to formulate a direct conclusion as to the relation between the motions, environmental forces, and the mooring line forces. Despite this, they provide some insight into the increase in tension in the mooring lines due to the damage cases. In order to provide a further idea in regards to the safety aspects of the operations with this increase in tension, a fatigue study should be performed.

Mooring forces (Intact)			
	ML1 [kN]	ML2 [kN]	ML3 [kN]
Mean	3341.84	1814.93	1850.05
STD	295.26	133.75	142.24

Mooring forces (DMG2)			
	ML1 [kN]	ML2 [kN]	ML3 [kN]
Mean	3512.23	1921.26	1938.28
STD	355.13	105.93	113.95

Mooring forces (DMG4)			
	ML1 [kN]	ML2 [kN]	ML3 [kN]
Mean	3495.84	1922.49	1916.50
STD	356.61	103.80	118.31

Table 8.9: Average results of mean and standard deviation values for mooring forces from 15 realizations with different wave seeds - Environmental Load Case 1

9 Discussion of Findings

9.1 Newman's Approximation vs. Full QTF

This section presents the important findings with regards to the application of Newman's approximation in comparison to the full QTFs.

The studies of this concept was performed by the means of frequency-domain analyses. In terms of the overall applicability, it would be interesting to look further into the time-domain applications. Beforehand, investigations regarding the applicability of Newman's approximation were made, and it was found that the approximation was lacking in the non-horizontal DOFs. Therefore, the study for this section was analyzed in the surge direction, but with the addition of one of the damage cases. Comparing the results, the surge force for the intact condition was identical for the Newman's approximation and the full QTF. The results from the damage case concludes the same results, but with different values. In conclusion, with regards to the surge DOF, Newman's approximation seems sufficient in approximating the wave forces for both intact configuration, but also for the damage case with applied static inclinations.

9.2 Applied inclinations for frequency-domain analyses

This Section presents the findings with regards to the studies of the applied inclinations for the frequency-domain analyses. It was noticed that when the substructure's inclination was non-symmetric, the frequency-domain analyses could not be performed using symmetric panel models. This caused the analyses to become more computationally expensive, which is not optimal. To address this issue, the study aimed at investigating whether changes in the substructure's inclination could be neutralized by simulating the model with updated CoG, COB, and mass distribution without the updated inclination.

The analysis was performed for damage case 2, which is one of the most severe damage cases where the damage is located at the front of the substructure. The study focused on the comparisons of the added mass and damping coefficients, force and response transfer functions of the body, and quadratic transfer functions. The results showed that for the main-diagonal coefficients, there were little to no differences between the results with and without the updated inclination. However, the off-diagonal coefficients showed severe changes similar to the documentation in the previous section, suggesting that these changes might affect the results in coupled analyses.

The force and response transfer functions of the body were also studied, and there were only slight deviations in the results, which were small and similar. The quadratic transfer functions were presented, and the results with and without the rotations were almost identical, indicating that this hypothesis should be further investigated in terms of time-domain analyses.

Overall, the study suggests that changes in inclination can be neutralized, making the analyses more efficient. The similarity between the conditions might be due to the design of the substructure, and further investigation is required to validate this hypothesis. The study's findings have important implications for the analysis of non-symmetrically loaded structures, which are common in many engineering applications. The study's methodology can be applied to other substructure designs, and the results can be used to optimize the analyses and reduce the computational cost.

9.3 Motion Response of Damaged Substructure

This section presents the major findings from the studies of motion response of the damage conditions for different environmental load cases.

The main goal of this study was focused around the comparison of the motion response of the FOWT subjected to different damage cases and different sets of environmental conditions. The study of the dynamic behavior was of significance, but one should be aware of the limitations of this study. The neglecting of the transient conditions of the collisions causing the damage, the filling process of the compartments, and the possible sloshing within the compartments are all important factors in which could improve the study. It is seen that the effects of sloshing could impact the motion response significantly, and the likelihood of the occurrence of this phenomena is looked closer into. The modification of the Morrison coefficient due to the damage facing the waves and current in damage case 1 and 2 is another issue requiring further investigation by the means of CFD.

In terms of the highlights of the first load case, one may notice the second damage case experiencing an increase of the mean response in the surge direction of about 19.46%, while the fourth damage case shows only small differences compared to the intact condition. One possible explanation for the increased surge offset in the second damage case is the pitching offset of the turbine, which causes the submerged part of the substructure to expose a larger fraction of submerged frontal area, leading to increased forces acting on the structure. In addition, the pitching angle would lead to reduced horizontal tension in the mooring line for the second damage case, allowing for a further increase in the surge offset. Looking closer at the pitching of the turbines, there are significant differences between the intact configuration and the second damage case, with a difference in mean pitch angles of 9.77°. The standard deviation also shows a difference of almost 22% between these configurations. An important consideration regarding the pitching of damage case 2 is the fact that it may well lead to a submersion of up to 5.9m of the damage location. This in addition to the large standard deviations makes the importance of considering the possibilities of sloshing significant. The studies also highlights the importance of considering the severity of the damage case if the wind-, wave-, and current direction were reversed. Under operational operating parameters such as these, it may well lead to capsize due to the severe differences in pitching angles caused by a change in center of buoyancy.

The second environmental load case investigated in this study explores the depend-

ency on wave forces for the different damage cases. The key difference between the first and second load cases is an increase in the significant wave height and the spectral peak period. The mean surge offset increases by about 4.37% for the intact condition from the first environmental load case to the second. However, for the second damage case, this increase is only 3.95%. The fourth damage case follows the trend of the intact condition, which reduces the gap in mean surge offsets between all the substructure configurations. One theory for the convergence of the surge response between the different configurations resides in the reduced Morrison coefficient for damage case 2 and the increased importance of hydrodynamic loads for this environmental load case. In terms of mean pitch offsets, there is minimal change between the first and second environmental conditions, highlighting the dominance of wind loads and buoyancy in terms of mean pitching angles. Concluding the findings from this environmental load case, the highlight lies in the convergence of the mean surge response for increased wave loads, but it is proposed to look closer at different environmental heading angles for the fourth damage case considering the marginal differences with respect to the intact configuration.

The third environmental load case was of extreme environmental conditions, in which the turbine was parked for the whole 1 hour simulation. The mean surge response showed severe differences compared to previous environmental load cases, mainly due to the severe increases in drag loads. For this load case, interesting differences between the intact configuration and damage case 4 surfaced. Here, the difference in mean surge response between the intact condition and damage case 4 was about 5.3%, which is higher than for previous load cases. The large wind and wave forces seemed to neutralize some of the differences between the intact configuration and damage case 2 in the symmetrical plane, but proved less capable of neutralizing the differences between the intact configuration and damage case 4 in the perpendicular plane. The intact configuration showed the most critical variations in terms of standard deviation. The sway offset significantly decreased, and the yaw offset increased for the fourth damage case compared to the intact configuration. These additional displacements would also lead to a coupled horizontal tension from two mooring lines, resisting the offsets in both surge and pitch. It's also suggested to look closer at the environmental forces for the confirmation of these events for other environmental load cases.

9.4 Emergency Shutdown of Damaged FOWTs

This section presents the findings with respect to the emergency shutdowns of the damaged FOWTs.

The main goal of this section was the investigation of the dynamic behavior of the different loading configurations under the process of emergency shutdown. This was performed to look closer at the severity of this procedure in regards to the safety of operation for all loading conditions.

The analysis shows that during the shutdown process, there is a sudden decrease in the mean surge offset for all loading conditions. The most severe change in the mean surge offset is observed for the fourth damage case. The standard deviation

of the surge motion is larger for the damaged cases, with the second damage case experiencing the largest instability. The mean pitch angle change due to the shutdown process is the most severe for the intact condition, while the second damage case displays the instability of the motion, with a maximum pitch angle of 15.3°.

After the shutdown process, there is a further decrease in the mean surge offset for all conditions. The most severe change in the mean surge offset is observed for the fourth damage case with a reduction of 28.4%, while the second damage case and the intact configuration reduce by 21.7% and 23.94% respectively. However, this may reduce the tension on the mooring lines, making it difficult to conclude whether this is a positive outcome. In terms of the pitching motion, the mean values for all configurations reduce, and the standard deviation of all configurations is lower than before and during the shutdown process.

In conclusion, several other factors should be investigated in order to form a complete view of the safety of the operation. One of these is considered for the shutdown process, and that is the maximum axial acceleration at the nacelle. For this, the damage cases experiences increases 17.28% and 13.58% for damage case 2 and 4 respectively. This comes to question in regards to safety of the wind turbine components, and shouldn't be treated lightly. Overall, the studies concludes that while the mean motions after shutdowns are severely lowered, additional factors such as the increased motions during the shutdown process, the maximum axial acceleration at the nacelle, the tension in the mooring lines and potential fatigue damage all have to be considered in order to make a proper evaluation of the safety of the procedure. Despite this, one may conclude that the second environmental load case poses threats to the safety of the turbine components due to the large accelerations in all conditions.

9.5 Applied Inclination for Time-domain Analyses

This section provides the main findings from the time-domain simulations of environmental load case 1 with and without applied inclinations due to damage in compartments, using the frequency-domain results from HydroD. The damage case presented is the second one, where damage occurs in a parallel plane to the wind and wave directions.

The increase in the mean surge response is expected for the configuration without the applied inclinations, based on previously performed frequency-domain analyses. There is also a 7.17% increase in the standard deviation of the simulation without the applied inclination, which may be explained by a reduction in the hydrostatic restoring coefficients. In terms of pitch offsets, there is a small reduction in the mean value for the configuration without the applied inclinations. The presence of the operating wind turbine seems to have reduced these differences significantly due to the dominance of the aerodynamic forces. However, there is still an increase in the standard deviation of 3.85%, highlighting the difference in the behaviors of the two configurations.

Despite the changes in statistics, the configuration without the applied rotations

seems to be capturing the dynamic behavior of the damage case quite well. It is mentioned that the difference in trim angles from the frequency-domain analyses was about 4°, which is not very significant. In fact, literature study performed throughout the thesis suggests that CFD is better at capturing the effects of applied static inclinations. Therefore, it's concluded that it may be interesting to re-do the analyses using CFD methods.

The results highlight the importance of performing the analyses in a correct manner, despite the reduced computational cost for the cases without the applied inclinations. The difference between the trim angle of the configurations was about 4°, which is minimal. However, the results displayed show considerable differences in statistics despite the similar dynamic behavior.

9.6 Environmental Forces on Damaged Turbines

This section presents the major findings regarding the environmental loads affecting the FOWT structure for different environmental load cases.

For this study, the investigation of the hydrodynamic and aerodynamic loads were investigated separately, in order to highlight each effects. The study aims to analyze the differences between environmental load cases and loading configurations, focusing on the second and fourth damage cases' differences.

A noteworthy discovery from the study regards the hydrodynamic forces in surge, as a consequence of significant discrepancies in offsets documented in earlier sections. Surprisingly, it's found that the fourth damage case experiences the largest first-order loads, despite experiencing lower mean surge offsets. The forces of both damage case are of about an 8.8% increase with respect to the intact configuration. For the full QTF forces, one may notice an opposite order of increase in regards to the first-order forces which is an interesting finding. Additionally, the hypothesis of the reduction in mean surge offset due to coupled resistance of the mooring lines for damage case 4 is confirmed. For the heave forces, differences are captured with regards to the intact configuration. These are assumed to reside within changes in the hydrostatic restoring coefficients. In terms of the hydrodynamic forces in pitch, an increase of about 5.25% is experienced for the damage cases in comparison to the intact configuration. Similarly, the QTF forces experience an increase with regards to the intact configuration, but this increase is larger. In conclusion, its found that for the INO-WINDMOOR design, damage cases of varying significance would experience increased first-order wave forces in surge and pitch, and and full QTF forces in pitch. In addition to this, reductions in the full QTF forces in surge and heave and the first-order forces in heave are observed.

For the second part of investigations in regards to the environmental loads, the aerodynamic loads were of interest, and the load cases of interest were LC1 and LC3 due to their differences in wind. One issue regarding these studies were the difficulty of comparing the load cases due to the turbine's state differing between the two cases. Here, for LC3, the turbine was in parked condition in which the aerodynamic loading on the blades is negligible. For LC1 and the forces in x-direction, the

study observed some unexpected differences between the intact configuration and the damage cases. The second damage case showed the most significant difference with a deviation of about 4.78% compared to the intact configuration. The fourth damage case had a deviation of about 2.56%. The pitching motion of the second damage case in the opposite direction to the intact configuration was identified as the main contributing factor to the difference in aerodynamic forces. However, it was harder to justify the difference between the fourth damage case and the intact configuration due to their similar motions. It was expected that the fourth damage case was better at maintaining maximum efficiency due to not having to adjust to the motions as much. For the third environmental load case, the justification of the results proves more complicated. Here, the main contribution to the x-direction forces are the drag forces on the structure, and hence, exposed frontal area. Here, the opposite is observed. In terms of this observation, a direct reason was not found. In terms of the pitching moments, smaller differences were experienced in the first environmental load case, as expected due to the operational wind turbine. For the third environmental load case, the results appear increasing by the order of the second damage case, the intact configuration and the fourth damage case. The pitching offset appear in the same order, and hence, it's expected to be the main contributing factor in regards to these results.

10 Conclusion and Potential Further Work

10.1 Conclusion

For this thesis, the INO-WINDMOOR floating wind turbine design have been studied under the operation at depths of 250m. The WINDMOOR design consists of the INO-WINDMOOR semi-submersible steel platform, its hybrid catenary mooring system, and the up-scaled version of the IEA 10MW wind turbine called the WINDMOOR 12MW wind turbine. For the thesis, a numerical finite element panel model was constructed together with a compartment model for the definition of damage load cases. By the application of these panel models, first- and second-order frequency domain analyses were carried out for acquiring the hydrodynamic results for the substructure. These hydrodynamic properties were carefully analyzed and compared for the further importation into the SIMA environment. In SIMA, the model containing all the FOWT properties was constructed. Here, the frequency-domain results were imported, the mooring system parameters were defined, the hydrostatic restoring data was defined, the quadratic drag was included, and the turbine was imported together with its components. This model was then applied to further investigate the several conditions in time-domain simulations.

The main aim of this thesis was the investigation of this thesis was the investigation of potential damage conditions of a FOWT during operational conditions. The study consisted of both frequency domain analyses, but also time-domain analyses for selected damage scenarios to be investigated. An additional inclusion to the study was the investigation of possible transient phenomena and wind turbine components safety. The investigations of the damage conditions were performed by comparing the damage cases to the intact configurations. The following steps concludes the investigations based on the results.

- Newman's approximation proved to be a good fit in terms of estimating the full QTF forces in the surge direction. This was also found to be the case for the damage conditions with a corresponding applied static inclination.
- In terms of performing frequency-domain analyses for a damaged structure without applying the proper inclinations, and hence, using symmetric panel models for both the structure and the free surface gave some interesting insight into the efficiency of frequency domain analyses. The results show little to no change in the added mass and damping coefficients located on the main diagonal, but severe changes in the off-diagonal coefficients. The force and response transfer functions of the body show small deviations for surge, heave, and pitch responses, and hence, proved quite well at describing the dynamic behavior of the structure. The wave force transfer functions show similar small deviations. The quadratic transfer functions show almost identical results with and without rotations. The study suggests that further investigation is needed to determine the effect of off-diagonal terms on coupled analyses and to determine whether the results apply to other substructure designs. In order to properly assess the results, time-domain simulations were performed at a later stage.

- For the comparison of the motion response of the damaged FOWTs under different damage conditions and environmental loads, one may conclude large differences between the different loading conditions. The fourth damage case, in which experiences significant changes in the perpendicular plane to the environmental headings experienced little to no change in regards to the intact condition for the milder environmental load cases. The second damage case on the other hand experienced mean surge increases of 19.46% and 19% for the first two environmental load cases. In terms of pitching, the fourth damage case also experienced similar behavior to the intact configuration, but also here, the second damage case experienced mean value differences in the offset of 9.77° and 9.76° which is a significant difference. It was also noticed that it may reach critical values if the waves and wind direction were to be reversed. For the third load case which was of extreme nature, the fourth damage case experienced a reduction in mean offsets in both DOFs with regards to the intact condition. The second damage case on the other hand experienced increased mean offsets. Overall, it was seen that the mean offsets and STDs for the second damage case increased, while for the fourth the surge STD increased, while the pitch STD decreased.

- For the emergency shutdowns, it was seen that in general, severe sudden changes in loading conditions should be expected. In terms of the nacelle accelerations, the values for the axial acceleration during the shutdown process far exceeds the suggested operational limit. For the motions, the most severe change in surge are observed for the fourth damage case. In general, the stability behind the procedure is reduced for both of the damage cases as one may notice by comparing the standard deviations.

- In terms of the continued time-domain analyses corresponding to the frequency-domain analyses with and without the applied inclinations, results were gathered in terms of its viability. The simulations show an increase in the mean surge response for the configuration without applied inclinations and a small reduction in the mean value for pitch offsets. The presence of the operating wind turbine reduces the differences significantly due to the dominance of aerodynamic forces. However, there is still an increase in the standard deviation of 3.85%, highlighting the difference in the behaviors of the two configurations. Despite the changes in statistics, the configuration without applied rotations captures the dynamic behavior of the damage case well. The difference in trim angles from the frequency-domain analyses was about 4°, which is not very significant. The results emphasize the importance of performing analyses in a correct manner, despite the reduced computational cost for cases without applied inclinations, and suggest that it may be interesting to re-do the analyses using CFD methods.

- For the environmental forces, clear differences are noticed when comparing the intact configuration with the damage cases. Despite the different types of damage presented in damage case 2 and 4, one may observe similar changes in the hydrodynamic forces in relation to the intact configuration. For the hydrodynamic first-order loads, the fourth damage case experiences a slight increase in loads compared to the second damage case. For the QTF forces, the

opposite is observed. In terms of the aerodynamic forces, smaller changes are experienced between the different loading conditions. This is to be expected considering the properties of the turbine structure remain the same.

10.2 Further Work

Based on the work and results presented in this master's thesis, suggestions and improvements for further enchantment of the knowledge in related field of work is presented.

- Proper use of CFD in order to look closer at the differences between potential flow methods and CFD in terms of capturing the effects of static inclinations, the effect on the Morrison coefficient due to damage, and transient effects.
- Simulations considering different headings of wind and waves in order to further investigate the damage scenarios, and the potential severity.
- Simulations in which compares the forces on the mooring system, including the anchors, and potential fatigue damage in order to perform a proper safety assessment of the damage cases.
- Performing a proper environmental analysis of the selected location by the means of captured data. In this case, it might be good to use for example NORA3 data.
- Investigation of proper collision severity of FOWTs, the potential damage size, and forces due to collision with e.g. a service vessel.

Appendix

A Wadam results convergence test of panel model

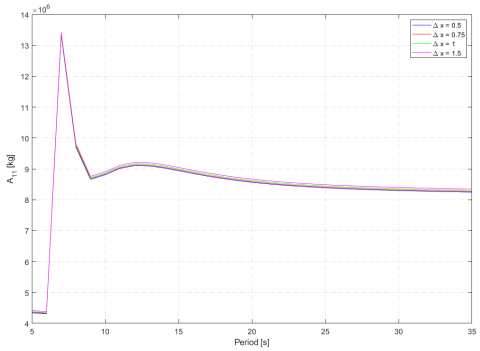

(a)

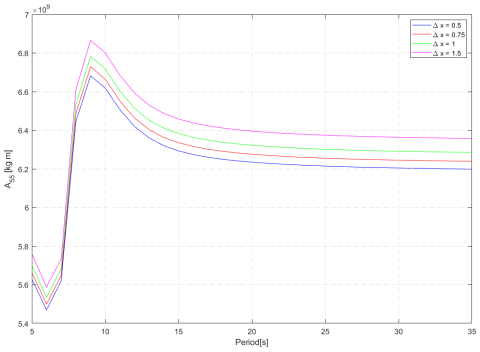

(b)

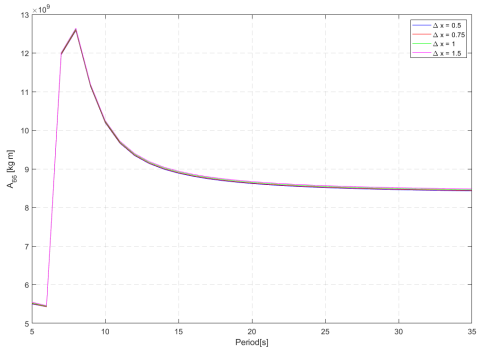

(c)

Figure .1: Added mass convergence study

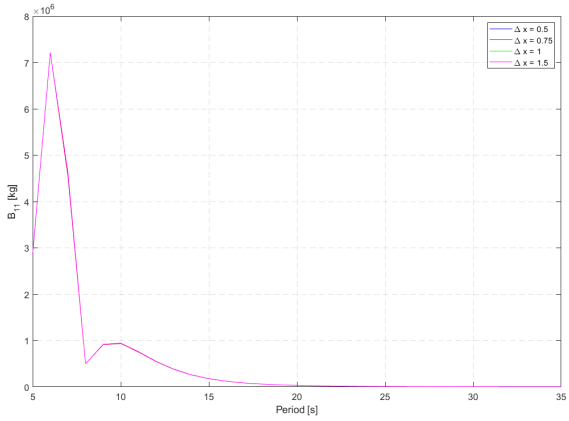

(a)

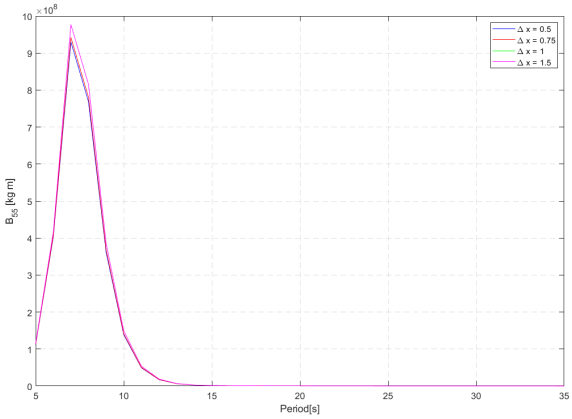

(b)

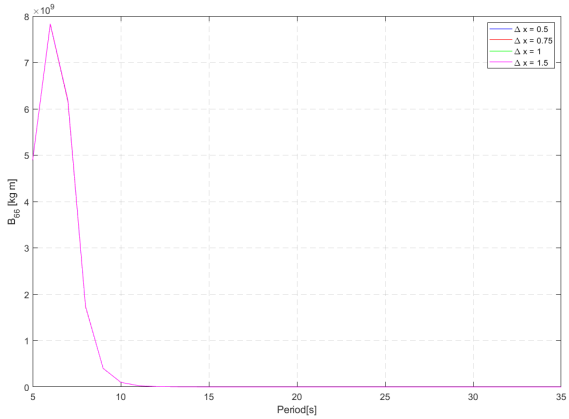

(c)

Figure .2: Damping convergence study

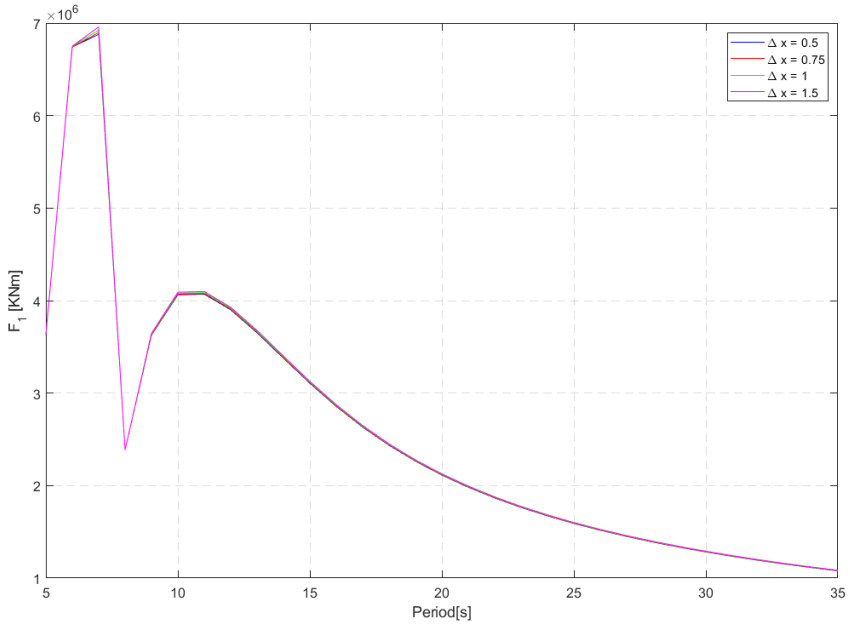

(a)

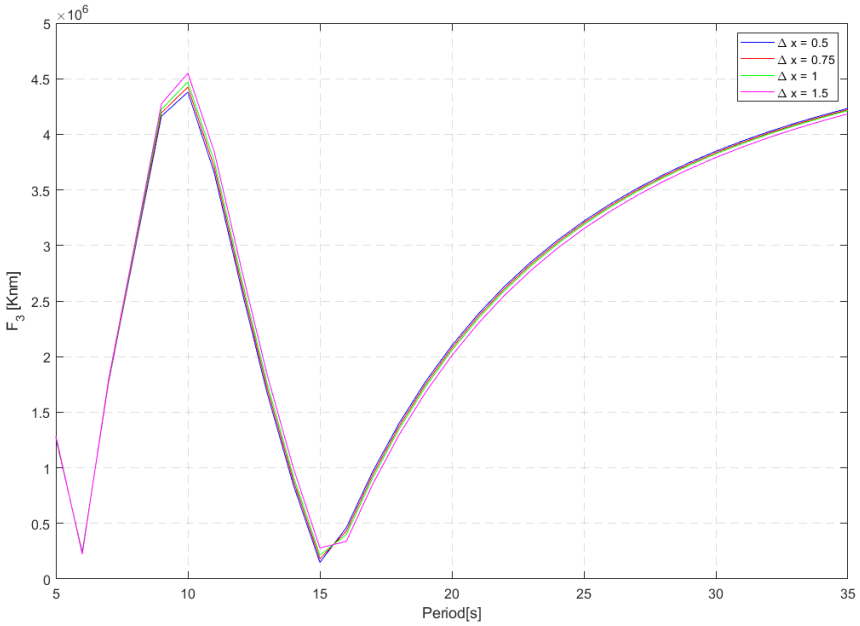

(b)

Figure .3: Force transfer function convergence study

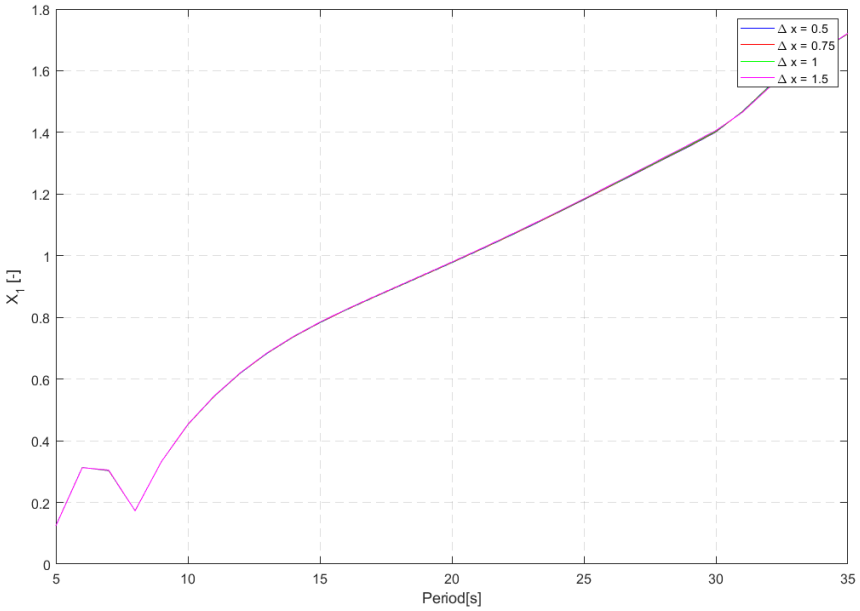

(a)

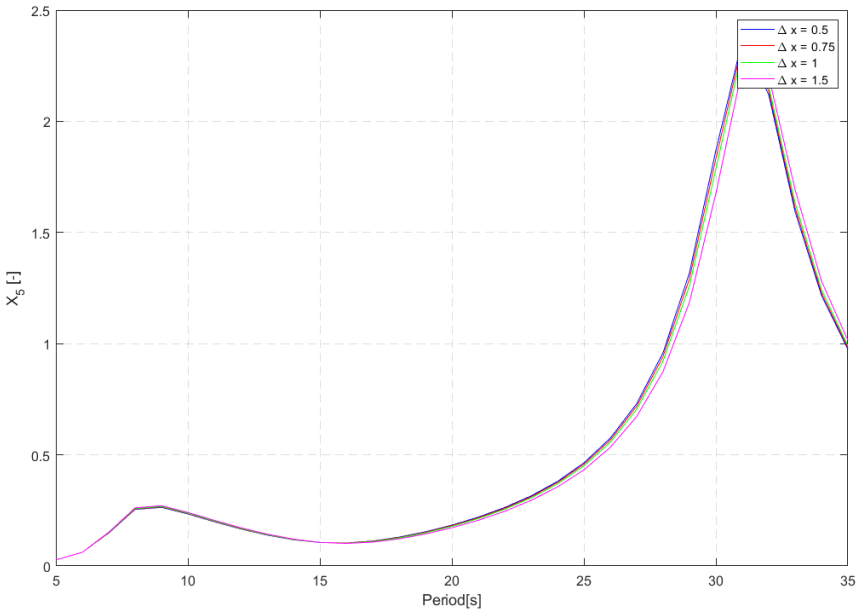

(b)

Figure .4: Motion transfer function convergence study

B Wadam results validation of panel model

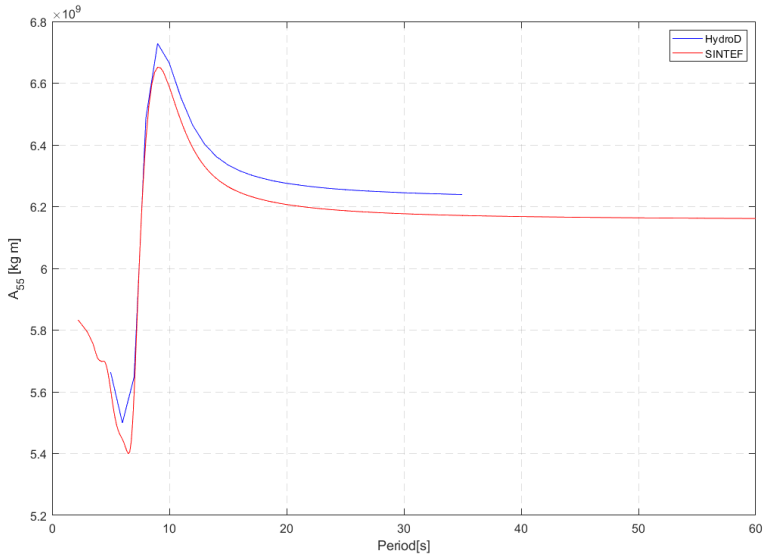

(a)

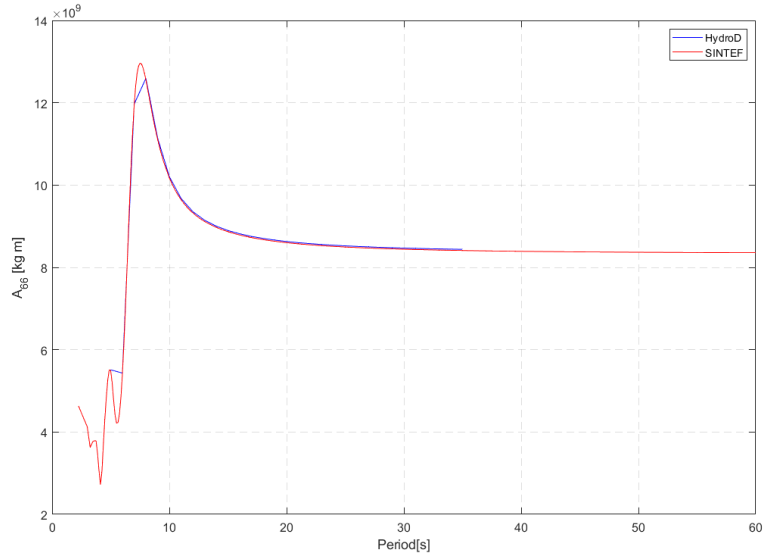

(b)

Figure .5: Validation of model added mass

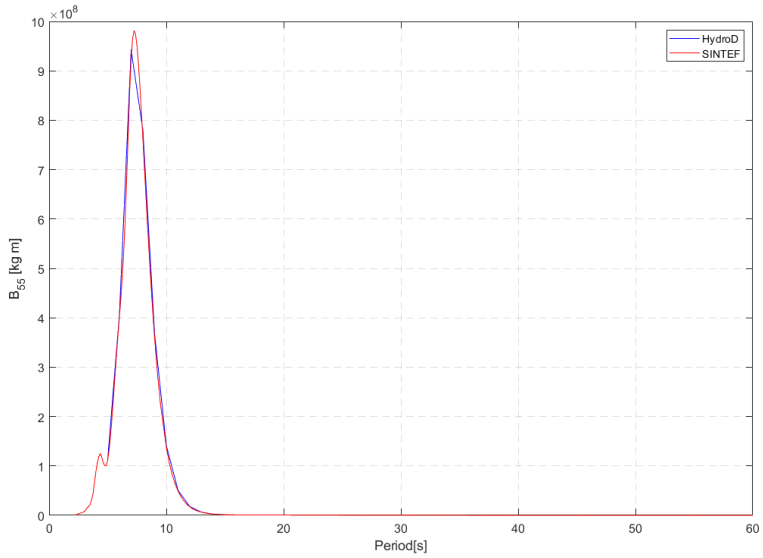

(a)

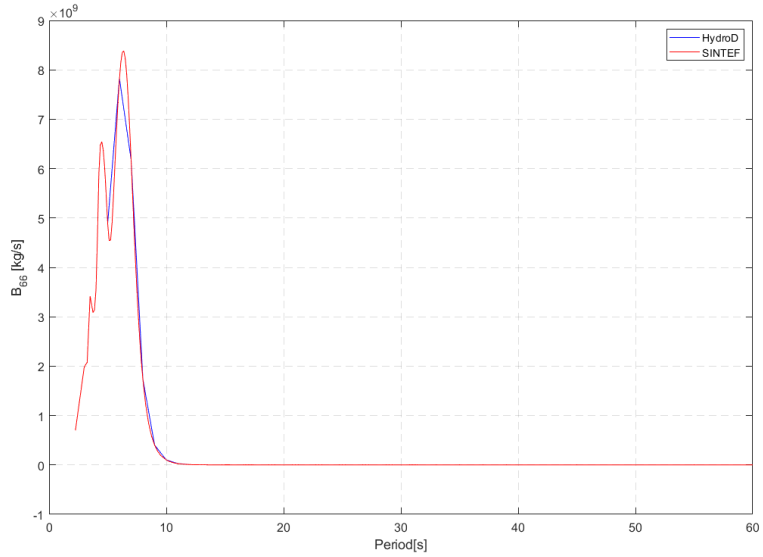

(b)

Figure .6: Validation of model damping

C Wadam results validation of combined panel- and compartment model

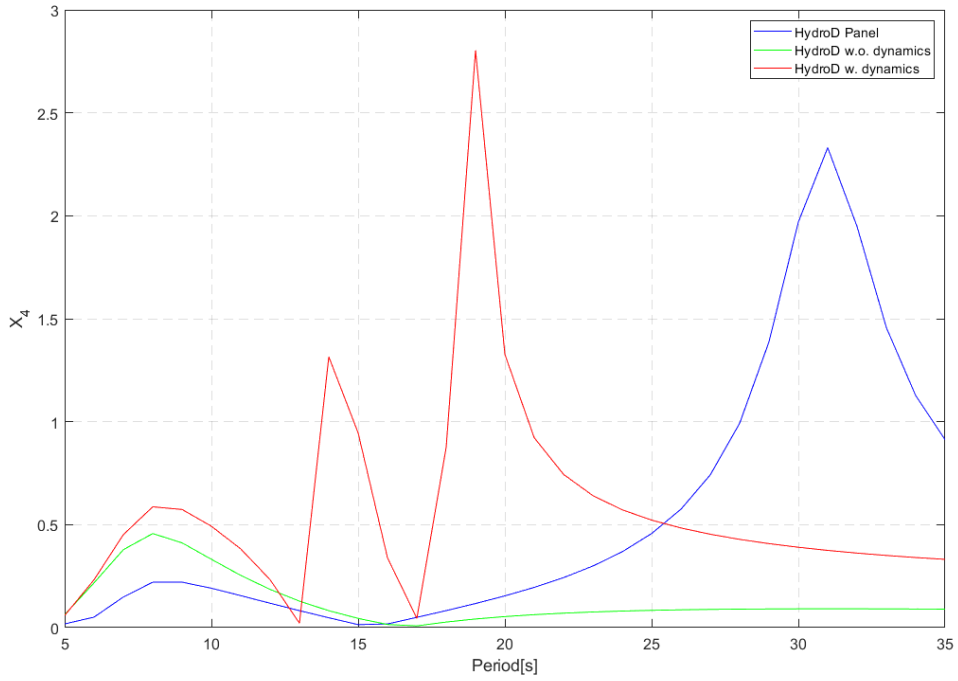

Figure .7: Roll RAO validation Compartment model 1

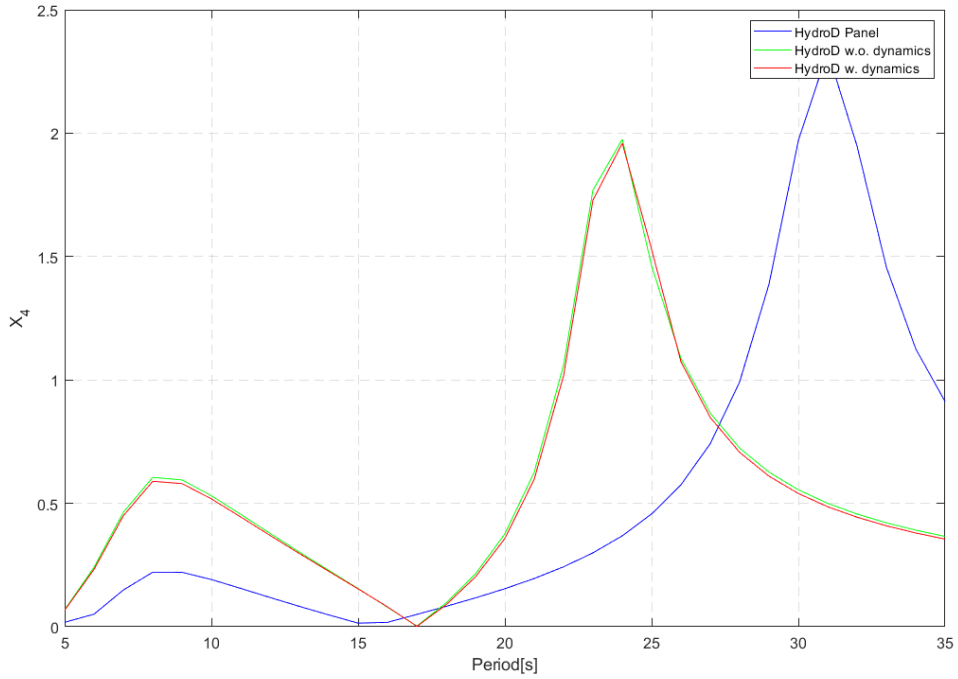

Figure .8: Roll RAO validation Compartment model 2

D Wadam results comparison of damage case hydrodynamic coefficients

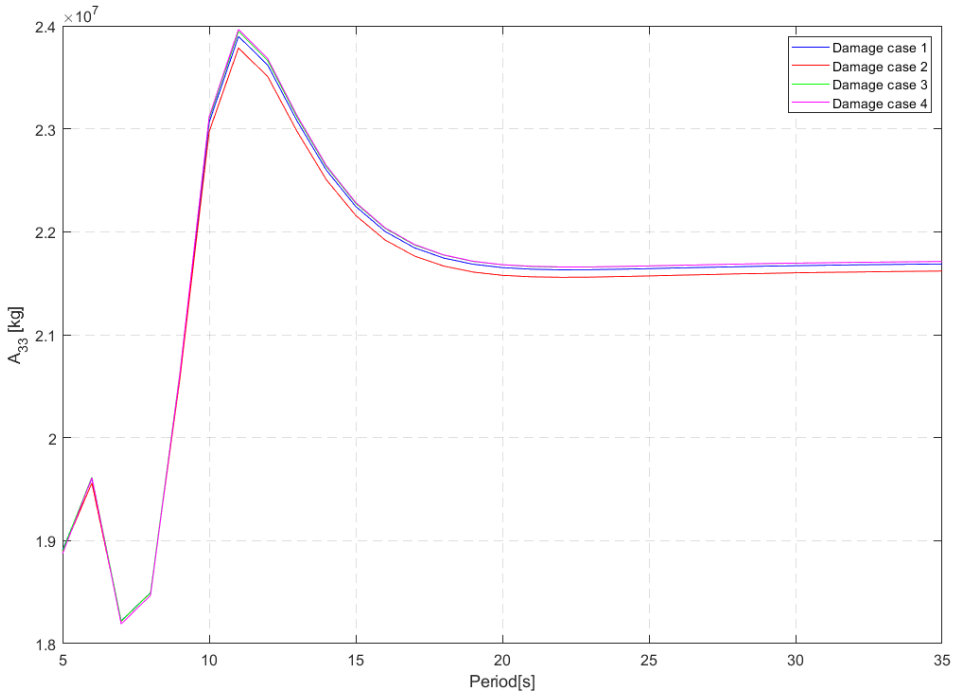

(a) Added mass heave-heave

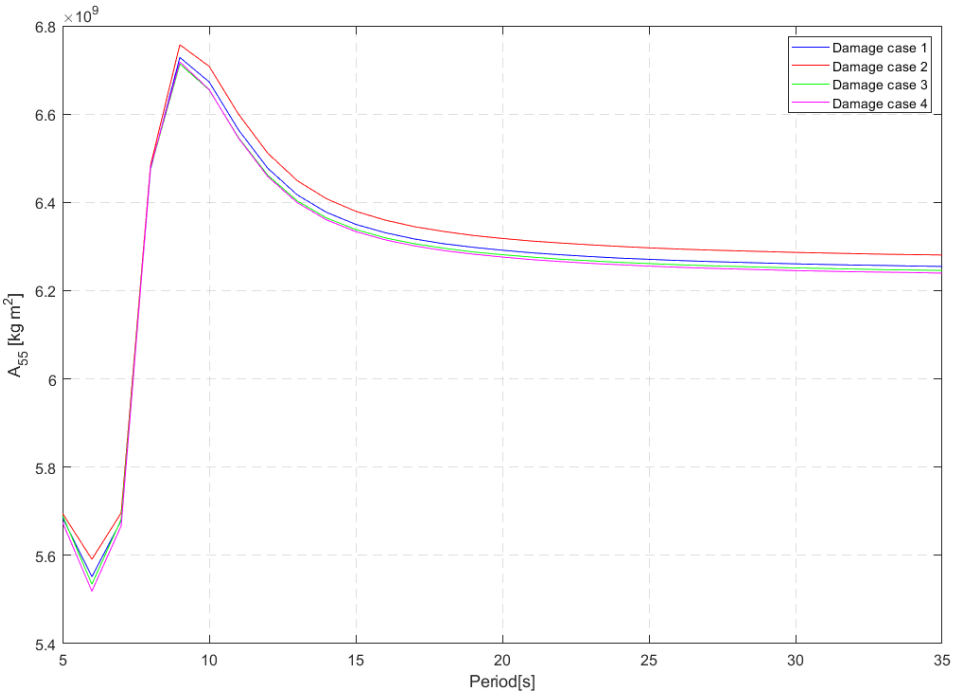

(b) Added mass pitch-pitch

Figure .9: Added mass

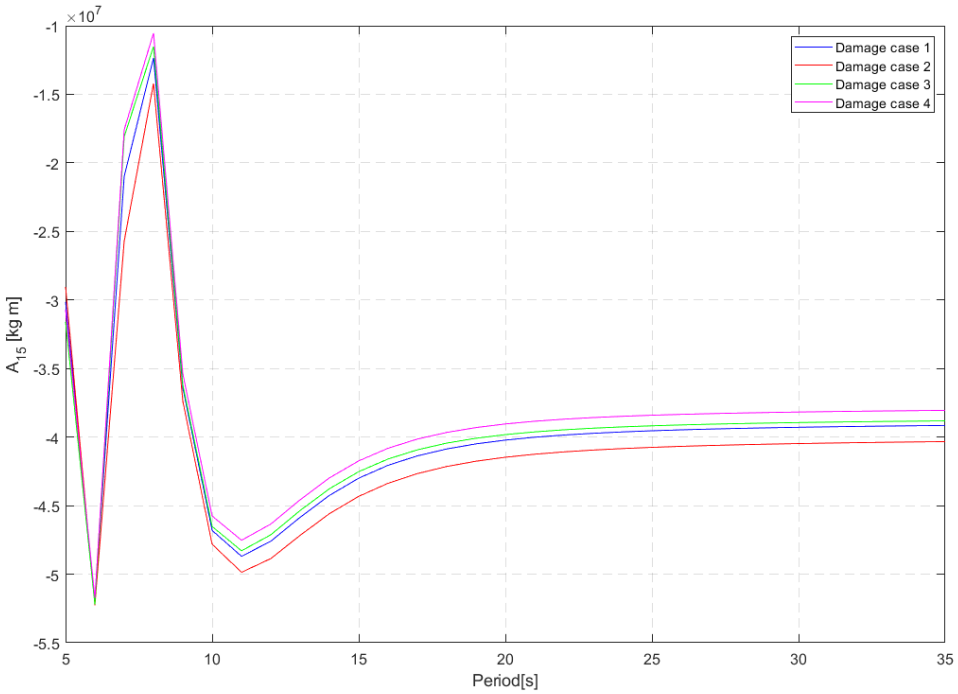

(a) Added mass surge-pitch

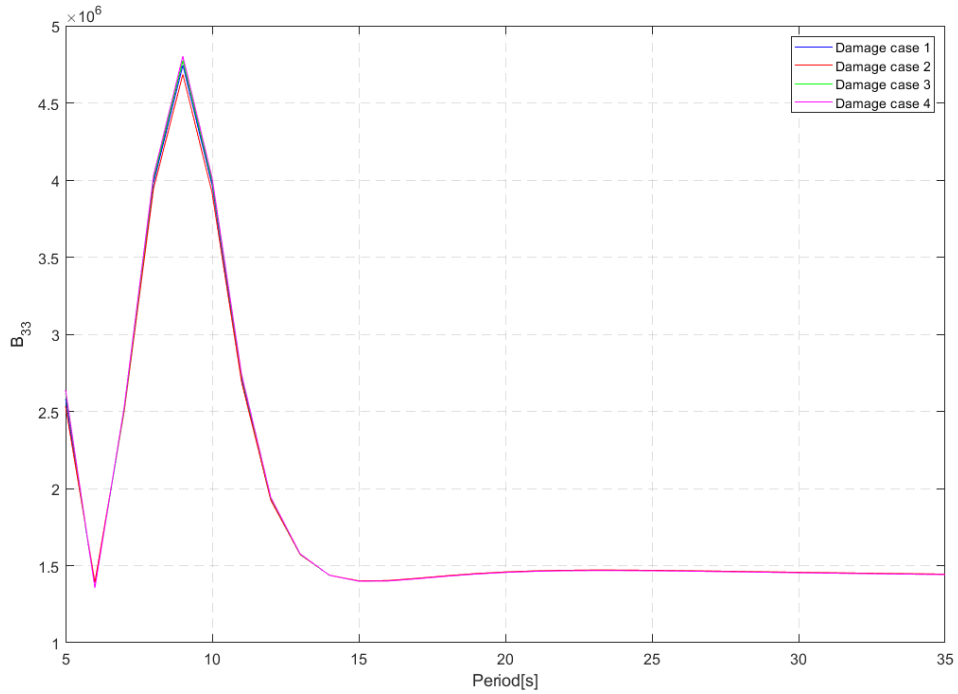

(b) Damping heave-heave

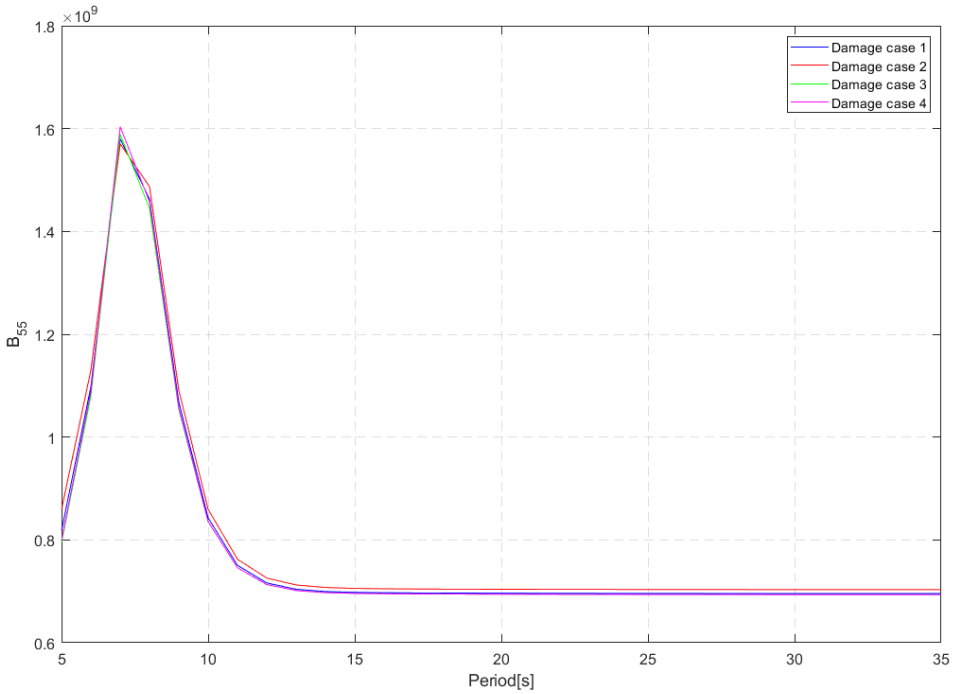

(a) Damping pitch-pitch

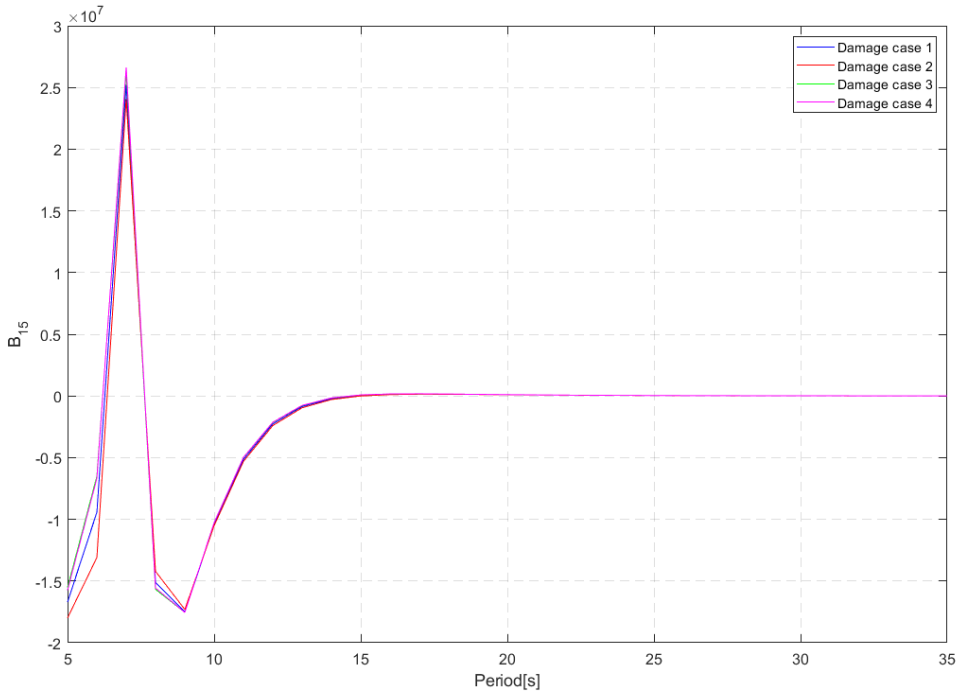

(b) Damping surge-pitch

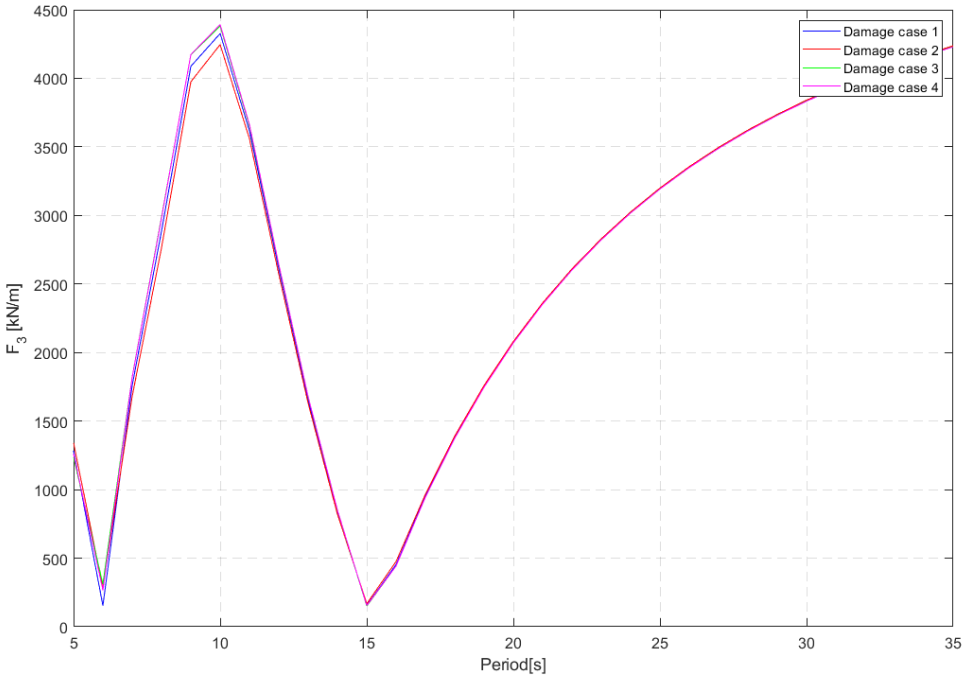

(a) Wave excitation transfer function heave

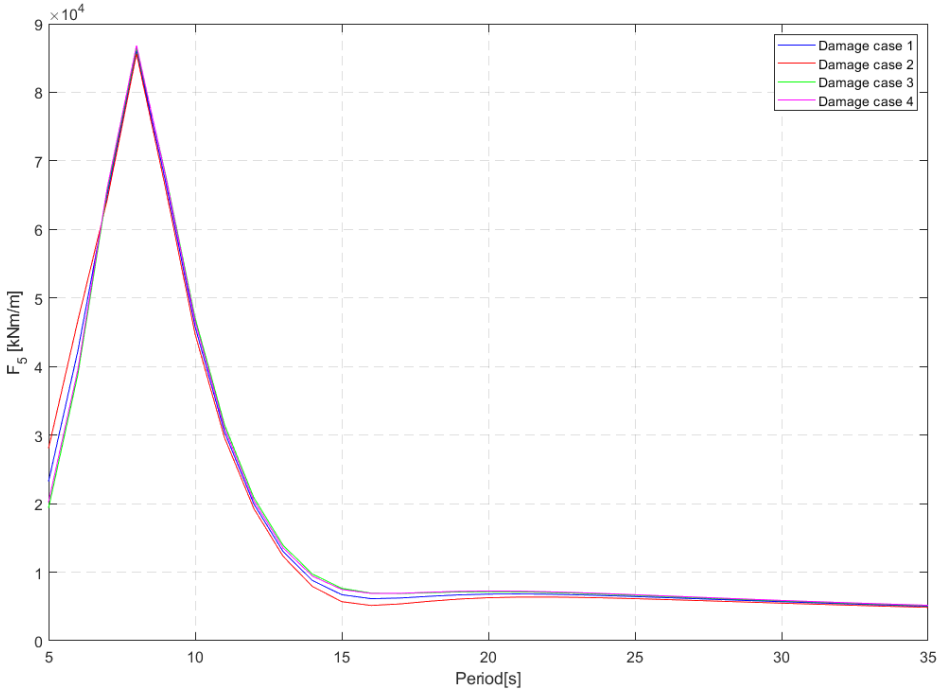

(b) Wave excitation transfer function pitch

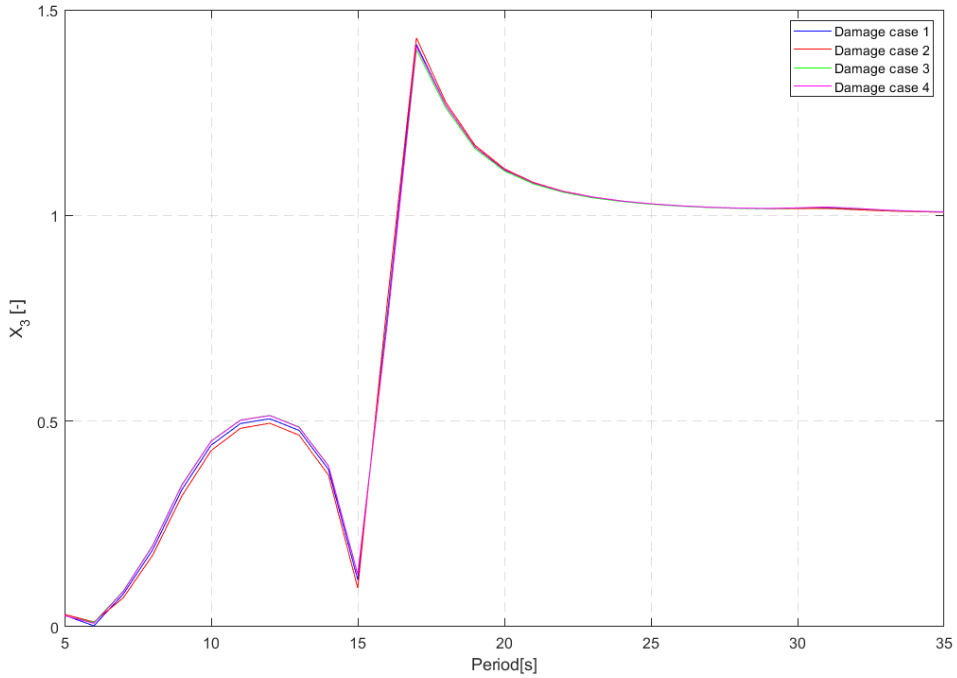

(a) Response amplitude operator heave

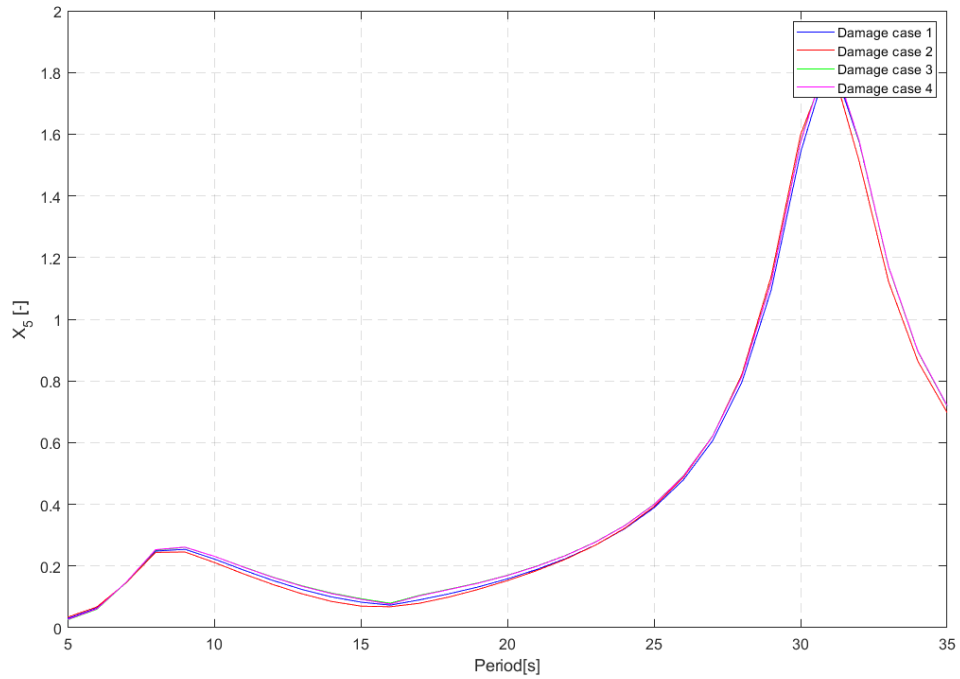

(b) Response amplitude operator pitch

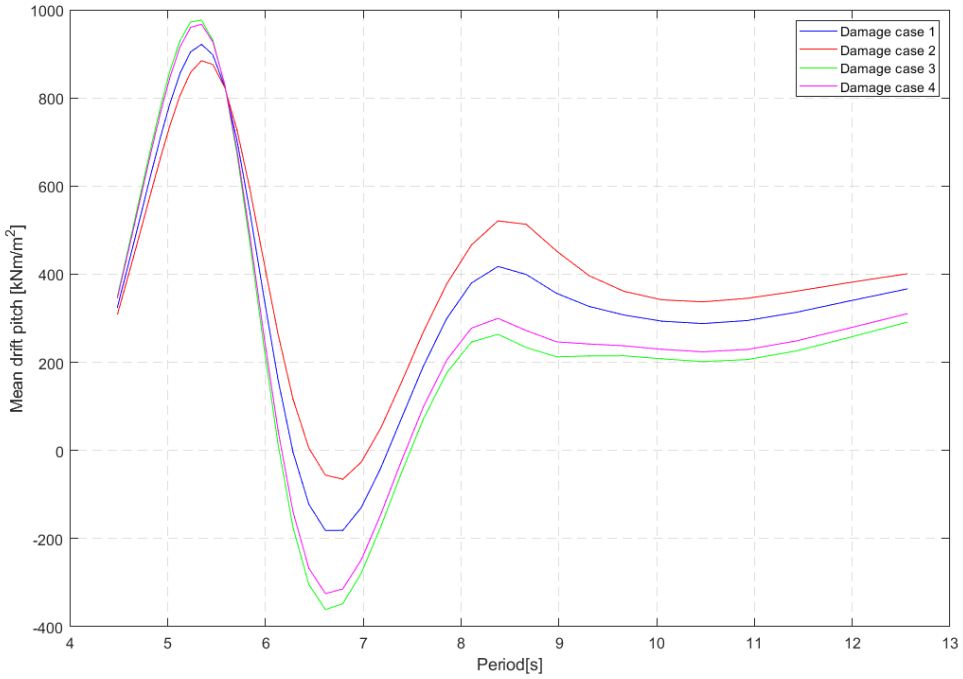

Figure .14: Mean drift force pitch

E Free decay tests damage conditions

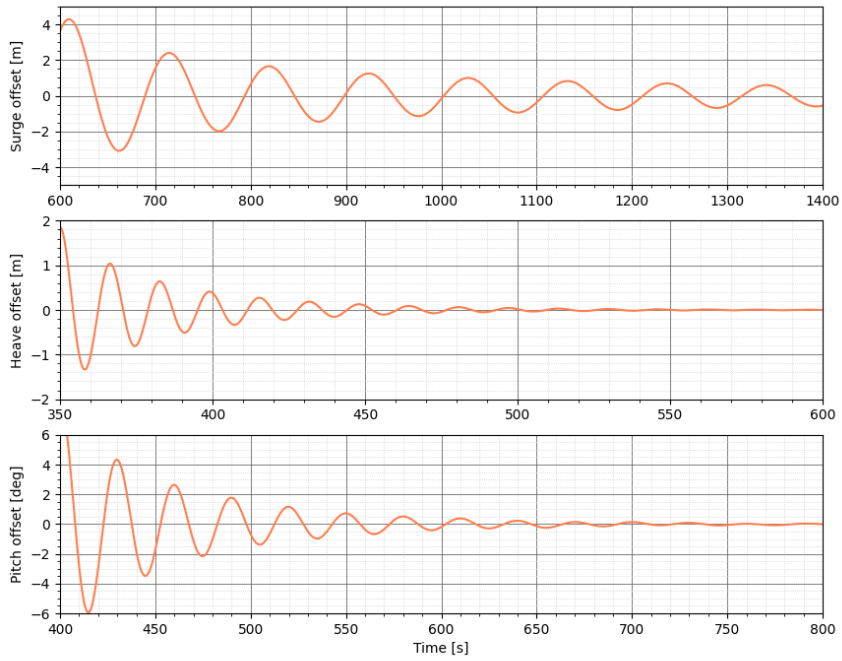

Figure .15: Decay test damage condition 1

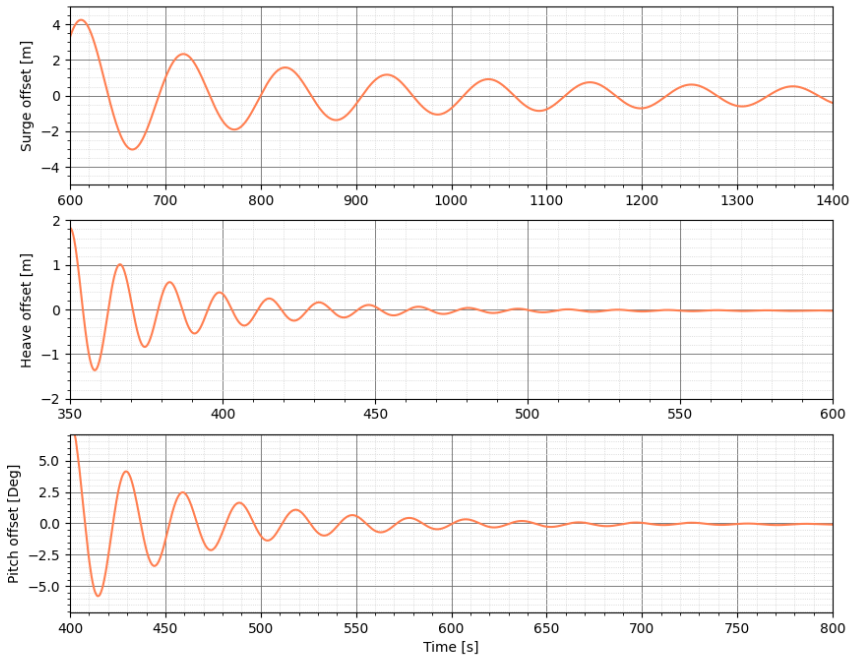

Figure .16: Decay test damage condition 2

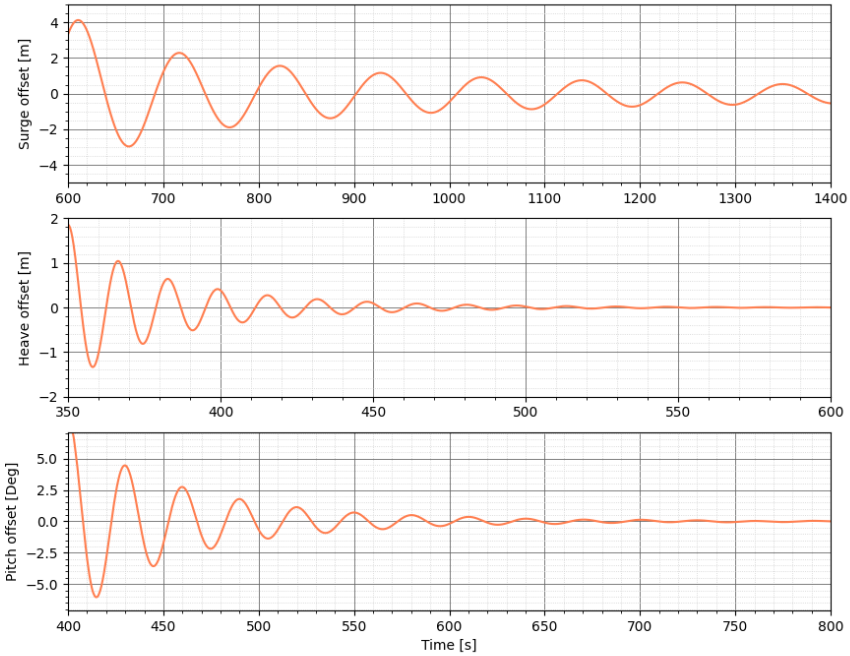

Figure .17: Decay test damage condition 3

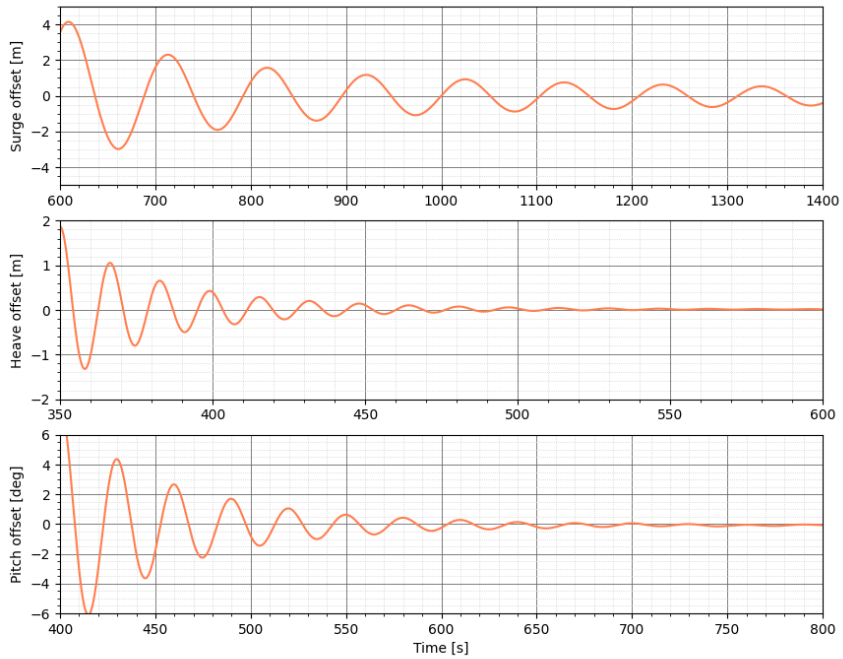

Figure .18: Decay test damage condition 4

F Rotations hydrodynamic data

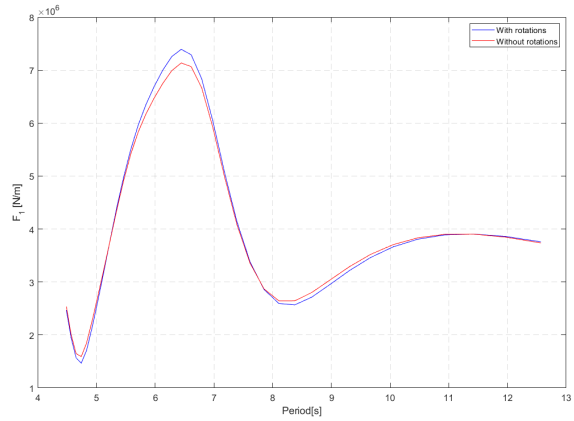

(a) Surge

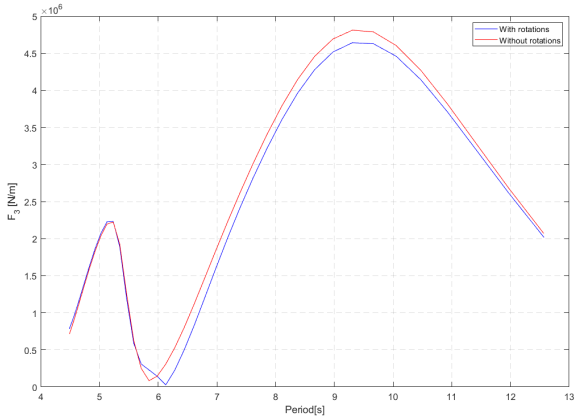

(b) Heave

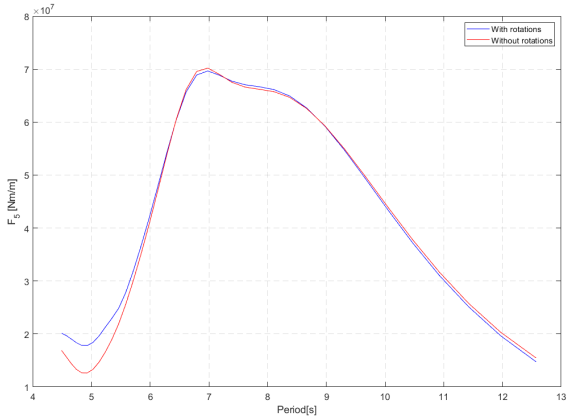

(c) Pitch

Figure .19: Force transfer functions

G Response time series

LC1

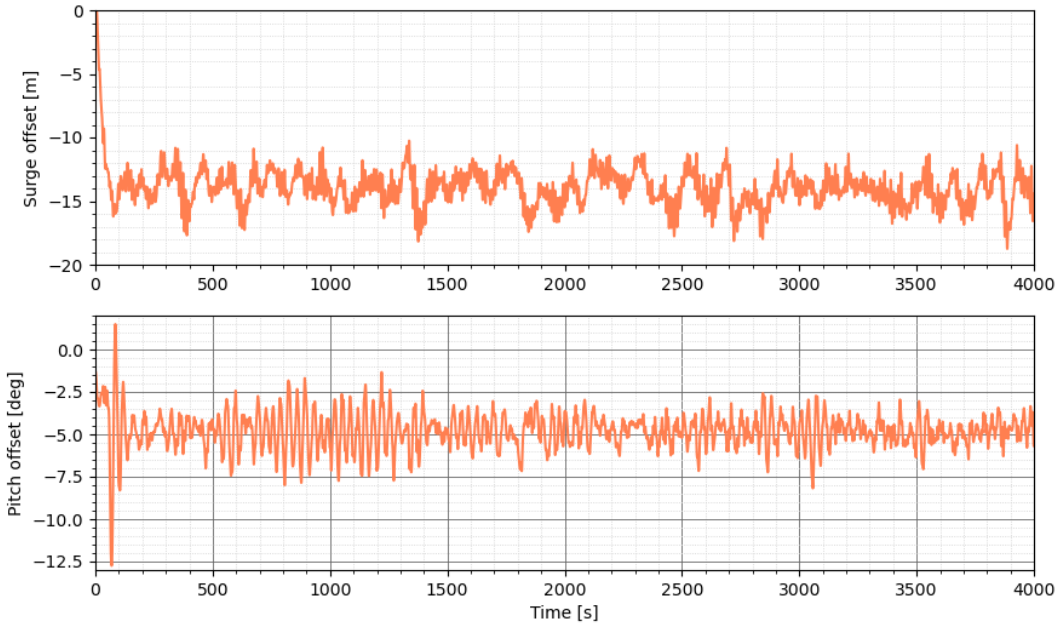

Figure .20: Response time series intact condition - LC1

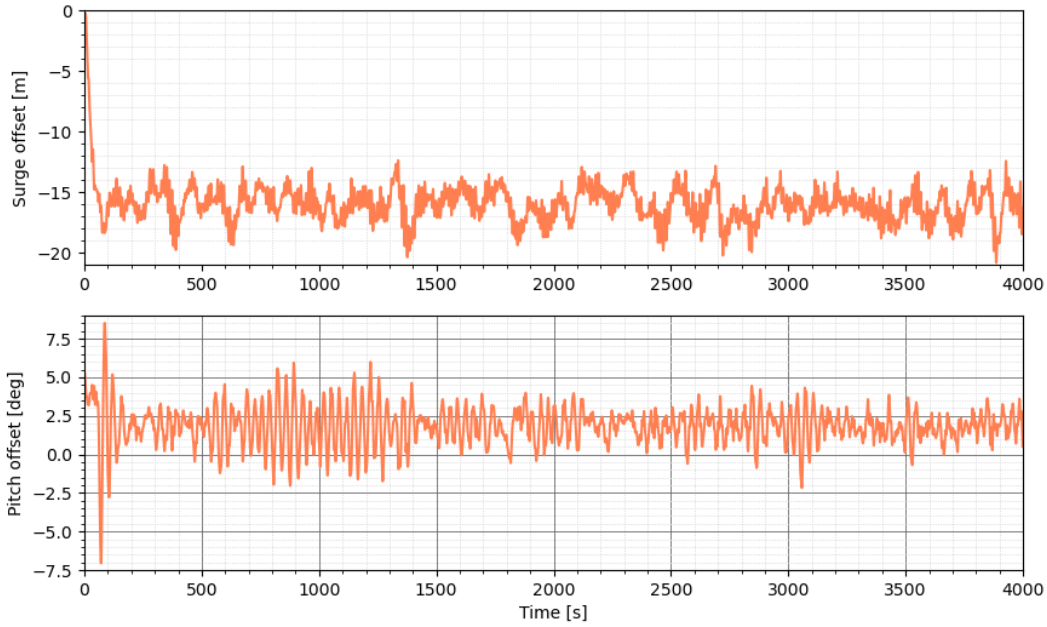

Figure .21: Response time series damage case 1 - LC1

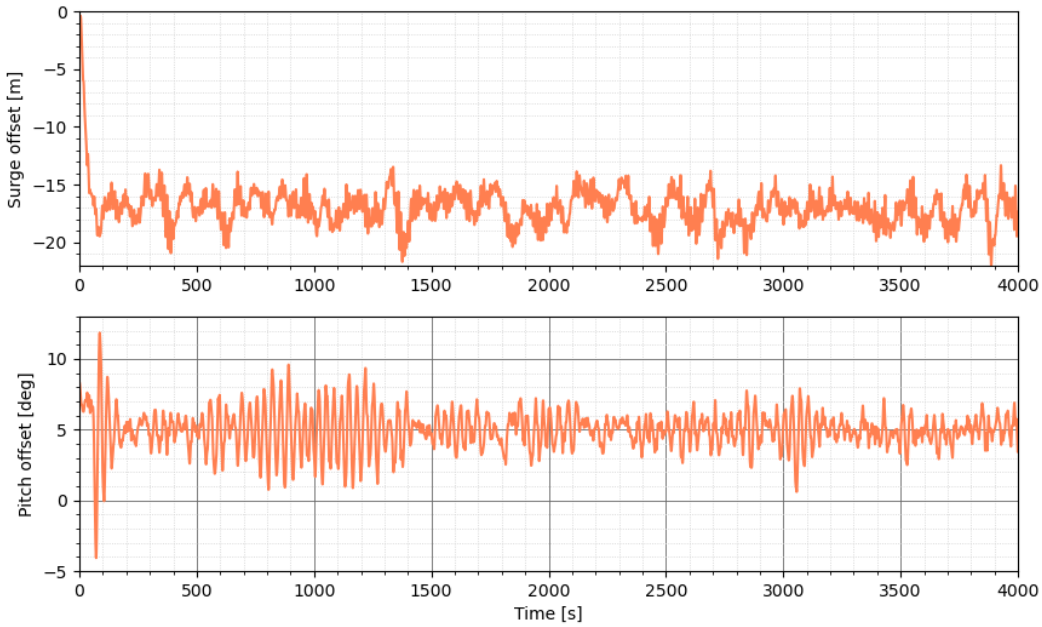

Figure .22: Response time series damage case 2 - LC1

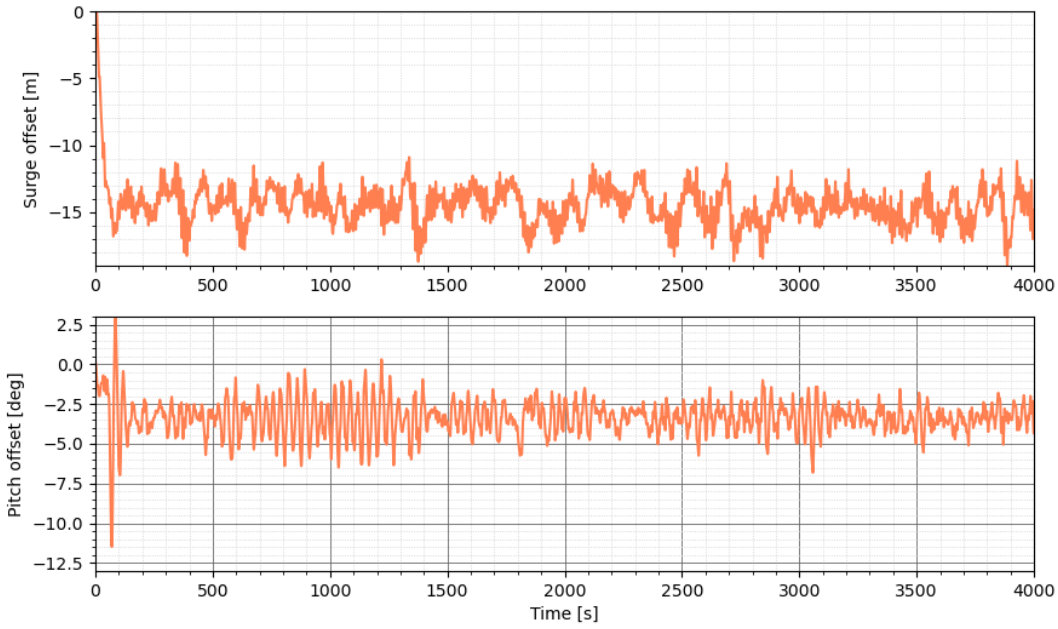

Figure .23: Response time series damage case 3 - LC1

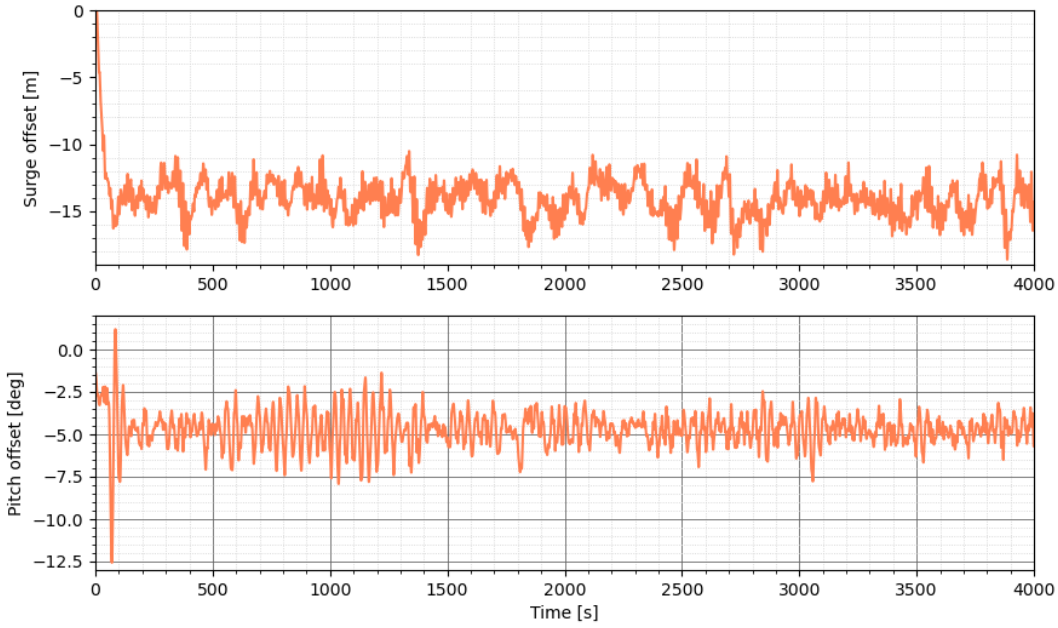

Figure .24: Response time series damage case 4 - LC1

LC2

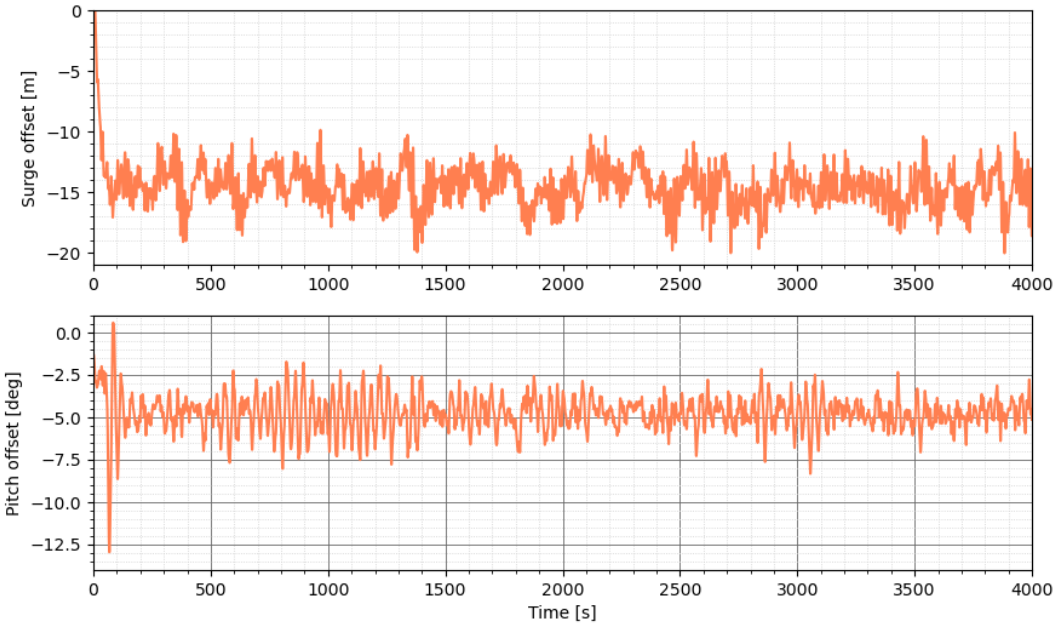

Figure .25: Response time series intact condition - LC2

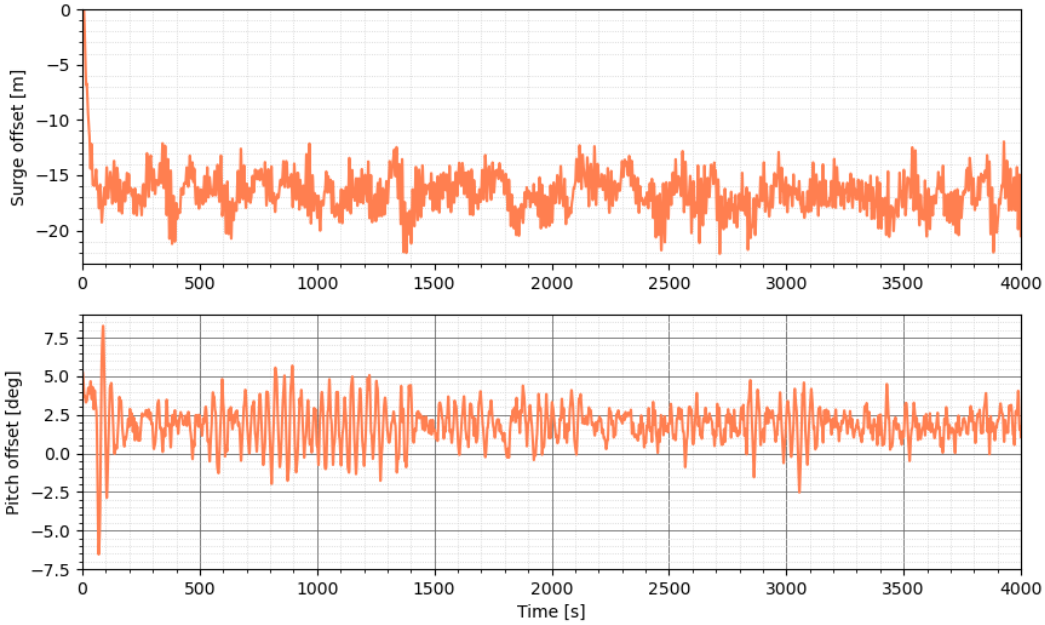

Figure .26: Response time series damage case 1 - LC2

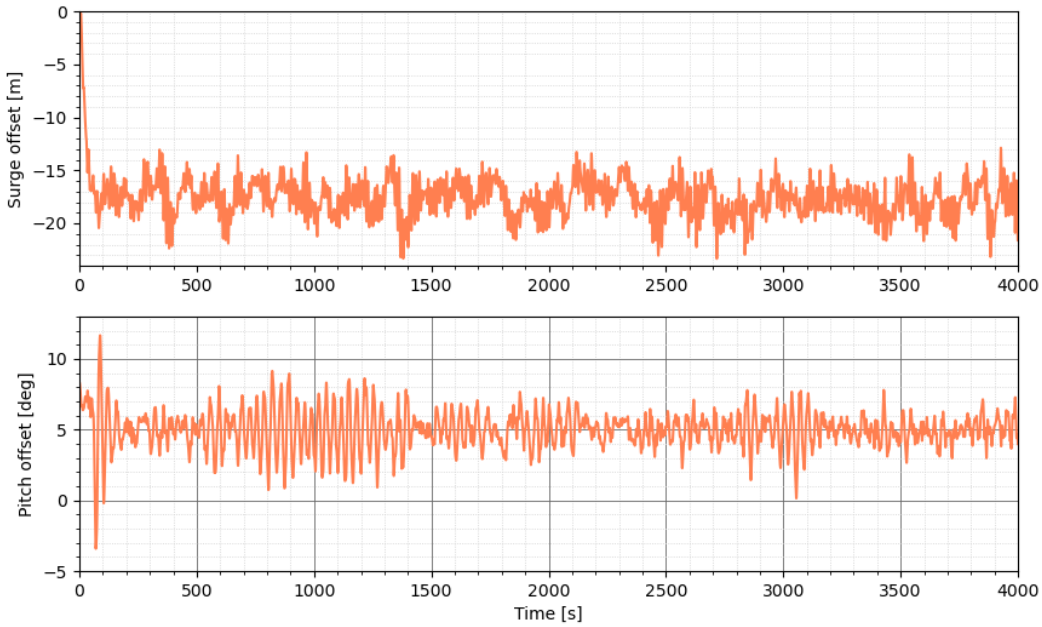

Figure .27: Response time series damage case 2 - LC2

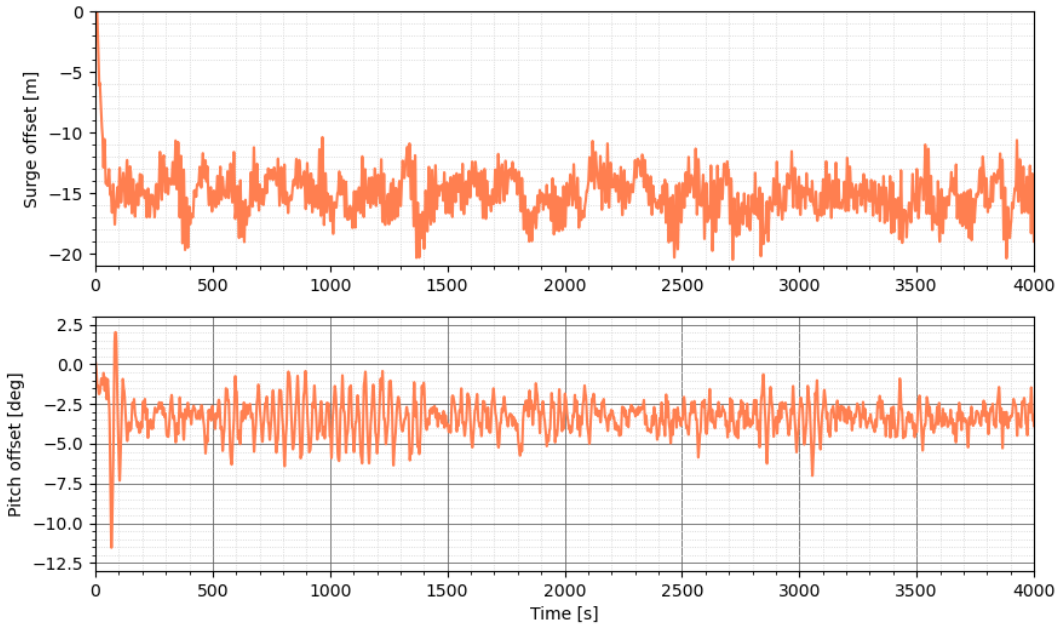

Figure .28: Response time series damage case 3 - LC2

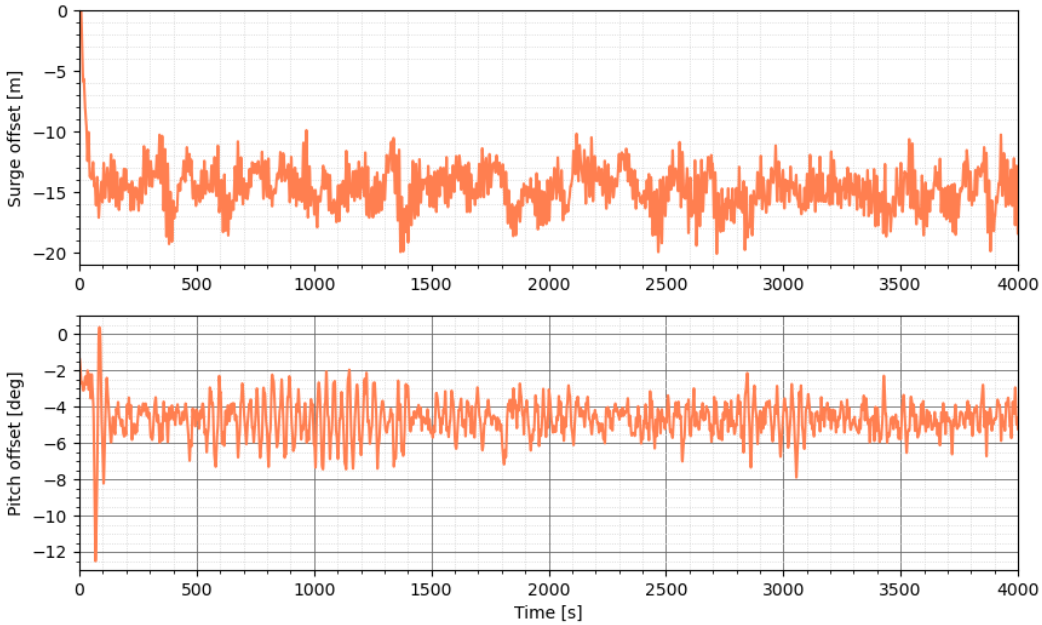

Figure .29: Response time series damage case 4 - LC2

LC3

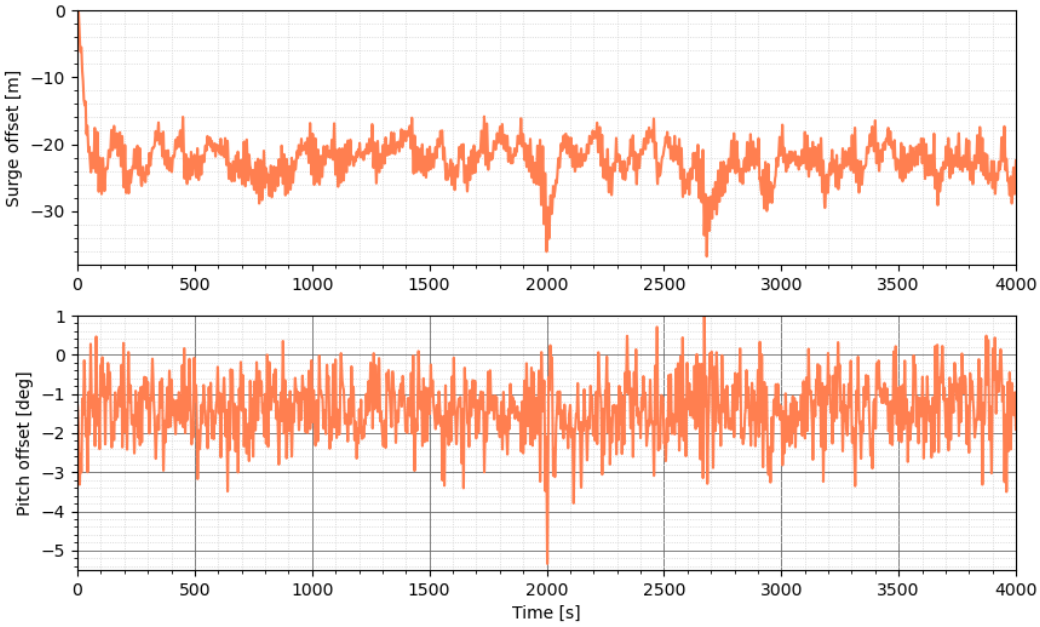

Figure .30: Response time series intact condition - LC3

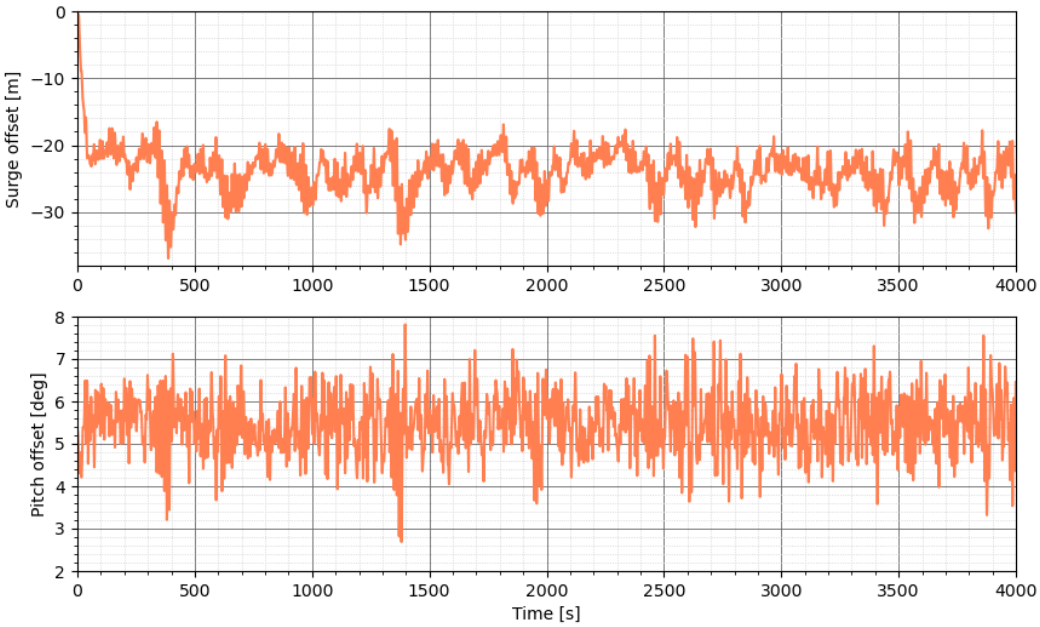

Figure .31: Response time series damage case 1 - LC3

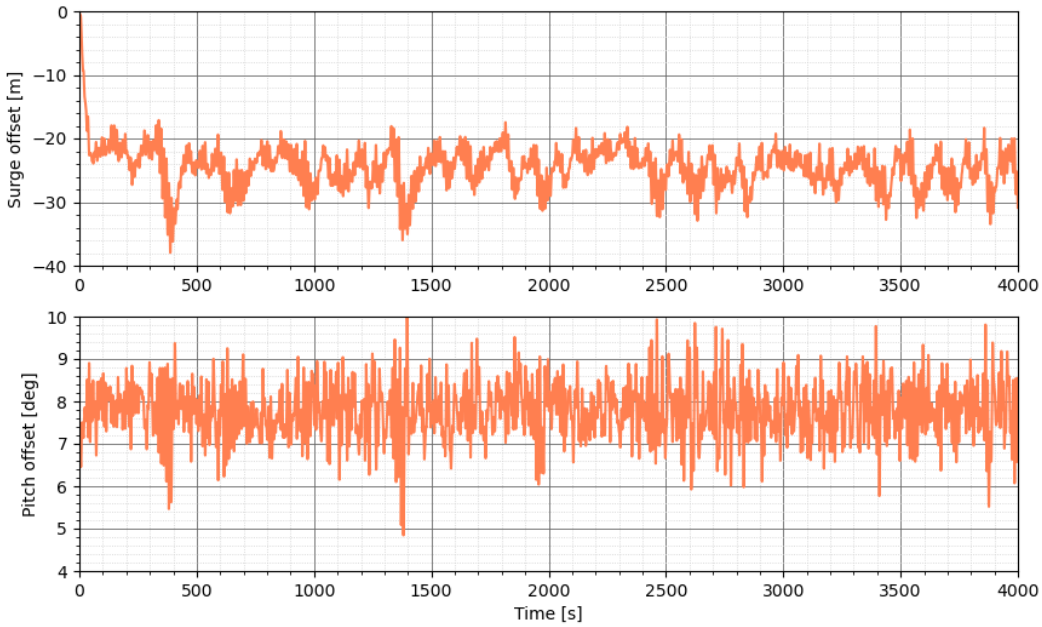

Figure .32: Response time series damage case 2 - LC3

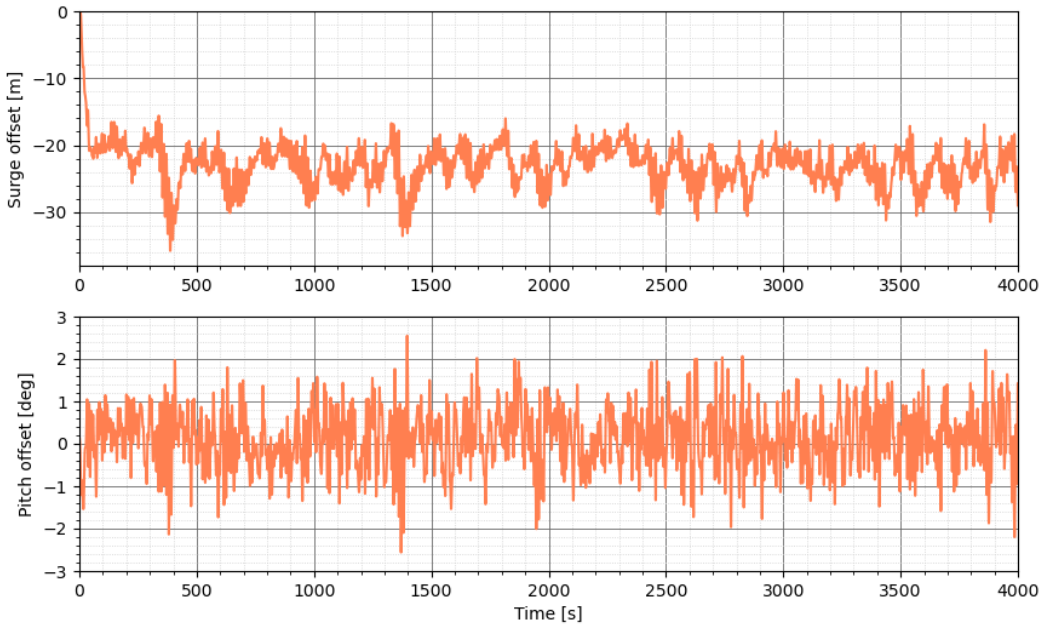

Figure .33: Response time series damage case 3 - LC3

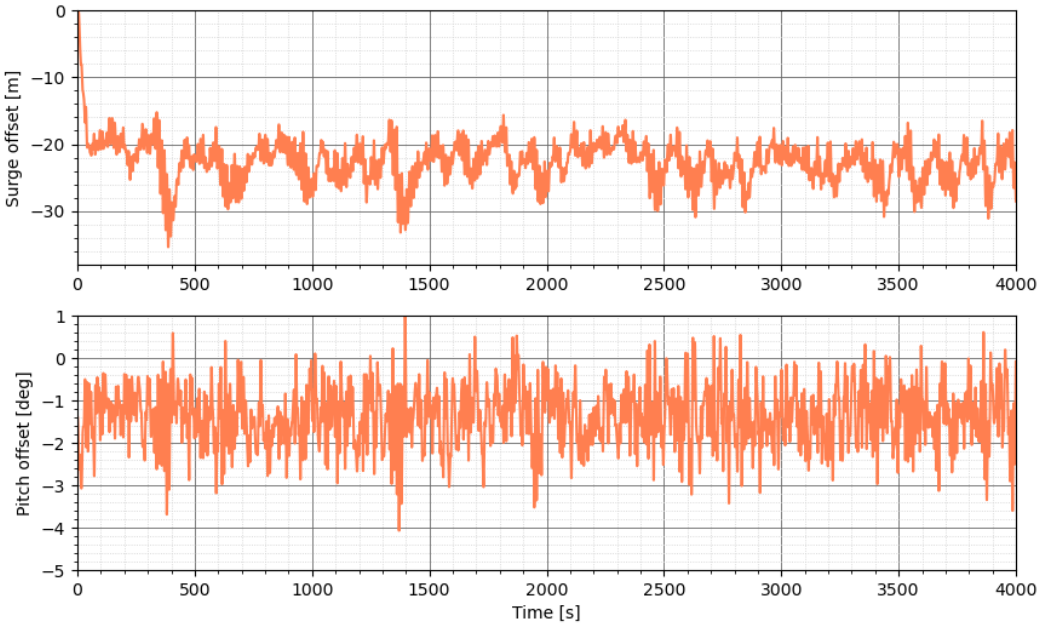

Figure .34: Response time series damage case 4 - LC3

Emergency shutdown

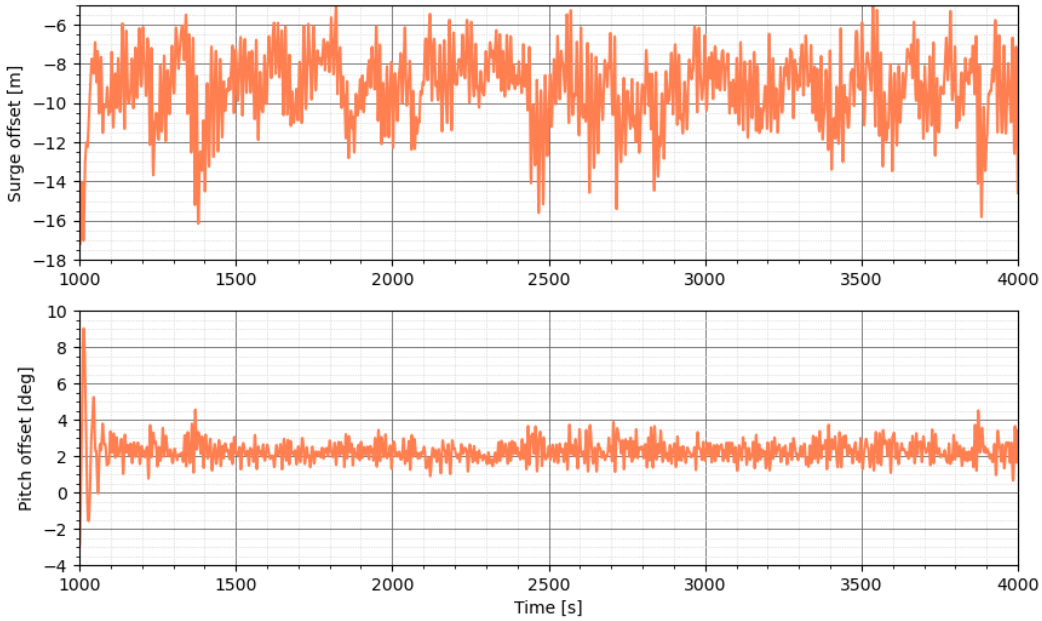

Figure .35: Response time series intact condition - Emergency shutdown

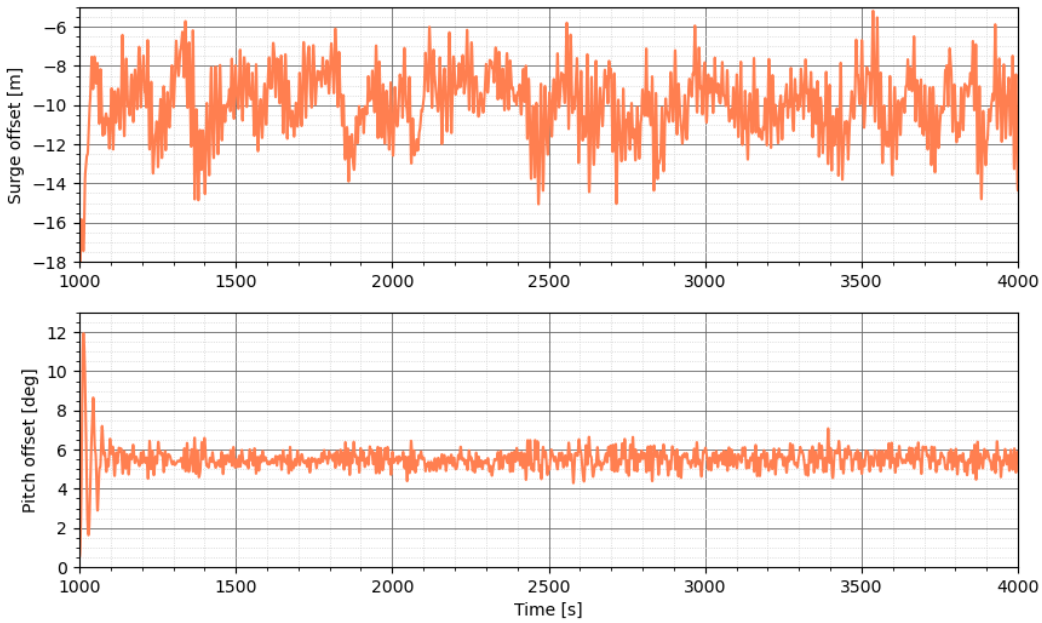

Figure .36: Response time series damage case 1 - Emergency shutdown

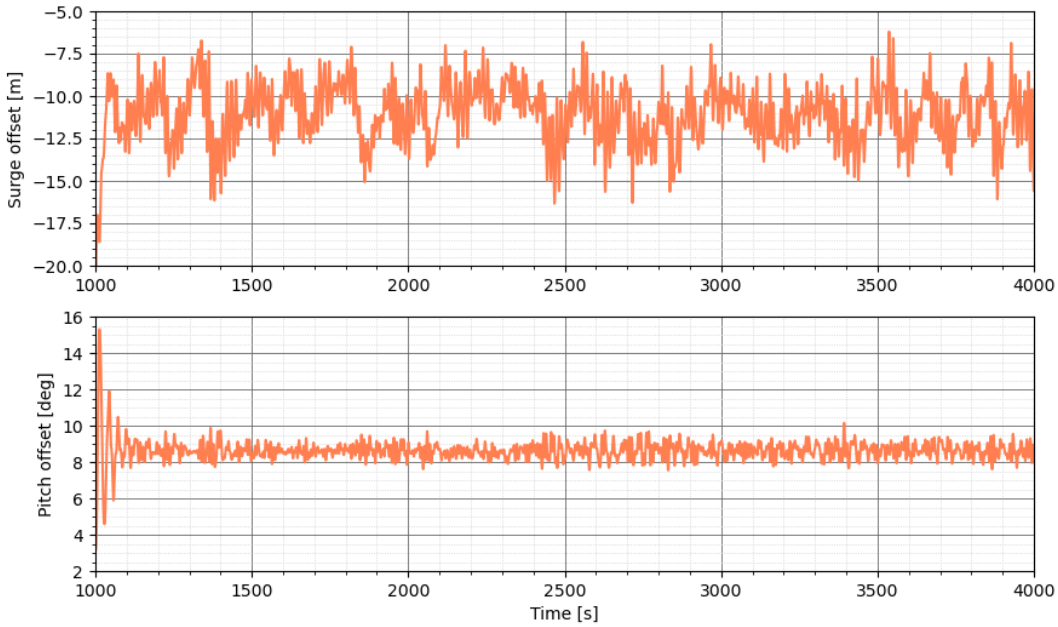

Figure .37: Response time series damage case 2 - Emergency shutdown

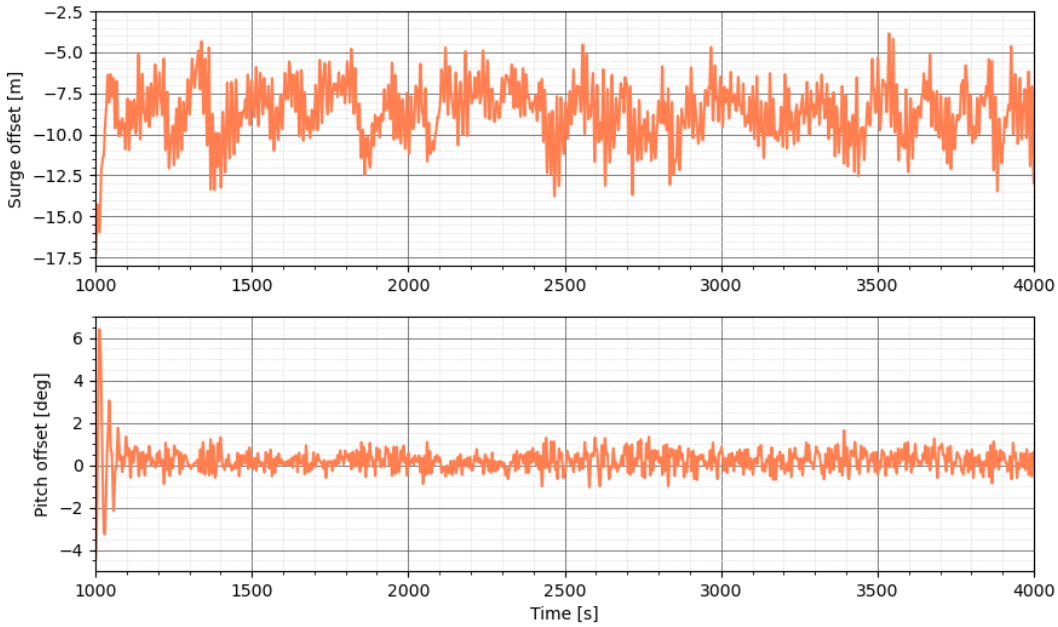

Figure .38: Response time series damage case 3 - Emergency shutdown

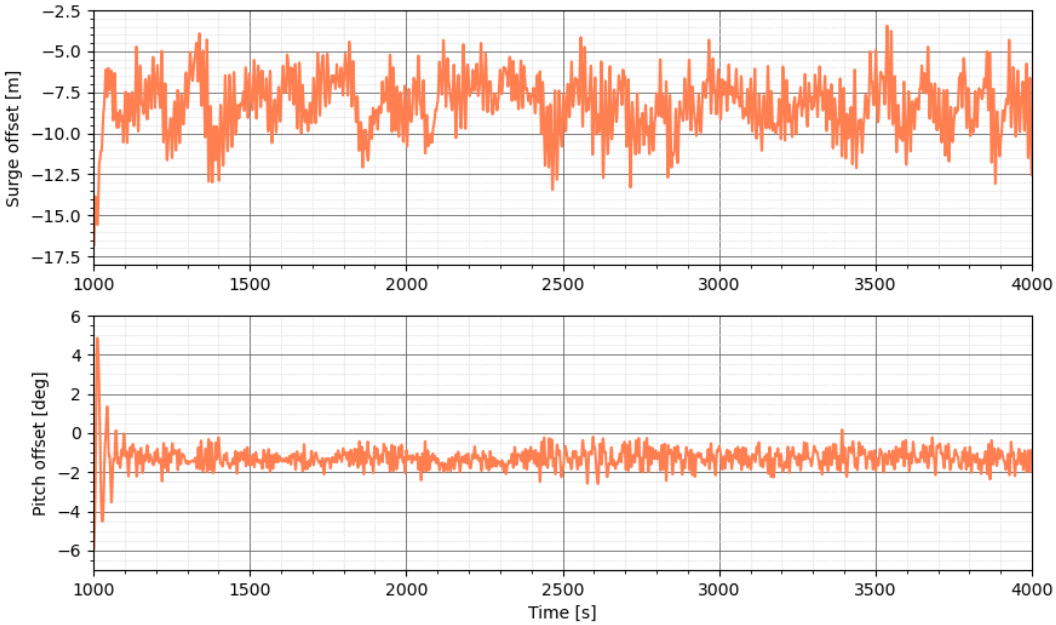

Figure .39: Response time series damage case 4 - Emergency shutdown

Bibliography

Anaya-Lara, O., Tande, J. O., Uhlen, K., & Merz, K. (2018). *Offshore wind energy technology*. John Wiley amp; Sons.

(anι*ee*), *A.L.*. (2023). Cargo ship hits turbine at north sea wind farm: Orsted investigates. https://www.rechargenews.com/wind/cargo-ship-hits-turbine-at-north-sea-wind-farm-orsted-investigates/2-1-1442789

Bachynski, E. E., Kristiansen, T., Larsen, C. M., & Myrhaug, D. (2021). *Marine dynamics compendium*. NTNU.

Bachynski, E. E., & Moan, T. (2012). Design considerations for tension leg platform wind turbines. *Marine Structures*, *29*(1), 89–114. https://doi.org/10.1016/j.marstruc.2012.09.001

Bachynski-Polic, E. (2022a). Integrated dynamic analysis of wind turbines.

Bachynski-Polic, E. (2022b). Coupled analysis lecture.

Bachynski-Polic, E. ((2022)). Basic aerodynamics for wind turbines erin bachynski-poli c.

Chujo, T., Haneda, K., Komoriyama, Y., Kokubun, K., Yamada, Y., Fujiwara, T., & Inoue, S. (2020). Study on the consideration method of damage stability criteria corresponding to iec 61400-3-2 for floating offshore wind turbine. *Volume 9: Ocean Renewable Energy*. https://doi.org/10.1115/omae2020-18252

DNV. (2021). Dnv-st-0119: Floating wind turbine structures.

DNV. (2022a). Floating offshore wind: The next five years. https://www.dnv.com/focus-areas/floating-offshore-wind/floating-offshore-wind-the-next-five-years.html

DNV. (2022b). Sesam feature description dnv. https://www.dnv.com/publications/sesam-feature-description-84639

DNV-RP-C205. (2010). Dnv-rp-c205: Recommended practice - environmental conditions and environmental loads.

Du, A. (2021). Semi-submersible, spar and tlp – how to select floating wind foundation types? https://www.empireengineering.co.uk/semi-submersible-spar-and-tlp-floating-wind-foundations/

EDP. (n.d.). Windfloat atlantic project. https://www.edp.com/en/innovation/windfloat

Equinor. (2022). Hywind tampen. https://www.equinor.com/energy/hywind-tampen

Faltinsen, O. M. (1999). *Sea loads on ships and offshore structures*. Cambridge University Press.

Faltinsen, O. M., & Timokha, A. (2009). *Sloshing*. Cambridge University Press.

Gao, Z., & Moan, T. (2009). *Mooring system analysis of multiple wave energy converters in a farm configuration*.

Genie user manual v7.3. (2016).

GWECS. (2022). Gwecs global offshore wind report 2022. https://gwec.net/gwecs-global-offshore-wind-report/

Haslum. (2000). *Simplified methods applied to nonlinear motion of spar platforms* (Doctoral dissertation). NTNU.

Haslum, H. (2018). Ow coe and subseauk mooring and anchoring systems webinar. https://www.globalunderwaterhub.com/documents/documents2020/mooring%5C%20and%5C%20acnhoring%5C%20uk%5C%20webinar.pdf

Hydrod user manual v4.9. (2016).

IPCC. (2022). Climate change 2022: Impacts, adaptation and vulnerability. https://www.ipcc.ch/report/ar6/wg2/

Jonkman, B. J. (2009). Turbsim user's guide: Version 1.50.

Karimi, M., Hall, M., Buckham, B., & Crawford, C. (2017). The three classes of offshore floating wind turbine support platforms ... https://www.researchgate.net/publication/311784732_A_multi-objective_design_optimization_approach_for_floating_offshore_wind_turbine_support_structures

Li, L., Gao, Z., & Moan, T. (2013). Joint environmental data at five european offshore sites for design of combined wind and wave energy devices. *Journal of Offshore Mechanics and Arctic Engineering, 137*. https://doi.org/10.1115/OMAE2013-10156

Ørsted. (2018). Making green energy affordable how the offshore wind energy industry matured – and what we can learn from it. https://orsted.com/en/insights/white-papers/making-green-energy-affordable/1991-to-2001-the-first-offshore-wind-farms

R. Nejad, A., Bachynski-Polić, E., Li, L., & Moan, T. (2016). Correlation between acceleration and drivetrain load effects for monopile offshore wind turbines. *Energy Procedia, 94*, 487–496. https://doi.org/10.1016/j.egypro.2016.09.219

Robertson, A., Jonkman, J., Masciola, M., Song, H., Goupee, A., Coulling, A., & Luan, C. (2014). Definition of the semisubmersible floating system for phase ii of oc4. https://doi.org/10.2172/1155123

Rypestøl, M. (2020). *Analysis of floating offshore wind turbine subjected to ship collisions* (Doctoral dissertation). NTNU.

SENER. (2022). Hivewind - semi-submersible floating steel platform for offshore wind turbines. https://www.energy.sener/project/hivewind-semisubmersible-floating-steel-platform-offshore-wind-turbines

Siddiqui, M. A. (2020). *Experimental and numerical hydrodynamic analysis of a damaged ship section in waves* (Doctoral dissertation). NTNU.

Souza, C. E. A. d., Berthelsen, P. A., Eliassen, L., Bachynski, E. E., Engebretsen, E., & Haslum, H. (2021). *Definition of the INO WINDMOOR 12 MW base case floating wind turbine*.

Statista. (2023). World electricity generation shares by source 2022. https://www.statista.com/statistics/269811/world-electricity-production-by-energy-source/#:~:text=Global%5C%20electricity%5C%20mix%5C%202022%5C%2C%5C%20by%5C%20energy%5C%20source&text=Fossil%5C%20fuels%5C%20remain%5C%20the%5C%20greatest,with%5C%20a%5C%2022%5C%20percent%5C%20share.

UNFCCC. (2015). The paris agreement. https://unfccc.int/process-and-meetings/the-paris-agreement/the-paris-agreement

Vatnøy, A. (2022). The norwegian offshore wind industry: - we can once again be world leading. https://offshore-wind.no/news/the-norwegian-offshore-wind-industry-we-will-once-again-be-world-leading/

Vikkelsø, A., Sørensen, H. C., & Larsen, J. H. M. (2003). https://base.socioeco.org/docs/a118_doc1.pdf

WindEurope. (2020). Ports: A key enabler for the floating offshore wind sector.
WindEurope. (2021). Offshore wind energy 2021 mid-year statistics. https://windeurope.org/intelligence-platform/product/offshore-wind-energy-2021-mid-year-statistics/
WindEurope. (2022). Wind energy today. https://windeurope.org/about-wind/wind-energy-today/
Wu, Y., Kwan, T., Luo, Y., & Ma, K.-T. (2019). *Mooring system engineering for offshore structures*. Gulf Professional Publishing.